Magnetic, transport and magnetotransport properties of perovskites La_2BMnO_6 (B = Fe, Cu, and Cr)

Thesis Submitted to AcSIR For the Award of
the Degree of
Doctor of philosophy
In Physical Sciences

By

Jasnamol Pezhumkattil Palakkal

Registration Number: 10PP12A39016

Under the guidance of

Dr. Manoj Raama Varma

Materials Science and Technology Division (MSTD)
National Institute for Interdisciplinary Science and Technology (NIIST)-
Council of Scientific & Industrial Research (CSIR),
Govt. of India,
Thiruvananthapuram – 695019

August, 2017

राष्ट्रीय अंतर्विषयी विज्ञान तथा प्रौद्योगिकी संस्थान
NATIONAL INSTITUTE FOR INTERDISCIPLINARYSCIENCE AND TECHNOLOGY
वैज्ञानिक तथा औद्योगिक अनुसंधान परिषद् | Council of Scientific and Industrial Research
इंडस्ट्रियल इस्टेट पी.ओ, पाप्पनंकोड, तिरुवनंतपुरम, भारत - 695 019 | Industrial Estate P.O., Pappanamcode, Thiruvananthapuram, India - 695 019

Certificate

This is to certify that the work incorporated in this Ph.D. thesis entitled ***'Magnetic, transport and magnetotransport properties of perovskites La_2BMnO_6 (B = Fe, Cu, and Cr)'*** submitted by **Ms. Jasnamol Pezhumkattil Palakkal** to Academy of Scientific and Innovative Research (AcSIR) in fulfillment of the requirements for the award of the degree of doctor of philosophy embodies original research work under my supervision. I further certify that this work has not been submitted to any other University or Institution in part or full for the award of any degree or diploma. Research material obtained from other sources has been duly acknowledged in the thesis. Any text, illustration, table etc., used in the thesis from other sources, have been duly cited and acknowledged.

Ms. Jasnamol Pezhumkattil Palakkal — Dr. Manoj Raama Varma

(Research scholar) — (Research supervisor)

to my parents

One never notices what has been done;
One can only see what remains to be done.

- Marie Curie

Acknowledgement

On the time of my PhD thesis submission, I would like to thank the entire physical world for supporting me. The smiles of gratitude are being articulated to the whole forces of nature for being a part of my venture. I shall remember, some of the humans who nourished my research activities by physically or mentally, as the guidance received from thesis supervisor, help from friends and colleagues, and support from family.

I would like to state my deepest gratitude to my thesis supervisor Dr. Manoj Raama Varma, who has given me the opportunity to start my research career at his laboratory, magnetism group, NIIST and his support and motivation throughout the thesis work. Happiness is to thank him for encouraging me to work independently to achieve the research goal. He has given me enough opportunity to collaborate and work with various research groups of labs in India and Slovenia. I enjoyed the freedom he has been allowing in our lab. Apart from scientific discussions, we used to talk about humanity, religion, politics, etc. Further, I am very much happy to acknowledge the affection and care received from his wife, Ms. Jaya M Varma, who is a passionate dancer.

I am indebted to Dr. A. Ajaygosh (Director, NIIST) and Dr. Suresh Das (Former Director, NIIST) for providing the facilities for the research works. I am thankful to Dr. Luxmi Varma and Dr. Mamgalam Nair (present and former co-coordinators, AcSIR), Dr. S. Savithri, Dr. K. P. Surendran, and Dr. M. Vasundhara (DAC members) for their constant bits of advice and motivation during the course of PhD. The encouraging comments and love from Dr. Mamgalam Nair and Dr. S. Savithri are particularly accredited. The lectures taken by various scientists in NIIST as part of AcSIR coursework were significant to improve my knowledge.

I express my sincere thanks to Prof. Dr. Matjaz Valant (University of Nova Gorica, Slovenia) for his help and support during the experiments performed at University of Nova Gorica. He welcomed me so nicely to his lab at the University of Nova Gorica and gave me enough support during my entire tenure at Slovenia. I am thankful to Prof. Dr. K. G. Suresh (Indian Institute of Technology, Bombay) and Prof. Dr. P. N. Santhosh (Indian Institute of Technology, Madras) for their timely action on acquiring a few experimental data. I am grateful to Prof. Dr. P. S. Anil Kumar (Indian Institute of Science, Bangalore) for allowing me to work, and get experienced with pulsed laser deposition techniques at his lab at IISc.

The supports provided by the scientists of NIIST, especially Dr. Prabhakar Rao (Head, MSTD, NIIST), Dr. M. L. P. Reddy and Dr. M. T. Sebastian (Former Heads, MSTD, NIIST), Dr. H. K. Bhatt (Head, Metals and Minerals section, NIIST), Dr. U. Syamaprasad (Rtd. Scientist), and Dr. Jose James (Late Scientist), are thankfully acknowledged.

I am delighted to thank Dr. Raj Sankar C (Scientist Fellow) for his support during the finishing stages of this course. The scientific discussions with him were advantageous and motivational that helped me to improve the quality of this work. Also, his advice and comments greatly helped me to modulate the way of scientific presentations.

The former postdoctoral fellows of our group Dr. Senoy Thomas (Assistant professor, CUSAT, Cochin), and Dr. Savitha Pillai (Assistant professor, IIRBS, Kottayam) are acknowledged for their support. I would like to thank my senior colleagues Dr. Reshmi C P (Assistant professor, Govt. Victoria College, Palakkad), Dr. P. Neenu Lekshmi (Postdoctoral fellow, IIT Madras) and Ms. Raji G R for their love, support, and valuable advice. Dr. Neenu Lekshmi was like an elder sister to me whom I found worth sharing all my worries; both professional and personal.

The technical assistance received from Mr. P. Gurusamy, Mr. M. R. Chandran, Mr. A Peer Mohamed, Mr. Prithwiraj, Mr. Kiran, Mr. Robert Philip, Ms. Lucy Paul, Ms. Saumya V, and Dr.

George T M were useful for the research work. I am thankful to all the office and library staff at NIIST for all their cooperation.

I take this opportunity to thank Ms. Mojca V, and Prof. Dr. Artem B (University of Nova Gorica) for the help rendered during the magnetodielectric measurement at the University of Nova Gorica, Slovenia. I am thankful to Prof. Lambert Alff (Technische Universität Darmstadt, Germany) for the scientific discussions during the initial years of this course, which benefited me a lot.

The friendship and moral support received from my junior colleagues Mr. Ajeesh Paulose, Ms. Aswathi K, Ms. Aswathy VS, Ms. Sudakshina B, and Ms. Athira M during the PhD period were fabulous. The wild 'trekking' and other trips we made together were very funny and enjoyable. The companionship with Mr. Ajeesh was so spectacular, and I will remember all our crazy hunts for yummy foods and movies. I also would like to acknowledge my lab mates Ms. Bhagya U, Ms Revathy R, Mr. Rojerce Brown Job , Mr. Rahul S, Mr. T. Thanveer, Mr. M S Unnikrishnan, Mr. K. Rajeshkumar, Mr. V. R. Akshay, Ms. Ann Rose Sunny, Mr. B. Arun, Mr. S. Suneesh, Ms. Neethu, Mr. Vishnu, Dr. Neson Varghese, Dr. Aswathy, Dr. Anooja, Mr. Mahesh and Mr. Dinesh for their help and support.

Further, I thank all my friends at NIIST especially Ms. Aswathy R. S., Ms. R. Aiswarya, Mr. K. S. Dijith, Mr. S Vaisakh, Ms. Merin, Ms. Roshin Peter, and Ms, Asha Susan C for their love and support. I acknowledge the entire NIIST community for their help and cooperation.

I am greatly thankful to my friends at the University of Nova Gorica Ms. Jinta M, Mr. Uroš L, Mr. Egon P, Ms. Fei, Mr. Mattia, Mr. Saim, Mr. Andraž and Ms. Saša for their companionship during my days at the University of Nova Gorica, Slovenia. My heartfelt thanks are duly extended to my friends in IISc Bangalore, especially Ms. Kunjalatha and Mr. Vineeth Mohan for their support during my stay at IISc Bangalore.

University Grants Commission (UGC), Government of India is acknowledged for the Junior/Senior Research Fellowship. Department of Science and Technology (DST), India is being acknowledged for providing finance for the two international visits under the India-Slovenia bilateral research project.

I am also thankful to all my teachers and friends for their encouragement at different stages of my academic career.

It is a great moment to remember my family for their unrelenting efforts for making me as I am. Without the hope and support of my father, Mr. Abdurahiman, I would not be even able to join for the course of PhD. Apart from the societal and communal inhibitions, my dad insisted upon the education of his only girl child. The quiet smile of my mom, Ms. Asya, made me strong and my dad was always there as a backbone to my dream.

I am also thankful to my brother Mr. Jaisal, his wife Ms. Banu, and my little nephews Akif, Aza, and Amin for being there for me whenever I need a shoulder to lean.

And finally, to those, whom I missed to write a thanking note, knowingly or unknowingly, I shall keep all that gratitude inside my heart. When you come on by asking me an acknowledgement, I am wholeheartedly indebted to do so!

JASNAMOL P PALAKKAL

Contents

Abstract i-v

Chapter 1: Introduction 1.1-1.37

1.1 Structure of Perovskites and Double Perovskites..... 1.2

1.1.1 Jahn-Teller distortion..... 1.5

1.2 Features of double perovskites..... 1.7

1.2.1 Magnetic properties..... 1.8

1.2.1.1 Exchange interactions..... 1.9

1.2.1.1.1 Super exchange interaction..... 1.9

1.2.1.1.2 Double exchange interaction..... 1.12

1.2.1.2 Types of magnetic materials..... 1.13

1.2.1.2.1 Diamagnetism..... 1.14

1.2.1.2.2 Paramagnetism..... 1.15

1.2.1.2.3 Ferromagnetism..... 1.16

1.2.1.2.4 Ferrimagnetism..... 1.17

1.2.1.2.5 Antiferromagnetism..... 1.17

1.2.1.2.6 Griffiths-like phase..... 1.18

1.2.1.2.7 Spin glass materials..... 1.19

1.2.2 Electrical properties..... 1.20

1.2.3 Specific heat……..... 1.24

1.2.4 Dielectric properties..... 1.24

1.2.5 Magnetoresistance and Magnetodielectric coupling..... 1.25

1.3 Objectives and motivation of the work..... 1.27

1.3.1 Motivation behind the present investigation..... 1.27

1.3.2 Objectives of the present investigation..... 1.31

1.4 References..... 1.31

Chapter 2: Experimental Techniques **2.1-2.26**

2.1 Synthesis of La_2BMnO_6..... 2.2

2.2 Characterization Techniques..... 2.5

2.2.1 Powder X–ray diffraction……..... 2.5

2.2.2 Rietveld refinement of the powder XRD pattern……..... 2.8

2.2.3 Scanning Electron Microscopy..... 2.11

2.2.4 X-Ray Photoelectron Spectroscopy..... 2.13

2.2.5 Vibrating sample magnetometer..... 2.16

2.2.6 AC magnetic characterization..... 2.18

2.2.7 Electron spin resonance (ESR) or electron paramagnetic resonance (EPR)..... 2.20

2.2.8. Electrical resistivity and magnetoresistance…….. 2.21

2.2.9. Specific heat capacity measurements……. 2.23

2.2.10. Dielectric and Magnetodielectric measurement……... 2.24

2.3 References……. 2.25

Chapter 3: High-temperature magnetic transition and existence of positive and negative magnetodielectric coupling in La_2FeMnO_6 **3.1-3.47**

Section 3-1: High-temperature magnetic transition and existence of ferromagnetic short-range correlations above transition in La_2FeMnO_6 **3.2**

3-1.1 Introduction……. 3.3

3-1.2 Experimental Details…….. 3.4

3-1.3 Results and discussion…… 3.5

3-1.3.1 Structural characterization……... 3.5

3-1.3.2 Magnetic characterization……... 3.6

3-1.3.3 Specific heat and electron spin resonance spectra…….. 3.14

3-1.4 Conclusions…… 3.15

Section 3-2: Large positive and negative magnetodielectric coupling in La_2FeMnO_6 **3.17**

3-2.1 Introduction…… 3.18

3-2.2 Experimental…….. 3.20

3-2.3 Results and discussion…… 3.21

3-2.3.1 Structural characterization……... 3.21

3-2.3.2 DC transport properties and charge ordering…….. 3.26

3-2.3.3 AC magnetic susceptibility……. 3.30

3-2.3.4 ZFC memory and aging test…… 3.32

3-2.3.6 Dielectric properties…… 3.34

3-2.3.6 Magnetodielectric coupling……. 3.37

3-2.4 Conclusion…….. 3.39

3-2.5 References…….. 3.40

Chapter 4: Unusual magnetodielectric effects in frustrated ferromagnetic perovskite La_2CuMnO_6 **4.1-4.25**

4.1 Introduction……... 4.2

4.2 Experimental..... 4.4

4.3 Results and discussion……... 4.5

4.3.1 Structural properties……... 4.5

4.3.2 DC and AC Magnetic Properties…… 4.7

4.3.3 Specific heat and dc resistivity..... 4.11

4.3.4 Dielectric properties..... 4.12

4.3.5 Magnetodielectric coupling..... 4.17

4.4. Conclusion..... 4.20

4.5. References..... 4.21

Chapter 5: Multiple magnetic transitions, Griffiths-like phase, and Magnetoresistance in La_2CrMnO_6 **5.1-5.26**

5.1 Introduction..... 5.2

5.2 Experimental..... 5.4

5.3 Results and discussion..... 5.5

5.3.1 Structural properties..... 5.5

5.3.2 DC and AC Magnetic Properties..... 5.7

5.3.3 Specific Heat, dc resistivity, and magnetoresistance..... 5.19

5.4. Conclusion..... 5.22

4.5. References..... 5.23

Chapter 6: Conclusion and scope of future works **6.1-6.7**

6.1 Conclusion……. 6.2

6.1.1 High-temperature magnetic transition and existence of positive and negative magnetodielectric coupling in La_2FeMnO_6…… 6.2

6.1.2 Unusual magnetodielectric effects in frustrated ferromagnetic perovskite La_2CuMnO_6…… 6.3

6.1.3 Multiple magnetic transitions, Griffiths-like phase, and Magnetoresistance in La_2CrMnO_6……... 6.5

6.2 Scope of future works…… 6.7

Appendix A: Magnetism and transport properties of ordered double perovskite Ba_2FeWO_6..... A.1-A2

Appendix B: Magnetism and magnetoresistance in $La_2B'NiO_6$ (B'=Co, & Al)..... B.1-B.3

List of publications and conferences……... P.1-P.3

List of Figures

Figure 1.1 The structure of perovskite ABO_3, with B-site cation (blue ball), O anion (red ball), and A-site cation (green ball)…… 1.3

Figure 1.2. The structure of double perovskite $A_2BB'O_6$, with alternative B-sites occupied by B and B' cations…… 1.5

Figure 1.3 Electronically degenerate state of d^1 configuration……. 1.6

Figure 1.4. (a) p-orbitals (b) Octahedral splitting of d-orbitals……. 1.10

Figure 1.5. Superexchange and GKA rules illustrated for the (a) AFM and (b, c) FM exchange interactions……. 1.12

Figure 1.6. The double exchange between the $3d_{z^2}$ orbital of Mn^{3+} and Mn^{4+} ion via the $2p_z$ orbital of an O^{2-} ion…….. 1.13

Figure 1.7 (a) Magnetic moment with field and (b) Susceptibility with temperature for a diamagnetic material……. 1.14

Figure 1.8 (a) Magnetic moment with field and (b) Susceptibility with temperature for a paramagnetic material……... 1.15

Figure 1.9 (a) Magnetic hysteresis loop and (b) Susceptibility with the temperature for a ferromagnetic material…….. 1.16

Figure 1.10 Susceptibility with temperature of an AFM material……. 1.17

Figure 1.11 Inverse susceptibility vs. temperature for antiferromagnetic (AFM), paramagnetic (PM), ferromagnetic (FM), and Griffiths-like phase (GP) 1.18

Figure 1.12. Electron transport between localized states in various cases (1) thermally assisted tunneling (2) tunneling and (3) tunneling with the emission of the photon……... 1.22

Figure 1.13 Variable range hopping and nearest neighbor hopping……. 1.23

Figure 2.1 Various steps involved in the synthesis of La_2BMnO_6…… 2.4

Figure 2.2 (a) Diffraction of incident X-Rays by parallel planes. (b) Schematic representation of powder X–ray Diffractometer……... 2.6

Figure 2.3 Schematic representation of a SEM microscope…….. 2.13

Figure 2.4. The photoemission process involved for XPS surface analysis…….. 2.14

Figure 2.5. Schematic diagram of main instrumental components in XPS…….... 2.15

Figure 2.6. Schematic representation of VSM…….. 2.18

Figure 2.7. Splitting of electron spin states on an application of magnetic field.. 2.20

Figure 2.8 (a) Four-probe method of measuring resistivity. (b) Electrical field lines and equipotential lines in a material during the four-probe method……. 2.22

Figure 2.9. Thermal connections to sample and sample platforms in PPMS heat capacity option……... 2.23

Figure 2.10. Parallel plate capacitor method……. 2.24

Figure 3-1.1 (a) Observed, calculated and the difference XRD pattern of La_2FeMnO_6 obtained from Rietveld refinement. (b) A small portion of the crystallographic structure of La_2FeMnO_6 crystal framed using CrystalMaker®. XPS spectra of (c) Fe $2p_{3/2}$ and (d) Mn $2p_{3/2}$ in La_2FeMnO_6 along with the fitted curves……... 3.6

Figure 3-1.2 ZFC and FC curves at 50, 200, and 1000 Oe for 5-380 K. Inset showing ZFC and FC curves at 50, 200, and 1000 Oe for 300-950 K…….. 3.7

Figure 3-1.3 Derivative of magnetization (FC) with respect to temperature vs. temperature for (a) 5-300 K and (b) 300-950 K. (c) M-H curves recorded at different temperatures. (d) Variation of coercivity (H_C) and remanence (M_r) with temperature…… 3.9

Figure 3-1.4 (a) Temperature dependence of inverse susceptibility (FC) at various fields. (b) CW fit (solid red line) on $1/\chi$ (T) (FC) at 20 Oe. (c) ln (χ^{-1}) vs. ln ($T-T_C^R$) at 20, 50 and 200 Oe. The solid green line is the linear fit. (d) The Arrot plot (M^2 vs. H/M) at different temperatures below and above T_C. The solid red line is the linear fit…….. 3.10

Figure 3-1.5 (a) Specific heat (C) as a function of temperature. (b) Low-temperature specific heat C fit. (c) ESR spectra of La_2FeMnO_6 at different temperatures. (d) Enlarged low field region of ESR spectra showing FMR signals…… 3.14

Figure 3-2.1 Observed and calculated powder XRD patterns of La_2FeMnO_6 along with the difference curve and Bragg positions at (a) 100 K and (b) 300 K. 3.22

Figure 3-2.2 (c) SEM image showing the surface of the sintered pellet..... 3.23

Figure 3-2.3 XPS spectra of La_2FeMnO_6 along with the fitted curves for (a) Fe $2p_{3/2}$ showing Fe^{2+} and Fe^{3+} and for (b) Mn $2p_{3/2}$ showing Mn^{4+} and Mn^{3+}..... 3.24

Figure 3-2.4 The arrangements of Mn/Fe-O-Fe/Mn bonds (Blue/Green-Fe/Mn and Red-O) marked with bond angle (b-axis view) for (a) 100 K (b) 300 K..... 3.25

Figure 3-2.5 (a) Variation of resistivity (ρ) with temperature. The inset shows ln (ρ) vs. $1/T^{1/4}$ plot with a linear fit (red) for the VRH model. (b) ln (ρ/T) vs. 1/T plot with a linear fit (red) for the SPH model..... 3.26

Figure 3-2.6 (a) Differential scanning calorimetry (left y-axis and bottom x-axis), showing a peak and C/T vs. T (right y-axis and upper x-axis) showing a kink near the T_{CL}. (b) Variation of DC susceptibility with temperature for field cooled measurement at 10 kOe..... 3.28

Figure 3-2.7 Magnetic moment vs. magnetic field at 42 K, 102 K, 134 K, and 174 K depicting the formation of wasp-waisted hysteresis loop near and above T_{CL}..... 3.29

Figure 3-2.8 Variation of (a) imaginary part of AC susceptibility with temperature at various frequencies. (b) ln τ vs. $1/T_m$ plot along with the Arrhenius fit (solid red line). Variations of the imaginary part of AC susceptibility with temperature with and without a DC field at (c) 227 Hz and (d) 397 Hz..... 3.31

Figure 3-2.9 The variation of ΔM as a function of temperature…… 3.32

Figure 3-2.10 (b) Time evolution of ZFC magnetic moment measured at H_{meas}=50 Oe, T_{meas}=50 K, and t_w=1000 s, and 5000 s. Solid red lines are the best fit to the stretched exponential function…… 3.33

Figure 3-2.11 Variation of (a) ε (Closed symbols at 0 Oe and open symbols at 5 kOe), (b) tan δ (Closed symbols at 0 Oe and open symbols at 5 kOe), (c) ε' and (d) ε'' with the temperature at various frequencies..... 3.34

Figure 3-2.12 Arrhenius fits (solid red line) for the relaxations in (a) tan δ, (b) low-temperature relaxation in ε', and (c) high-temperature relaxation in ε'..... 3.36

Figure 3-2.13 Variation of MD and MDL (inset) with the temperature at various frequencies..... 3.38

Figure 4.1 (a) XRD pattern of La_2CuMnO_6 after Rietveld refinement. (b) Distorted octahedron of La_2CuMnO_6. (c) SEM image, showing the ceramic microstructure…… 4.5

Figure 4.2 XPS spectra of (a) Cu $2p_{3/2}$ and (b) Mn $2p_{3/2}$ in La_2CuMnO_6 along with the fitted curves…… 4.6

Figure 4.3 (a) ZFC and FC thermomagnetic curves at various fields. Inset is showing the dM/dT vs. T plot. (b) ZFC curves for low-temperature region showing AFM interactions…… 4.7

Figure 4.4 (a) Temperature dependence of AC susceptibility (χ_{ac}) and inset showing real part of AC susceptibility (χ_{ac}'') at various frequencies. (b) Isothermal magnetization curves recorded at different temperatures. Inset depicting the variation of coercivity (H_C) and remanence (M_r) with temperature 4.8

Figure 4.5 (a) Temperature dependence of inverse dc susceptibility (FC) at various fields. Inset of (a) showing the CW fit (solid blue line) on $1/\chi$ (T) for FC at 100 Oe. (b) ln (χ^{-1}) vs. ln ($T-T_C^R$) at 100 Oe with the linear fit (solid blue line). Inset of (b) showing the M^2 vs. H/M plot above T_C depicting the absence of a spontaneous magnetization……. 4.10

Figure 4.6 (a) Temperature dependence of specific heat (C/T) vs. T plot. The inset is showing the specific heat fit for the low-temperature region (5-80 K). (b) Temperature dependence of resistivity (ρ). Inset is showing the ln (ρ) vs. $1/T^{1/4}$ plot with the solid red line showing the linear fit for VRH model…….. 4.11

Figure 4.7 Temperature dependence of (a) dielectric constant (ε) and (b) loss tangent (tan δ) at various frequencies: 4 kHz, 8 kHz, 12 kHz, 15 kHz, 18 kHz, 20. 5 kHz, 40.9 kHz, 81.7 kHz, 122.5 kHz, 204.2 kHz, 285.8 kHz, 367.4 kHz, 449.0 kHz, 530.7 kHz, 612.3 kHz, 693.9 kHz, 775.5 kHz, 857.2 kHz, 938.8 kHz, and 1 MHz. Arrhenius fit to the relaxation time in tan δ for (c) 0 Oe and (d) 5 kOe…… 4.13

Figure 4.8 Variation of (a) real part (ε') and (b) imaginary part (ε'') of dielectric constant with temperature at various frequencies ranging from 4 kHz to 1 MHz. (c) log (ε'f) vs. log f and (d) variation of ε'' with frequency at selected temperatures…….. 4.16

Figure 4.9 Temperature variations of (a) magnetodielectric coupling and (b) magnetodielectric loss coupling at various frequencies (c) The maximum in tan δ (T_m) corresponding to each frequency with 0 Oe and 5 kOe. Inset is showing the maximum MD coupling observed for each frequency. (d) Variation of magnetodielectric coupling and magnetodielectric loss coupling with the temperature at 4 kHz and 285.8 kHz; depicting negative MDL corresponding to positive MD and positive MDL corresponding to a low value of MD……. 4.19

Figure 5.1. (a) Observed, calculated, and the difference XRD pattern of La_2CrMnO_6 obtained from Rietveld refinement. The blue bars indicate the Bragg positions. (b) A portion of the La_2CrMnO_6 crystal structure along with the reference axes…….. 5.6

Figure 5.2. XPS spectra of (a) Cr $2p_{3/2}$ and (b) Mn $2p_{3/2}$ in La_2CrMnO_6 along with the fitted curves……. 5.6

Figure 5.3 (a) ZFC and FC thermomagnetic curves at various fields. Inset is showing the dM/dT vs. T plot. (b) M/H vs. T of the ZFC curves at different fields indicating the dip at 60 K. Inset of (b) showing the isothermal magnetization curves recorded at different temperatures. (c) The zoomed center portion of MH loop at various temperatures. (d) Temperature dependence of inverse dc susceptibility (FC) at 100 Oe along with the CW fit (solid blue line). Inset of (d) depicting the variation of coercivity (H_C) and remanence (M_r) with temperature…… 5.11

Figure 5.4 (a) Temperature dependence of real part of AC susceptibility (χ_{ac}') and inset showing the temperature dependence of imaginary part of AC susceptibility (χ_{ac}'') at various frequencies for 2-300 K. (b) The $d\chi_{ac}'/dT$ vs. T plot showing the minima at 32 K, 56 K, and 123 K. Temperature dependence of (c) real (χ_{ac}') and (d) imaginary (χ_{ac}'') part of AC susceptibility for 2-130 K at various frequencies…… 5.12

Figure 5.5. Temperature dependence of real (χ_{ac}') part of ac susceptibility at H_{dc}=0 and 100 Oe for (a) f=4444 Hz, (b) f=9788 Hz. Temperature dependence of imaginary (χ_{ac}'') part of ac susceptibility at H_{dc}=0 and 100 Oe for (c) f=4444 Hz, (d) f=9788 Hz…….. 5.13

Figure 5.6 ln τ vs. T_m plot along with the fit to the critical power law for (a) transition near 5 K and (b) transition near 110 K…….. 5.15

Figure 5.7 (a) The variation of ΔM as a function of temperature. (b) Time evolution of ZFC magnetic moment measured at H=20 Oe, T_{meas}=2 K, and t_w=100 s, 1000 s, and 5000 s. Solid red lines are the best fit to the stretched exponential function…….. 5.16

Figure 5.8 (a) ln (χ^{-1}) vs. ln ($T-T_C^R$) at 100 Oe with the linear fit (solid blue line). Inset of (a) showing the CW fit (solid blue line) on 1/χ (T) for FC at 100 Oe. (b) M^2 vs. H/M plot above and below T_C…….. 5.17

Figure 5.9 (a) Temperature dependence of specific heat (C/T) vs. T plot. The inset is showing the specific heat fit for the low-temperature region (2-78 K). (b) Temperature dependence of resistivity (ρ). Inset is showing the ln (ρ/T) vs. $1/T^{1/4}$ plot with the red solid curve showing the nonlinear fit for SP-VRH model……. 5.20

Figure 5.10 Magnetoresistance as a function of (a) temperature at 90 kOe (b) magnetic field at 101 K, 102 K, and 120 K……... 5.21

Figure A.1 (a) Observed, calculated and the difference XRD pattern of Ba_2FeWO_6 obtained from Rietveld refinement. The bar marks represent the possible Bragg reflections. Inset: The crystallographic structure framed using CrystalMaker® (b) The ZFC and FC M(T) at 100 Oe. Inset showing the isothermal magnetization at 2 K (c) tan δ vs T at various frequencies (d) Percentage MD vs. T at different frequencies. Inset showing percentage MDL vs. T at different frequencies……. A.1

Figure B.1 (a) Observed, calculated and the difference XRD pattern of La_2CoNiO_6 obtained from Rietveld refinement. The bar marks represent the possible Bragg reflections. Inset showing the crystallographic structure framed using CrystalMaker® (b) The ZFC and FC M(T) at various magnetic fields. Inset showing dM/dT vs. T plot (c) inverse susceptibility vs. T along with the C-W linear fit (d) Magnetoresistance as a function of magnetic field at various temperatures…….. B.1

Figure B.2 (a) Observed, calculated and the difference XRD pattern of La_2AlNiO_6 obtained from Rietveld refinement. The bar marks represent the possible Bragg reflections. Inset showing the crystallographic structure framed using CrystalMaker® (b) FC DC susceptibility vs. temperature plot along with the modified CW fit at 100 Oe. Inset showing the ZFC and FC DC susceptibility vs. temperature at 20 Oe and 100 Oe (c) Magnetic hysteresis loop at 2 K. Inset is showing the zoomed center portion (d) Magnetoresistance as a function of magnetic field at various temperatures…….... B.2

List of Tables

Table 1.1 Some prominent reports on % MD shown by La_2NiMnO_6 and La_2CoMnO_6…….. 1.28

Table 3-1.1 Calculated μ_{eff} in units of μ_B/f.u. for La_2FeMnO_6 with Fe^{3+} and Mn^{3+}…… 3.12

Table 3-2.1 Lattice parameters, bond lengths, bond angle, J-T and angle distortion along with reliability factors for the structural refinement of La_2FeMnO_6 at 100 K and 300 K……. 3.22

Table 3-2.2 The fitted parameters obtained from the resistivity data…….. 3.27

Table 3-2.3 The characteristic relaxation times and activation energies calculated for different relaxations obtained from the Arrhenius fit……... 3.36

Table 5.1. The effective moment (in units of μ_B / f.u.) calculated for different combinations of Cr and Mn cations..... 5.9

Table 5.2. The parameters obtained after the mathematical fitting of the time dependent ZFC magnetization by using the stretched exponential function..... 5.16

Table 6.1. Important results obtained for La_2BMnO_6 (B=Fe, Cu, and Cr)..... 6.6

Abstract

The basic materials research can provide scientific knowledge for the design/synthesis of potential materials for different technological applications. The extensive research made so far on the transition metal oxides with perovskite structure (ABO_3; A=Alkaline earth/Rare earth metals, B=Transition metals) have brought a variety of physical properties such as magnetoresistance, magnetodielectric, half metallic/metallic/insulating/semi-conducting properties etc. that are attractive for both scientific and technological aspects. The double perovskites ($A_2BB'O_6$) show a variety of physical properties by way of differences in B/B' ordering, oxidation states of cations, B-O-B' exchange interaction, etc. An external magnetic field can interact with materials to induce a variation in the physical properties. Hence the study of magnetic, transport and magnetotransport properties of perovskites La_2BMnO_6 (B=Fe, Cu, and Cr) becomes extremely important in the present scientific scenario. The present thesis aims at synthesizing these materials and investigating the magnetic and physical properties systematically. The thesis has six chapters including introduction, experimental techniques and results and the conclusion and the scope of future work. Also, two appendices are attached to introduce additional results on some more double perovskites.

Chapter 1 ***Introduction:*** This chapter gives a brief literature survey on the introduction to Perovskites and Double perovskite, interactions in double

perovskites, features of double perovskites, Mn-based double perovskites and the objectives and scope of the work.

Chapter 2 ***Experimental Techniques:*** This chapter gives details of synthesis methods and experimental techniques used for characterization.

Chapter 3 ***High-temperature magnetic transition and existence of positive and negative magnetodielectric coupling in La_2FeMnO_6:*** This chapter has following sections.

Section 3-1 High-temperature magnetic transition and existence of ferromagnetic short-range correlations above transition temperature in La_2FeMnO_6: This section presents the observation of a high-temperature magnetic transition along with the ferromagnetic short-range correlations (FSCs) in La_2FeMnO_6 perovskite system. A large positive and negative magnetodielctric (MD) coupling is also observed in the material. The M-T curves show two distinct transitions at T_{C1}~60 K and T_C~425 K. Coercivity values of ~1140 Oe, and ~35 Oe are observed at 2 K and 300 K respectively. The thermomagnetic analysis reveals the presence of FSCs in La_2FeMnO_6 up to T*= 570 K, well above the transition temperature, similar to Griffiths-like phase (GP). The electron spin resonance spectra show ferromagnetic resonance signals showing the possibility of the presence of FSCs at room temperature. The large contribution from electronic specific heat is an indication of ferromagnetic charge localized state.

Section 3-2 Large positive and negative magnetodielectric coupling in La_2FeMnO_6: The conduction mechanism in La_2FeMnO_6 established a localization of charge carriers in a distorted low temperature phase; resembling a charge

localization at T_{CL}~133 K with corresponding changes in the heat flow and specific heat. The wasp-waisted hysteresis loop above T_{CL} demonstrated a complex exchange interaction between the $Fe^{2+}/Fe^{3+}/Mn^{4+}/Mn^{3+}$ cations. The ZFC memory and aging, ac susceptibility and the dielectric permittivity as a function of temperature at different frequencies indicated the occurrence of a spin glass property and dielectric relaxation. The magnetodielectric (MD) coupling make La_2FeMnO_6 a candidate for the new class of materials that exhibit both the positive and negative MD effects. The observed large MD values of +45% at 122 K, -18% at 147 K and -6.8% near room temperature in a small applied field of 5 kOe make the material superior than reprted values in the literature.

Chapter 4 ***Unusual magnetodielectric effects in frustrated ferromagnetic perovskite La_2CuMnO_6:*** A series of fixed frequency dielectric measurements disclose a dielectric relaxation in the ferromagnetic perovskite La_2CuMnO_6, with a dynamic (Arrhenius to Arrhenius) crossover at T_C. The external magnetic field alters the relaxation parameters in the vicinity of crossover and induces an unusual trend in the magnetodielectric (MD) coupling around the T_C. Large MD coupling of 55 % at 68 K for 4 kHz and 61 % at 105 K for 285.8 kHz in a small applied magnetic field of 5 kOe is discovered. Zero-field cooled magnetic measurements evidenced a combined antiferromagnetic and ferro/ferrimagnetic phase below T_C. The thermomagnetic analysis reveals the presence of GP with FSCs above T_C. Specific heat analysis pointed the possibility of the presence of a ferromagnetic (FM) variable range hopping (VRH) active charge localized state. The bulk conduction mechanism for the charge carriers pursues a VRH model. The presence of FM short range correlations and the influence of a core grain dominated magnetoresistance on

the Maxwell-Wagner interfacial polarization are responsible for the observed large MD effect. Both the magnetic ordering and the external magnetic field control the electric dipole relaxation in the material.

Chapter 5 ***Multiple magnetic transitions, Griffiths-like phase and magnetoresistance in La_2CrMnO_6:*** Multiple magnetic transitions arising from the competing magnetic interaction between Cr and Mn are observed for the perovskite La_2CrMnO_6 from dc and ac magnetic measurements. A ferromagnetic and spin glass transitions are observed. The material also has a GP with the occurance of FSCs above T_C. The system ultimately turns into paramagnetic at the Griffiths temperature 180 K. A combination of variable range hopping and nearest neigbor small polaron hopping governs the conduction mechanism in the material. A negative magnetoresistance of 22% at 105 K is observed for the material at 90 kOe which increases to 29% at temperature near 110 K and reduced gradually to zero on further increase in the temperature .

Chapter 6 ***Conclusion and scope of future works:*** This chapter concludes the thesis and gives a summary of the studeis described in the earlier chapters. Also the chapter points the scope of the future works. Some preliminary studies for future works are done that are listed in appendices A and B.

Appendix A ***Magnetism and transport properties of ordered double perovskite Ba_2FeWO_6:*** Magnetic, dc resistivity, magnetoresistance, dielctric relaxation and magnetodielctric coupling in ordered double perovskite Ba_2FeWO_6.

Appendix B ***Magnetism and magnetoresistance in $La_2B'NiO_6$ (B'=Co, & Al):*** The perovskite materials La_2CoNiO_6 and La_2AlNiO_6 are compared based on the

observed magnetic and magnetoresistance properties. The superexchange interaction between the transition element cations present in La_2CoNiO_6 offer ferromagnetism in the material. La_2AlNiO_6 exhibits a temperature dependent (thermally excited) paramagnetic susceptibility that follows the modified Curie-Weiss law. Both the materials are exhibiting magnetoresistance.

Chapter 1

Introduction

This chapter gives a brief introduction to perovskites and double perovskites, structure and physical properties of double perovskites. The objectives and motivation of the present investigation are also discussed.

1.1 Structure of Perovskites and Double Perovskites

The general formula for a perovskite is ABX_3 where A and B are cations, and X is an anion. The name perovskite came from Russian mineralogist Lev Perovski after his discovery of mineral $CaTiO_3$ with perovskite structure. The most studied and researched family of oxide systems includes perovskite oxides ABO_3, where A is usually an alkaline earth or rare earth element cation and B is a transition element cation. The importance of compounds belonging to this family of the crystal structure is due to their wide variety of properties and their flexibility to accommodate almost all the elements of the periodic system. The crystal structure of ideal cubic ABO_3 perovskite can be described as consisting of B cation in a 6-fold coordination with anions thus forming an octahedron. The A cation is then in the middle of a cube with a 12-fold cuboctahedral coordination with eight BO_6 octahedra at the corners of the cube. The ideal cubic perovskite structure is given in figure 1.1. The perovskite structure is known to be exceptionally adaptable. The A and B ions can be changed so that countless compounds can be formed with perovskite or related structures. The relative ion size requirements for the stability of the cubic structure are quite strict. So, a small fall and distortion can make a few lower-symmetry distorted structures, in which the coordination numbers of A cation, B cations or both are reduced.

Normally, the A cations are bigger than the B cation. A distorted perovskite structure originates when the central A cation is smaller than the corner B cation. This may cause a revise in the usual positions of O anions and B cations in ideal cubic structure, and the structure gets deviated. The reduced symmetry due to the

distorted perovskite structure has a noteworthy impact on their physical properties and practical applications.

The stability of a perovskite structure is determined based on a factor called Goldschmidt's tolerance factor t defined as $t=(R_A+R_O)/[\sqrt{2}(R_B+R_O)]$, where R_A, R_B, and R_O are the ionic radii of A, B cations and O anions respectively [1]. The tolerance factor is 1 for an ideal perovskite structure. A large number of ABO_3 type oxides are stable in perovskite structure with the tolerance factor slightly varying around 1 [2]. Reports are claiming a few crystal structures for the perovskite lattice corresponding to the particular range of t values. Yakel reported that $0.8 < t < 0.9$ stands for orthorhombic (monoclinic), $0.9 < t < 0.97$ stands for cubic, and $0.97 < t < 1.02$ stands for tetragonal perovskite structure [3]. Tokura *et al.* reported that $0.96 < t < 1$ is rhombohedral and $t < 0.97$ is an orthorhombic structure [4].

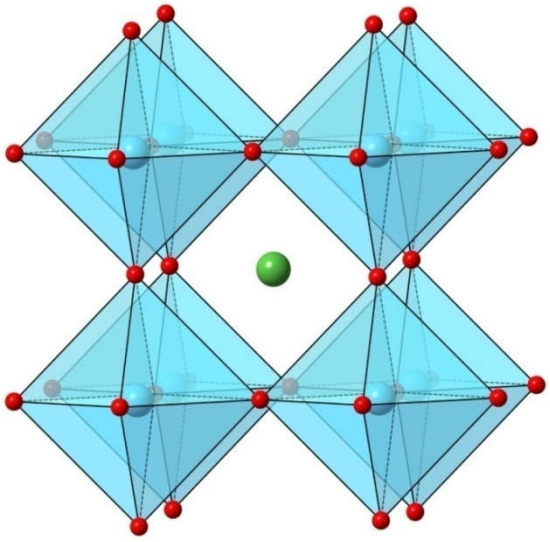

Figure 1.1 The structure of perovskite ABO_3, with B-site cation (blue ball), O anion (red ball), and A-site cation (green ball)

The double perovskite structure is formed by suitably modifying the simple perovskite structure by equally incorporating two types of B cations with different

size and charge, as depicted in figure 1.2. The general formula of the double perovskite is $A_2BB'O_6$ (or $AB_{0.5}B'_{0.5}O_3$). When viewed along the three axes, $A_2BB'O_6$ unit cell may be seen as doubled, regarding the primitive cell of ABO_3. The BO_6 and $B'O_6$ octahedra are arranged in two interleaving FCC sublattices. The B and B' atoms are ordered in a double perovskite because of charge, size and electronegativity difference. If the B and B' cations are of different charges, then the oxygen anions have a slight tendency to shift towards the more charged cation while the octahedral symmetry of B and B' cations is preserved. If the ionic radii of B and B' cations are comparable, then there is a possibility of occurring anti-site defects where adjacent B-sites are occupied by same B/B' cations. This means that if the size or valence difference between B and B' is reduced, then the ordering becomes more difficult, and the amount of structural defects increases. It is customary to write B-site disordered double perovskites as disordered $A_2BB'O_6$ or $AB_{0.5}B'_{0.5}O_3$. Also, the size mismatch of A and B/B' ions create a cooperative octahedral tilting to the structure to achieve an energetically stable arrangement. When the A cation is smaller than B/B' cation, the empty space around A cation causes an octahedral tilt. The complex deformation tilt is a sign of the rotation of neighboring octahedra.

The tolerance factor t for the double perovskites are modified as $t=(R_A+R_O)/[\sqrt{2}((R_B+R_{B'})/2)+R_O)]$, where the ionic radius of B is replaced by the average ionic radii of both the B and B' cations. In the majority of cases, the double perovskites with $0.96 < t < 1.06$ are cubic/tetragonal, $t < 0.96$ are orthorhombic/monoclinic and $1.06 < t$ are hexagonal [5].

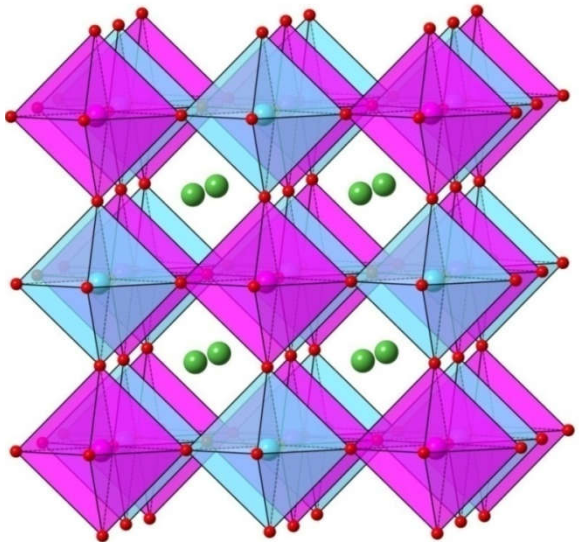

Figure 1.2. The structure of double perovskite $A_2BB'O_6$, with alternative B-sites occupied by B and B' cations.

The wide range of properties exhibited by double perovskites is mainly associated with B-site cations. For highly symmetric double perovskite systems, the oxygen anions are located in between the B and B' cations as a straight line. Tilting of the BO_6 and $B'O_6$ octahedra may arise as a result of lowering of symmetry. This builds a deviation in the B-O-B' bond angle from 180° and accordingly affects the path of electronic/magnetic interactions along the B-O-B'-O-B providing different functional properties. Thus the search for new functional materials having double perovskite structure and study of the interplay between their crystal structure, electronic structure, magnetism, electrical transport, spin-orbit interactions, electron-lattice coupling, etc. are of great interest to researchers in materials science.

1.1.1 Jahn-Teller distortion

Jahn-Teller (J-T) effect states that a nonlinear molecule with a spatially degenerate electronic ground state will undergo a geometrical distortion that

eliminates the degeneracy by lowering the overall energy of the system [6]. Perovskite oxides with transition metal cations at the octahedral site are likely to exhibit the J-T distortion.

According to the molecular orbital theory, in an octahedral complex, the five d atomic orbitals are split into two degenerate sets t_{2g} $\left(d_{xy}, d_{yz}, d_{xz}\right)$ and e_g $(d_{z^2}, d_{x^2-y^2})$. Degenerate states will avail more than one orbital for occupying an electron. For example, the one electron present in the d^1 configuration of octahedral symmetry will have three t_{2g} orbitals with same energy to occupy. In such case, the electron will asymmetrically occupy in any of the three degenerate orbitals $\left(d_{xy}, d_{yz}, d_{xz}\right)$as in figure 1.3. The asymmetric occupation leads to an increase in system energy. So, the system tries to get rid of this extra energy by lowering the system symmetry and undergoes the J-T distortion.

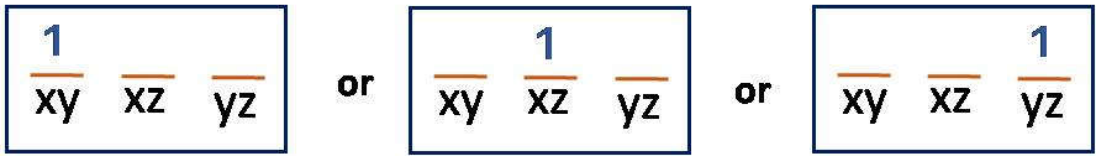

Figure 1.3 Electronically degenerate state of d^1 configuration.

The electronic degeneracy and J-T distortion are possible in all the d-orbital configurations in octahedral symmetry except d^3, d^8, d^{10}, high spin d^5 and low spin d^6 configurations. Since the e_g orbitals are directed towards the ligands, an asymmetrically occupied e_g orbital will gain considerably more energy. Thus, a significant J-T distortion is shown by high spin d^4, low spin d^7, and d^9 configurations in the octahedral environment.

The double perovskites containing transition element cations in the octahedral site are likely to undergo a J-T distortion. The J-T distortion can be calculated by using the equation [7] $\Delta d = \frac{1}{6}\sum_{1}^{6}\left[\left(d_n - \langle d\rangle\right)/\langle d\rangle\right]^2$ (where d_n is average for the n^{th} B/B'-O bond length and <d> is the average for all B/B'-O bond lengths).

1.2 Features of double perovskites

The perovskite oxides are showing a broad range of physical properties like ferromagnetism (FM), ferrimagnetism (FiM), antiferromagnetism (AFM), superconductivity, metallic and semiconducting property, half-metallicity, intergrain tunneling type magnetoresistance (MR), dielectric relaxation, magnetodielectric (MD) coupling, etc. [8-13]. The interesting electronic and magnetic properties of transition metal oxide perovskites are due to the presence of d-electrons and the metal–oxygen (B-O) bond. The double perovskites with alternative B-site occupied by two transition metal cations, are interesting due to the possibility of a variety of properties by virtue of B/B' ordering, B-O-B' bond angles, oxidation states of B/B' cations, antiphase boundaries, lattice distortion incorporated with perovskite structure, etc. [8-11]. Various combinations of different cations with different magnetic states at A, B, and B' sites are possible for the double perovskites and thereby exhibit surprising magnetic behaviors. The superexchange and double exchange interactions are the interactions known to be present in these materials. Since these interactions are between B and B' mediated by an intermediary O ion, the size and charge of B/B' cations, the B-O-B' bond angle, the B-site ordering, etc.

have great importance regarding the magnetic properties. These factors introduce a frustrated magnetic structure that may give rise to spin glass and clustered spin glass type behavior because of the lack of long-range magnetic order. Also, there is a real/virtual hopping of electrons occurring during the superexchange/double exchange interaction between the transition metal cations mediated by O anion. This introduces a variety of electrical conduction mechanisms and dielectric relaxation phenomenon in the double perovskite material. A possible coupling of magnetic and electric phases is also expected for these materials. The strong interplay between spin, charge, lattice, and orbital degrees of freedom in transition metal oxide perovskites offer unlimited opportunity to tune their physical properties. Physical properties of materials exploiting both the spin and charge degrees of freedom of charge carriers are interesting for both scientific and technological applications [7, 14-20].

1.2.1 Magnetic properties

Materials can be classified into two broad classes based upon the magnetism they exhibit. In the first class of materials, the individual magnetic moments present in the material are non-interacting each other and each moment acts independently of the others. Diamagnetic and paramagnetic (PM) materials belong to this class. The second class of magnetic materials forms magnetically ordered states as the magnetic moments couple to one another. This coupling is an exchange interaction and is based upon the overlap of electrons in conjunction with Pauli's exclusion principle. Perovskites have generally coupled magnetic moments at some temperature ranges. The perovskites $LaMnO_3$, $LaFeO_3$, $LaCrO_3$, $LaCoO_3$, $LaCuO_3$, etc. generally show an antiferromagnetic ordering at low temperatures [21-26],

while the double perovskites La_2NiMnO_6 and La_2CoMnO_6 are showing a ferromagnetic or ferrimagnetic ordering [27, 28]. The exchange interactions pertaining in the B-site cations have an important role in determining the magnetic properties of these compounds.

1.2.1.1 Exchange interactions

Exchange interaction is a quantum mechanical effect that arises between particles or ions. Same charges cost energy when they are close together and save energy when they are apart [29]. The individual magnetic moments associated with atoms/ions will be forced into parallel (ferromagnetic) or antiparallel (antiferromagnetic) alignment with their neighbors via exchange interaction between the neighboring magnetic atoms/ions. The exchange interactions are classified into direct exchange, indirect exchange and double exchange interactions. The indirect exchange interaction in ionic solid is the superexchange interaction, and that in metals is the RKKY interaction [29]. The exchange interactions pertaining in the transition metal oxide double perovskites are superexchange and double exchange interactions. They are explained as follows.

1.2.1.1.1 Superexchange Interaction

The magnetism in transition metal oxides is generally governed by the superexchange interaction with a virtual hopping of electrons. Superexchange interaction is the indirect exchange interaction in ionic solids since there is no direct overlap between orbitals of magnetic ions. It is mediated by a non-magnetic ion placed in between the magnetic ions. Superexchange is proposed by Hendrik Kramers in 1934 [30]. Later Phillip Anderson modified the Kramers' model, and

Goodenough and Kanamori proposed some semi-empirical rules for the superexchange [23, 31-33].

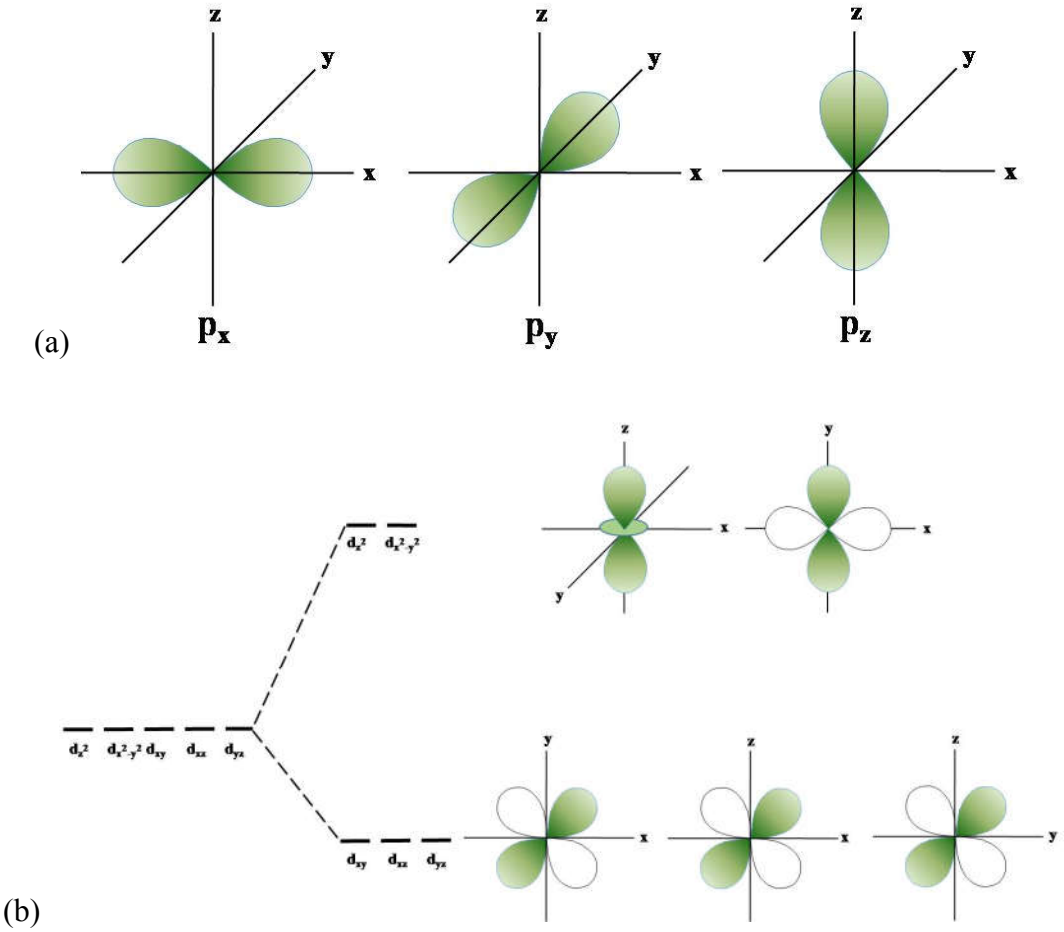

Figure 1.4. (a) p-orbitals (b) Octahedral splitting of d-orbitals

Consider two transition metal cations separated by an oxygen ion. Each cation contains single unpaired electron in the d-orbital, and the oxygen has two p electrons in the outermost occupied orbital. Virtual hopping of the oxygen 2p electrons is taking place during the oxygen-mediated superexchange interaction between the transition metal ions. The O^{2-} ion has fully occupied triply degenerate $\left(2p_x,\ 2p_y,\ 2p_z\right)$ orbitals (figure 1.4 (a)). The e_g orbitals $(d_{z^2},\ d_{x^2-y^2})$ of the cations point along the crystal axes along with the oxygen 2p-orbitals. A repulsion between

electrons in the oxygen p-orbital and electrons in the transition metal e_g d-orbitals increases the energy of the e_g orbitals. i.e. the five d orbitals in transition metal oxide systems are split into triply degenerate lower energy $t_{2g}\left(d_{xy}, d_{yz}, d_{xz}\right)$ and doubly degenerate high energy e_g orbitals $(d_{z^2}, d_{x^2-y^2})$ as shown in figure 1.4 (b). In transition metal oxides, the d-orbitals of the transition elements overlap each other via the p-orbital of O anions, resulting in superexchange interaction. A virtual hopping of electrons is taking place during superexchange interaction. Some semi-empirical rules are developed to predict the superexchange interaction, which is known as the Goodenough-Kanamori-Anderson (GKA) rules [34, 35]. GKA rules are illustrated for the case of Mn_{3+} in $LaMnO_3$ as shown in figure 1.5 [36].

According to this rule,

(i) The superexchange interaction between ions with two half-filled or two empty d-orbitals located at 180º angles will be strongly antiferromagnetic according to Pauli's exclusion principle.

(ii) The superexchange interaction between filled and half-filled d-orbitals or empty and half-filled d-orbitals located at 180º angles will be weak FM.

(iii) The superexchange interaction between filled and vacant orbitals located at 180º can be either antiferromagnetic or ferromagnetic, but generally, favors ferromagnetic.

(iv) The superexchange interaction between two half-filled d-orbitals located at 90º is weak ferromagnetic.

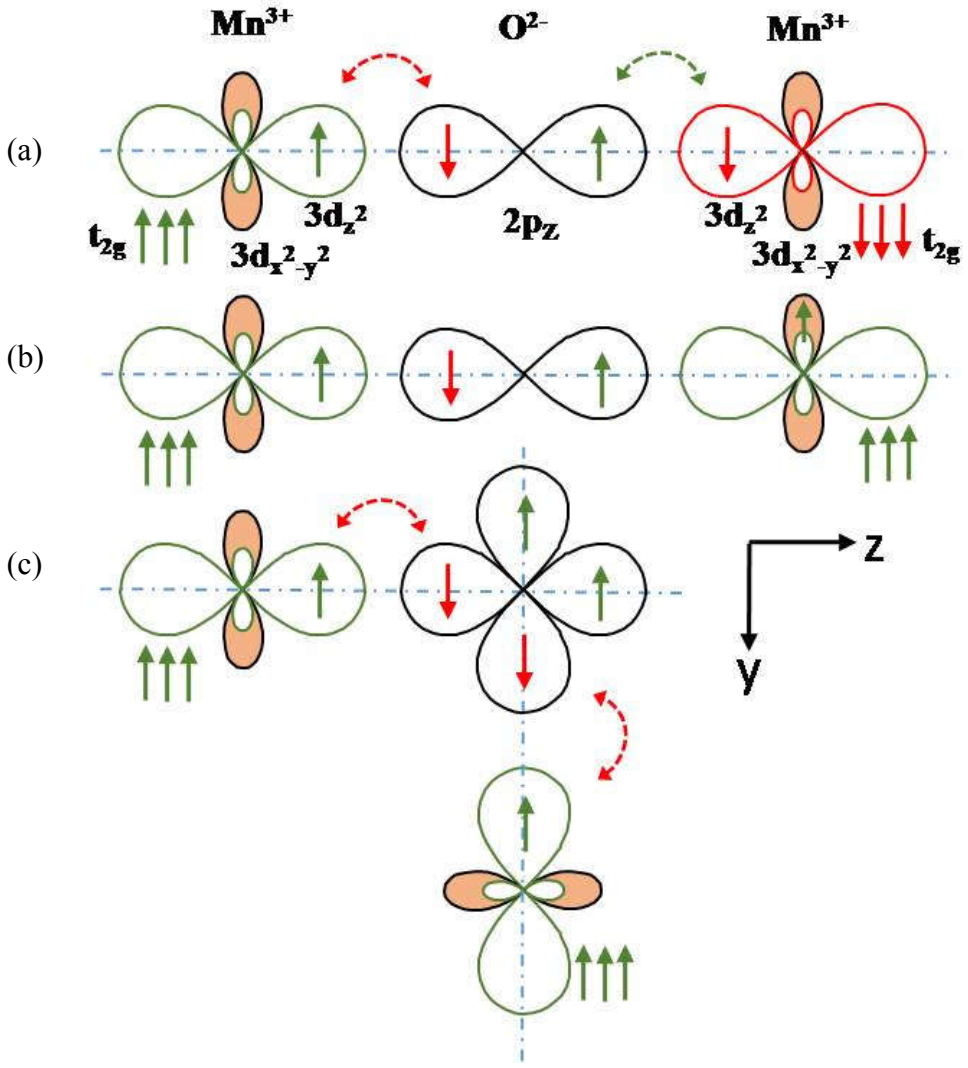

Figure 1.5. Superexchange and GKA rules illustrated for the (a) AFM and (b, c) FM exchange interactions.

1.2.1.1.2 Double exchange interaction

The double exchange interaction arises between ions of different oxidation states. The double exchange interaction was proposed by Zener in 1951 [37]. Consider the 180º interaction between Mn^{3+} and Mn^{4+} mediated by O ion. A real hopping of electron between Mn^{3+} (t_{2g}^3 e_g^1) and Mn^{4+} (t_{2g}^3 e_g^0) ions through O^{2-} is taking place in double exchange. Suppose the O is giving its spin-up electron to the

e_g orbital of Mn^{+4}, the vacant p orbital of O will be filled by an electron from the e_g orbital of Mn^{+3}, as in $LaMnO_3$, as illustrated in figure 1.6 [36]. The extra electron of the e_g orbital of Mn^{3+} ion travel back and forth between Mn^{3+} and Mn^{4+} ions retaining its spin where the spin is coupled with those of both the ion cores (t_{2g}). The real hopping of electrons (delocalization) reduces the kinetic energy. Thus the overall energy saving during the double exchange interaction leads a ferromagnetic alignment of spins of neighboring ions.

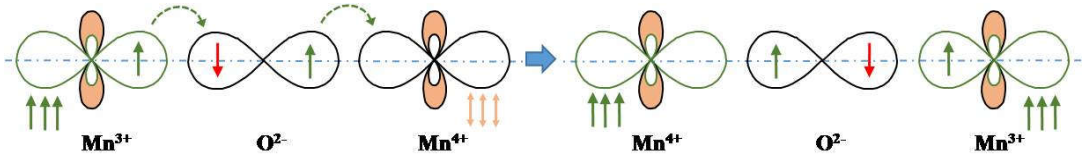

Figure 1.6. The double exchange between the $3d_{z^2}$ orbital of Mn^{3+} and Mn^{4+} ion via the $2p_z$ orbital of an O^{2-} ion.

1.2.1.2 Types of magnetic materials

Magnetism in materials is originated because of the spin and orbital moments associated with each atom present in the material and depending on the exchange interactions involved in such system. Magnetic materials are classified into different types based on their response to applied magnetic fields. Various classes of magnetic behavior are diamagnetism, paramagnetism, ferromagnetism, ferrimagnetism, and antiferromagnetism. In some magnetic materials, a competition between different types of magnetic interactions may occur. Materials with Griffiths-like phase and spin glass are examples of such material systems where more than one magnetic interaction predominates. Many perovskites are known to exhibit all these magnetic phases at various temperature regions.

1.2.1.2.1 Diamagnetism

Application of a magnetic field on a diamagnetic material induces an opposite magnetic field within the material which remains constant over a wide range of temperatures. Thus the diamagnetic materials are repelled by the applied magnetic field. On application of an external magnetic field, the magnetic moment gets increased with a negative slope as shown in figure 1.7 (a). Also, on increasing the temperature, the negative susceptibility stays unaltered as given by the equation $\chi_m = -\frac{N\mu_0 e^2 \langle r^2 \rangle_{av}}{6m_e}$, where N is the number of atoms per unit volume, μ_0 is the permeability of free space, e is the charge of electron, $\langle r^2 \rangle$ is the average squared radius of the electron orbit and m_e is the mass of electron [38]. It is portrayed in figure 1.7 (b).

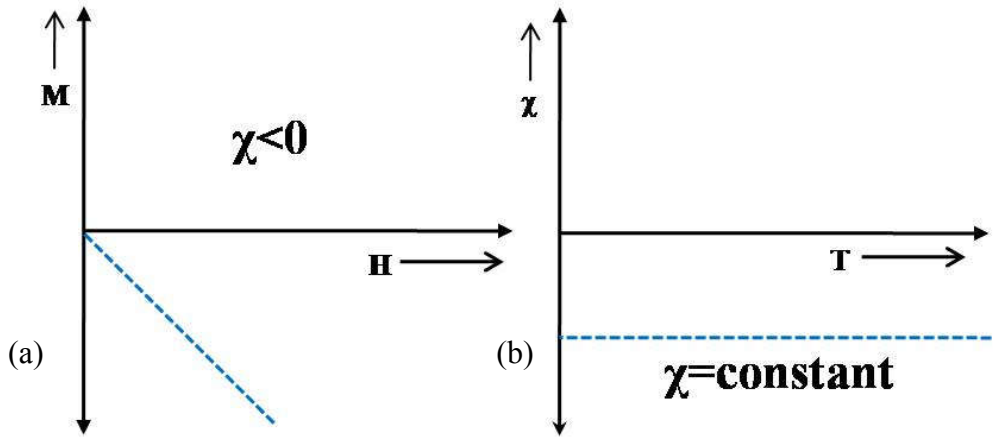

Figure 1.7 (a) Magnetic moment with field and (b) Susceptibility with temperature for a diamagnetic material

1.2.1.2.2 Paramagnetism

On application of an external magnetic field, a magnetic field is induced inside a paramagnetic material in the direction of the field. Thus, in reverse to the diamagnetic materials, paramagnetic materials are attracted by an externally applied magnetic field. The paramagnetic susceptibility is given by Curie's law as $\chi_m = \frac{N\mu_0\mu_{eff}^2\mu_B}{3k_BT} = \frac{C_W}{T}$ where C_W is the Curie constant and k_B is Boltzmann's constant, μ_B the Bohr magneton, T is the temperature and μ_{eff} is the effective magnetic moment of the paramagnetic ions [39]. μ_{eff} is calculated by using the equation $\mu_{eff} = g\sqrt{J(J+1)}$ where g is the Lande g factor $g = \frac{3J(J+1) + S(S+1) - L(L+1)}{2J(J+1)}$, provided S, L and J are spin, orbital and total angular momentum quantum numbers respectively. The variation of the magnetic moment with magnetic field and susceptibility with the temperature of a paramagnetic material is shown in figure 1.8 (a) and (b) respectively.

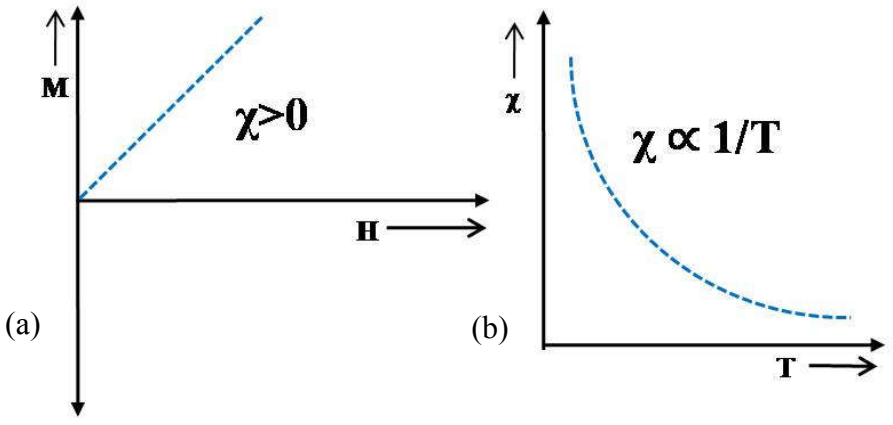

Figure 1.8 (a) Magnetic moment with field and (b) Susceptibility with temperature for a paramagnetic material

1.2.1.2.3 Ferromagnetism

The atomic moments in a ferromagnetic material exhibit very strong interactions that are produced by electronic exchange forces, resulting in a parallel alignment of atomic moments. These materials have a spontaneous magnetization and a magnetic ordering temperature (T_C) and can retain the magnetization once the magnetic field is removed. The magnetic moment shows a complex dependence with the applied magnetic field as shown by the hysteresis loop in figure 1.9 (a). Even on the removal of the field, the magnetic moment has a nonzero value called remanence magnetization (M_r). The amount of reverse magnetic field that should be applied to a ferromagnetic material to make the moment zero is called the coercive field (H_C). A ferromagnetic material becomes paramagnetic above T_C as described in figure 1.9 (b).

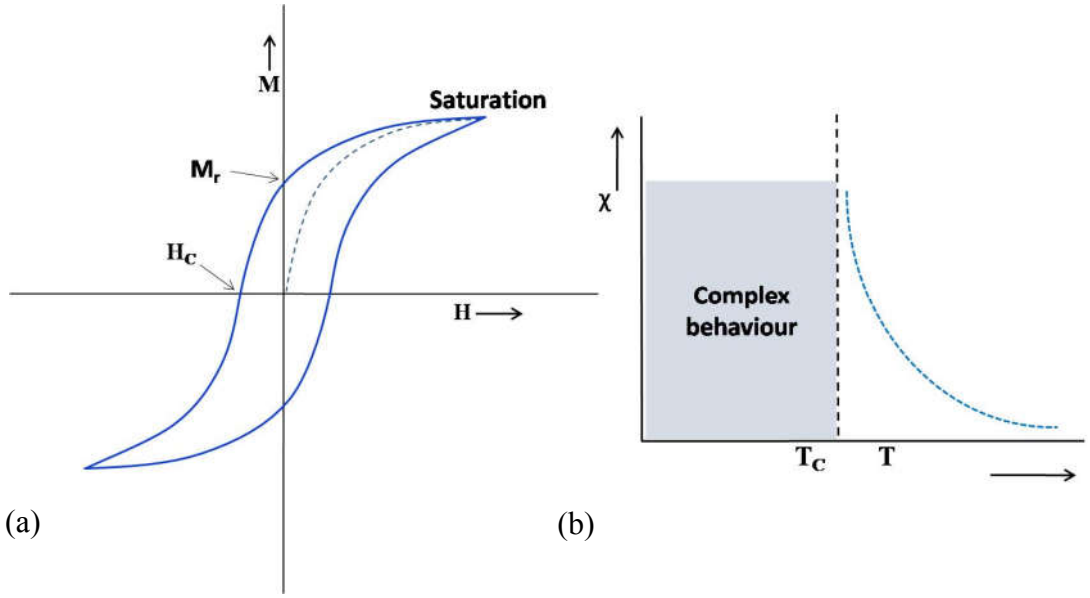

Figure 1.9 (a) Magnetic hysteresis loop and (b) Susceptibility with the temperature for a ferromagnetic material.

The ferromagnetic materials follow Curie-Weiss (CW) law $\chi = \frac{C_W}{T - \Theta}$ above transition (T_C), in the paramagnetic region, where C_W is the Curie constant, Θ is the Curie temperature. In most cases, the Θ and T_C are same.

1.2.1.2.4 Ferrimagnetism

A ferrimagnetic material is the one that has a number of atoms with opposing magnetic moments of unequal magnitude. The ferrimagnetic material also has got a spontaneous magnetization. The magnetic moment with field and temperature follows almost the same behaviour as that of ferromagnets.

1.2.1.2.5 Antiferromagnetism

Antiferromagnetic material is one that has populations of atoms with opposing magnetic moments of equal magnitude and the net magnetic moment is zero. Antiferromagnetism is also a manifestation of ordered magnetism, similar to ferromagnetism and ferrimagnetism. The antiferromagnetic order vanishes and becomes paramagnetic above a particular temperature called Neel temperature (T_N), as shown in figure 1.10. Antiferromagnetic materials also follow the CW law, where the Curie temperature Θ is negative.

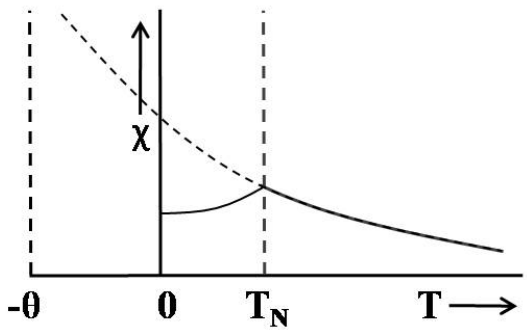

Figure 1.10 Susceptibility with temperature of an AFM material.

1.2.1.2.6 Griffiths-like phase

R B Griffiths originally proposed Griffiths-like phase (GP) as a nonanalytic behavior of random ising ferromagnet above the critical temperature (T_C) where a ferromagnetic phase get diluted with an increasing paramagnetic contribution when the temperature is increased [40]. In other words, the Griffiths-like phase is a diluted ising ferromagnet [40].

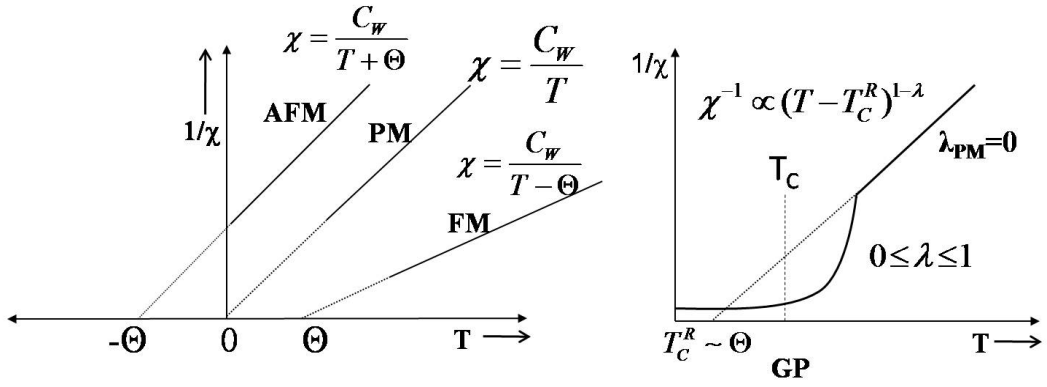

Figure 1.11 Inverse susceptibility vs. temperature for antiferromagnetic (AFM), paramagnetic (PM), ferromagnetic (FM), and Griffiths-like phase (GP).

For certain materials, the inverse susceptibility versus temperature plot shows a sharp deviation from CW law at a particular temperature (above T_C) called Griffiths temperature (T*). This deviation is reduced as the external magnetic field is increased. This is a characteristic feature of a Griffiths-like phase. The susceptibility of a paramagnetic material will follow the Curie law $\chi^{-1} = \frac{T}{C_W}$ and that of a ferromagnetic material follows the CW law $\chi^{-1} = \frac{T-\Theta}{C_W}$ above the transition point. Since the material contains both paramagnetic and ferromagnetic correlations above transition temperature for the case of Griffiths-like phase, the susceptibility of

a Griffiths-like phase shows a deviation from the CW law above T_C. On reaching the Griffiths temperature (T*), the material becomes completely paramagnetic and follows the CW law (above T*). A power law $\chi^{-1} \propto (T - T_C^R)^{1-\lambda}$ is used to fit the susceptibility of a Griffiths-like phase, provided $0 \leq \lambda < 1$ where T_C^R is the critical temperature of the random FM [12, 41-51]. The T_C^R is the point which gives a λ_{PM} value close to 0 above T* such that the power law becomes the CW law in the paramagnetic region. The Griffiths-like phase is more clearly observable at low magnetic fields where the λ_{GP} is close to 1. λ_{GP} reduces to 0 as the field is increased, where the susceptibility follows the CW law. Variation of the inverse susceptibility as a function of temperature for antiferromagnetism, paramagnetism, ferromagnetism, and Griffiths-like phase are shown in figure 1.11.

1.2.1.2.7 Spin glass materials

A spin glass is a disordered magnetic material whose spins are not aligned in a regular pattern as in ordered magnetic materials. This can be due to the competing magnetic orders present in the system simultaneously. The presence of competing ferromagnetic, ferrimagnetic, antiferromagnetic systems in the material offers a complex frustrated magnetism in these materials with a short-range magnetic order. The field cooled, and the zero-field cooled thermomagnetic plot will show a bifurcation at low temperature due to the metastable nature of the spin glasses. They also show relaxation when subject to an external alternating magnetic field. Also, they exhibit a memory and aging property under zero-filed cooled condition. In a typical spin glass material, all the spins are independent and non-interacting each other. In some cases, the independent spins form locally correlated clusters. Such

materials are known as clustered spin glass or simply cluster glass. Cluster glass materials are composed of independent and non-interacting clusters of magnetic spins. The glassy nature of a magnetic system is determined from the ac susceptibility measurements with varying frequency. If a frequency dependent peak shift is appearing in the real or imaginary part of the AC susceptibility, then the material is a spin glass. In the zero-field cooled memory test, the magnetization shows a memory of an intermediate halting temperature in the spin glass region. Also, during the aging measurement, the magnetic moment follows a stretching relation with respect to time.

1.2.2 Electrical properties

Materials are classified into conductors, semiconductors, and insulators based upon their opposition to the flow of electric current through them. Conductors have a large number of free electrons as charge carriers and allow an easy passage to the flow of current. Semiconductors allow the current flow in a restricted manner whereas the insulators offer a very high resistance to the flow of current through them.

The electrical properties of materials are described by the band structure. The balance between interatomic interactions (electronic bandwidth) and electron-electron interactions causes changes in the electrical conductivity. If the conduction band is empty, then the materials are band insulators. If the conduction band is partially occupied and interatomic interactions are less than the electron-electron interaction, then the electrons are localized. If the conduction band is partially occupied and interatomic interactions are greater than the electron-electron

interaction, then the electrons can be itinerant. In transition metal oxides, s electrons enter into deeper bonding orbitals, and the conduction bands are mostly with oxygen 2p and transition metal d orbitals. The s orbitals are the principal constituent of the conduction band in simple metals whereas, in transition metal oxides, the directionality of the p and d orbitals and the strong Coulomb interaction in the d orbital cloud manifest the charge transport phenomenon.

Usually, the transition metal oxides with disordered double perovskite structure are insulators in which the electrical transport is through hopping conduction mechanism [52]. The presence of electrons, phonons and their interaction greatly influence the electronic states as well as phonon states in the oxide system. Hopping conduction is the electrical conduction in which the electrons or polarons transport via hopping between localized states. A distorted lattice can invoke polaron in the lattice which is a quasiparticle consisting of a conduction electron or hole together with its self-induced polarization [53]. The electrons and/or polarons hopping can take place in various cases as described below and in figure 1.12.

1. Hopping from a state to another state of higher energy via thermally assisted tunneling.

2. Hopping between states of equal energy via tunneling, which does not require thermal energy.

3. Hopping from a state to another state of lower energy via tunneling process by emitting photon(s). It does not depend on temperature.

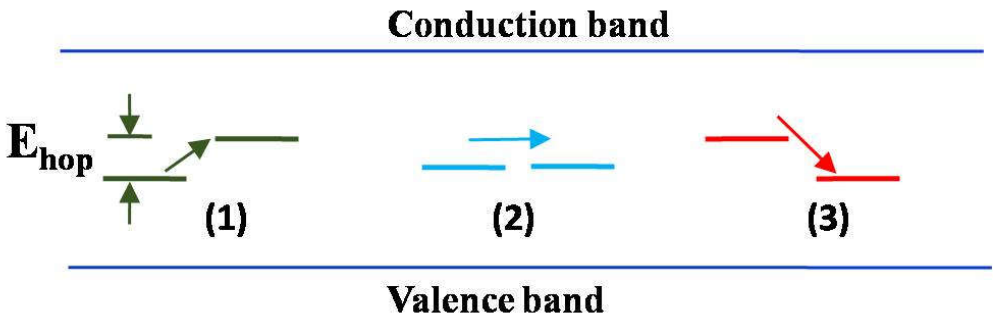

Figure 1.12. Electron transport between localized states in various cases (1) thermally assisted tunneling (2) tunneling and (3) tunneling with the emission of the photon.

For the occurrence of hopping conduction, the following conditions should satisfy.

1. Overlapping of the wavefunctions of the two localized state.

2. Occupied and empty states must be present. i.e. hopping should occur between states close to the Fermi level.

Various models are assumed to the hopping conduction mechanism in insulators and semiconductors. The main mechanisms include the Arrhenius thermal activation conduction or band gap model (TAC), nearest-neighbor hopping of small polarons (NN-SPH), and Mott's variable range hopping model (Mott – VRH).

In Arrhenius model, the conduction mechanism is thermally activated, where the resistivity follows the Arrhenius law $\rho = \rho_0 \exp\left(\frac{E_A}{k_B T}\right)$ provided ρ_0 is a constant, E_A is the activation energy, and k_B is the Boltzmann constant.

In Mott's variable range hopping (VRH) mechanism, the charge carriers hop to states at variable ranges and energy [54]. It follows the equation

$\rho = \rho_0 \exp\left(\frac{T_0}{T}\right)^{1/4}$, where ρ_0 and T_0 are constants. The density of localized carrier states in the Fermi level $N(E_F)$ is determined from T_0 by using the expression $T_0 = \frac{24}{\pi k_B N(E_F) \in^3}$ where $\in$ is the decay/percolation length of the localized wave function. The hopping energy E_A to nearby sites is not universal, but depends on the temperature and can be obtained from T_0 by using the equation $E_A = \frac{k_B}{4} T_0^{\frac{1}{4}} T^{\frac{3}{4}}$. The range of hopping R depends on $\in$, $N(E_F)$ and T as $R = \left[\frac{9 \in}{8\pi k_B N(E_F) T}\right]^{1/4}$. It means that the hopping will be towards variable sites (of various R) having varying energies, at lower temperatures.

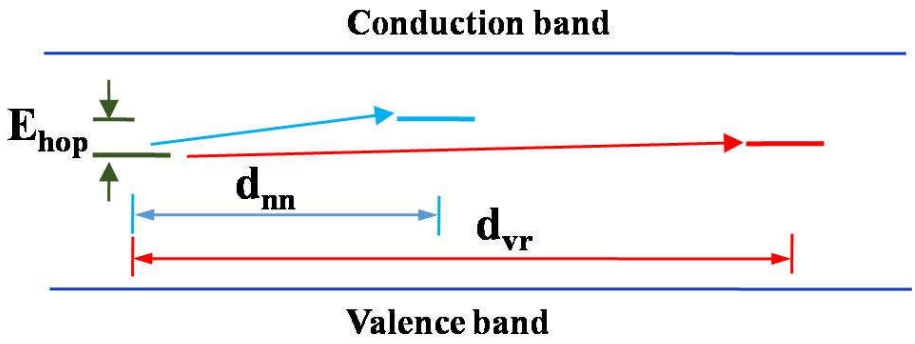

Figure 1.13 Variable range hopping and nearest neighbor hopping.

Generally, at higher temperatures, sufficient thermal energy will be available that can activate the nearest neighbor hopping of small polarons between the localized donor and acceptor sites [55]. The NN-SPH model is described by the equation $\rho = Ak_B T \exp\left(\frac{E_A}{k_B T}\right)$, where A comprises of different temperature

independent parameters, E_A is the activation energy (required to activate a polaron). The VRH and NN-SPH are depicted in figure 1.13.

In some cases, both the VRH and the SPH mechanisms come together in the conduction process. The variable range hopping of small polarons (VR-SPH) [56] is expressed as a combination of the two corresponding equations as $\rho = BT\exp\left(\frac{E_A}{k_B T} + \left(\frac{T_0}{T}\right)^{1/4}\right)$ where B is a constant.

1.2.3 Specific heat

The specific heat (C) is the amount of heat per unit mass required to increase the temperature of a substance by one degree Kelvin or Celsius. Specific heat can give information about lattice dynamics. Certain transition temperatures like magnetic, charge ordering, etc. show distinct anomalies in the specific heat data as a function of temperature. The low-temperature C follows the equation $C= \gamma T+\beta_3 T^3+\beta_5 T^5+\beta_7 T^7$ where γT is the electronic specific heat, and the higher order T terms are contributions arising from lattice and phonons [57]. Heat in a solid is transported by both electrons and phonons in the lattice. From the electronic contribution to the specific heat, information regarding the low-temperature charge carriers is obtained.

1.2.4 Dielectric properties

A dielectric material is an insulator that can be polarized on the application of a voltage difference across it. Electric charges do not flow through an insulator material but slightly deviates from their equilibrium position when a potential difference is applied. This creates a dielectric polarization where the positive and

negative charges are separated by a distance, with the formation of electric dipoles. The dielectric response of a material arises from electronic contribution and lattice contribution. The electronic contribution is due to the movement of the electron clouds with respect to the ions, and the lattice contribution arises from the movement of the ions. The dielectric constant is related to the easiness of material to get polarized, and the loss tangent is related to the absorption and dissipation of electromagnetic energy in the form of heat by the material when placed in a field. Usually, the presence of phonons, polarons and the extrinsic factors like grain boundaries, electrode/sample interface (contact point), electronically separated phases, inhomogeneities, imperfections, etc. incorporates the dielectric behavior of a material.

The electric dipoles present in a dielectric material tend to relax when placed in a frequency dependent field. Usually, the relaxation time $\tau = (2\pi f)^{-1}$ for a particular frequency f follows the Arrhenius law (thermally activated relaxation) $\tau = \tau_0 \exp\left(\frac{E_a}{k_B T_m}\right)$ where τ_0 is the Debye relaxation time, E_A is the activation energy and T_m is the temperature where the dielectric data shows a maximum for a particular f.

1.2.5 Magnetoresistance and Magnetodielectric coupling

Magnetoresistance (MR) is the tendency of material to change the value of its electrical resistance when subjected to an externally-applied magnetic field. Magnetodielectric (MD) coupling is established as a change in the dielectric constant of the material on application of an external magnetic field. The

magnetoresistance is calculated by the expression $\mathrm{MR}(\%) = \frac{\rho_H - \rho_0}{\rho_0} \mathrm{x}100$, where ρ_H and ρ_0 are the resistivities with and without a magnetic field. The MD can be calculated by the equation $\mathrm{MD}(\%) = \frac{\varepsilon_H - \varepsilon_0}{\varepsilon_0} \mathrm{x}100$ and the magnetodielectric loss (MDL) coupling can be calculated by the equation $\mathrm{MDL}(\%) = \frac{\tan \delta_H - \tan \delta_0}{\tan \delta_0} \mathrm{x}100$ where ε_H, and $\tan \delta_H$ are the dielectric constant and loss tangent in a magnetic field (H), and ε_0, and $\tan \delta_0$ are the dielectric constant and the loss tangent in zero magnetic field.

Varying the resistance and dielectric property of a material upon the application of an external magnetic field has potential applications in spintronics and MR/MD based devices like magnetic read heads, sensors, nonvolatile memories, etc. [17]. Strongly correlated electronic systems create competing magnetic and electronic phases along with an interplay between the spin and charge order. Such systems exhibit a coupling between the magnetic order and the charge order mostly around a magnetic or electric transition [7, 15, 16, 20, 58-62]. A magnetoresistance is observed in ferromagnetic conductor around a magnetic transition while MD coupling is typically found around a paramagnetic to ferromagnetic transition where the charges are localized to possess insulating or semiconducting behavior [15, 16, 20, 58-62].

1.3. Objectives and motivation of the work

1.3.1 Motivation behind the present investigation

Magnetism in double perovskites arises due to the presence of superexchange interactions. A possibility of double exchange interaction is there if the double perovskite containing cations of the same element with oxidation state differs by one. The exchange interaction becomes rather complex and competing if the double perovskite material is having the B-site cations of comparable size and charge. Short-range magnetic interactions B-O-B' and long-range magnetic interactions B-O-B'-O-B and B'-O-B-O-B' are also present in double perovskite systems. Usually, the short-range B-O-B' interactions are the strongest interaction. Thus double perovskites provide a playground for a variety of magnetic properties including magnetic frustration and low-dimensional magnetism. Usually, double perovskites are insulators or semiconductors. The flow of charges through them is lead by various hopping conduction mechanisms. Since most of the double perovskites are insulators, they can also show dielectric polarization and dielectric relaxation. As they have a magnetic and electric phase existing, a possible coupling between the magnetic and electronic phases are expected which may give rise to magnetoresistance and magnetodielectric coupling properties. Thus the wide diversity in the magnetic, transport and magnetotransport properties of the double perovskites, based on the local surrounding of the B-site cations, inspired to choose the double perovskite family as the prime focus of the present investigation. For a better understanding of the inherent interactions in double perovskites, and design or synthesis of potential materials, basic materials research is necessary.

Table 1.1. Some prominent reports on % MD shown by La_2NiMnO_6 and La_2CoMnO_6

La_2NiMnO_6		
% MD	**At (K)**	**Reason**
+ 50	115	Influence of magnetic field on the dipolar relaxation [20]
+4	80	Short range FM ordering [18]
+2.2	220	Extrinsic origin by interfacial polarization [63]
-15	250	Spin-lattice coupling [27]
-20	270	Glassy dielectric properties [64]
-30	220	Dielectric relaxation and FM transition [65]
+ & -	depends	MD based upon the annealing temperature [66]
La_2CoMnO_6		
+11	220	Coupling of dipolar relaxation with magnetic order [16]
+110	90	Spin–lattice anomaly below T_C [19]

The double perovskites with general formula La_2BMnO_6 (B=Ni and Co) have attracted researchers' interests because of their ferromagnetic behavior with frustrated magnetism at low temperature, and the colossal dielectric constant with very high magnetodielectric coupling [64, 67]. These materials are magnetic double perovskites with the existence of Griffiths-like phase. They show semiconducting or

insulating behaviour according to the composition and synthesis conditions. The conduction mechanisms are governed by combinations of various hopping conduction mechanisms [64, 67]. Hence the present work opted the La_2BMnO_6 series with B= Fe, Cu, and Cr where the B-site cation (Ni / Co) of the La_2NiMnO_6 and La_2CoMnO_6 are replaced by their neighboring transition element cations.

Among the double perovskite oxide family, La_2NiMnO_6 has been widely studied since it shows a wide variety of structural, magnetic and electronic properties. Recently, the double perovskite La_2CoMnO_6 has also got the attraction of researchers since it also follows the peculiar magnetism and magnetodielectric coupling similar to that of La_2NiMnO_6. In the majority of the cases, the synthesized materials are not perfectly ordered since the radii of the B-site cations (Ni/Co and Mn) are comparable. So, the possibility of anti-site defect reduces the order of the double perovskite system. Thus, in our present work, the term perovskite and double perovskites are equally valid to illustrate the class of La_2BMnO_6 (or $LaB_{0.5}Mn_{0.5}O_3$) compounds.

La_2NiMnO_6 is ferromagnetic with T_C at 280 K and existence of ferromagnetic correlations above T_C [68, 69]. A recent study reported La_2NiMnO_6 nanoparticles with T_C at 350 K [70]. A frustrated magnetic behavior is shown by La_2NiMnO_6 and La_2CoMnO_6 nanoparticles with T_C at 275 K and 210 K respectively [71]. The ferromagnetic correlations above T_C are induced by antisite defects against long-range ordering of the Ni/Mn sublattice or due to the strong spin-phonon coupling effect [68, 69]. A giant dielectric constant step and a relaxor-like dielectric behavior are reported in La_2NiMnO_6 as a consequence of Ni^{2+} and Mn^{4+} cationic ordering [63, 72]. Dielectric relaxation of La_2NiMnO_6 follows the Arrhenius law,

and the DC conductivity follows the variable range hopping mechanism [72]. A partly disordered La_2NiMnO_6 is reported to possess a reentrant spin glass-like magnetism and glassy dielectric properties with frustrated FM phase near 270 K and a very large MD coupling over a broad range of temperatures (MD>16% at 300 K) [64]. A small extrinsic MD is observed in La_2NiMnO_6 which is not showing FM correlations above T_C [63]. A negative MR effect (-10 %) is observed for La_2NiMnO_6 at 250 K in 50 kOe, in which the low-field MR is originated from the spin-dependent electron hopping between the ferromagnetic domains and the high field MR is originated from the suppression of scattering from the spin defects arising from the Ni/Mn anti-site disorders [73]. La_2CoMnO_6 synthesized at low temperature has a rhombohedral phase with T_C at 225 K, and is converted to orthorhombic phase with T_C at 150 K when treated at temperatures above 1200 ºC [74, 75]. The crystallographic and magnetic structure of La_2CoMnO_6 show variation as per the sample annealing temperature [74]. A low T_C is observed for a monoclinic phase, and a high T_C is reported for a rhombohedral phase of La_2CoMnO_6 as a result of the difference in exchange interaction arising from variations in the Co-O-Mn bond angles and distances [76]. Large MD coupling of 11 % and 8 % at 100 kHz near the two FM transitions were observed in La_2CoMnO_6 as a result of the coupling of dipolar relaxation with magnetic order parameter [16]. Intrinsic coupling between magnetic and dielectric orders and extrinsic effect from Maxwell-Wagner model combined with MR property contribute to MD effect in the La_2CoMnO_6 nanoparticles [16]. Dielectric relaxation with high dielectric constant is observed for La_2CoMnO_6 that constitute the low-frequency Maxwell-Wagner relaxation and the high-frequency Debye-type relaxation processes and an MD of 35 % is obtained in

50 kHz and 5 kOe at 120 K [77]. Recently, a very high MD of +110 % is observed for La_2CoMnO_6 nanoparticles at 90 K in 1 kHz and 50 kOe [19]. Some of the reports on the % MD observed for La_2NiMnO_6 and La_2CoMnO_6 are tabulated in Table 1.1. Also, many manganite materials are known to exhibit MR in the GP region [78-83]. The presence of quenched disorder, the J-T distortion and the hopping of carriers has a crucial role in the occurrence of GP [84].

1.3.2 Objectives of the present investigation

The reports on La_2NiMnO_6 and La_2CoMnO_6 with a variety of properties with different physical origin encouraged to research La_2BMnO_6 with B=Fe, Cu, and Cr. The Ni/Co-O-Mn bond angle and distances determined the wide range of magnetic, transport and magnetotransport properties of La_2NiMnO_6 and La_2CoMnO_6. Hence studying the magnetic, transport, and magnetotransport properties of La_2FeMnO_6, La_2CuMnO_6, and La_2CrMnO_6 are expected to offer good scientific challenge and thus taken as the problem for the investigation. For this reason, the main objectives of the present investigation are as follows.

- Synthesis of phase pure La_2BMnO_6 (B=Fe, Cu, and Cr)
- Identification of the magnetic structure
- Studies of DC transport and magnetoresistance properties
- Studies of dielectric and magnetodielectric properties

1.4 References

[1] V.M. Goldschmidt, Naturwissenschaften, 14 (1926) 477-485.

[2] M.A. Peña, J.L.G. Fierro, Chemical Reviews, 101 (2001) 1981-2018.

[3] H. Yakel, Acta Crystallographica, 8 (1955) 394-398.

[4] Y. Tokura, Y. Tomioka, Journal of Magnetism and Magnetic Materials, 200 (1999) 1-23.

[5] J.B. Philipp, P. Majewski, L. Alff, A. Erb, R. Gross, T. Graf, M.S. Brandt, J. Simon, T. Walther, W. Mader, D. Topwal, D.D. Sarma, Physical Review B, 68 (2003) 144431.

[6] C.S. Housecroft, A. G., Inorganic Chemistry, Prentice Hall, 2008.

[7] C.N.R. Rao, B. Raveau, Colossal Magnetoresistance, Charge Ordering and Related Properties of Manganese Oxides, World Scientific, 1998.

[8] K.I. Kobayashi, T. Kimura, H. Sawada, K. Terakura, Y. Tokura, Nature, 395 (1998) 677-680.

[9] P. Baettig, C. Ederer, N.A. Spaldin, Physical Review B, 72 (2005) 214105.

[10] M.T. Anderson, K.B. Greenwood, G.A. Taylor, K.R. Poeppelmeier, Progress in Solid State Chemistry, 22 (1993) 197-233.

[11] L. Balcells, J. Navarro, M. Bibes, A. Roig, B. Martínez, J. Fontcuberta, Applied Physics Letters, 78 (2001) 781-783.

[12] J. Pezhumkattil Palakkal, P.N. Lekshmi, S. Thomas, K.G. Suresh, M.R. Varma, RSC Advances, 5 (2015) 105531-105536.

[13] M.K. Wu, D.Y. Chen, F.Z. Chien, S.R. Sheen, D.C. Ling, C.Y. Tai, G.Y. Tseng, D.H. Chen, F.C. Zhang, Zeitschrift für Physik B Condensed Matter, 102 (1996) 37-41.

[14] E. Dagotto, Science, 309 (2005) 257-262.

[15] A.P. Ramirez, Journal of Physics: Condensed Matter, 9 (1997) 8171.

[16] A. Venimadhav, D. Chandrasekar, J. Krishna Murthy, Applied Nanoscience, 3 (2013) 25-28.

[17] A.K. Kundu, Magnetic Perovskites, Springer India, 2016.

[18] K.D. Chandrasekhar, A.K. Das, A. Venimadhav, Journal of Physics: Condensed Matter, 24 (2012) 376003.

[19] J.K. Murthy, K.D. Chandrasekhar, S. Murugavel, A. Venimadhav, Journal of Materials Chemistry C, 3 (2015) 836-843.

[20] P. Padhan, H.Z. Guo, P. LeClair, A. Gupta, Applied Physics Letters, 92 (2008) 022909.

[21] J.W. Seo, E.E. Fullerton, F. Nolting, A. Scholl, J. Fompeyrine, J.P. Locquet, Journal of Physics: Condensed Matter, 20 (2008) 264014.

[22] P. Mondal, D. Bhattacharya, P. Choudhury, P. Mandal, Physical Review B, 76 (2007) 172403.

[23] J. Kanamori, Journal of Physics and Chemistry of Solids, 10 (1959) 87-98.

[24] I. Weinberg, P. Larssen, Nature, 192 (1961) 445-446.

[25] J.F. Bringley, B.A. Scott, S.J. La Placa, T.R. McGuire, F. Mehran, M.W. McElfresh, D.E. Cox, Physical Review B, 47 (1993) 15269-15275.

[26] D.P. Belanger, T. Keiber, F. Bridges, A.M. Durand, A. Mehta, H. Zheng, J.F. Mitchell, V. Borzenets, Journal of Physics: Condensed Matter, 28 (2016) 025602.

[27] N.S. Rogado, J. Li, A.W. Sleight, M.A. Subramanian, Advanced Materials, 17 (2005) 2225-2227.

[28] Y.Q. Lin, X.M. Chen, Journal of the American Ceramic Society, 94 (2011) 782-787.

[29] S. Blundell, Magnetism in Condensed Matter, OUP Oxford, 2001.

[30] H.A. Kramers, Physica, 1 (1934) 182-192.

[31] P.W. Anderson, Physical Review, 79 (1950) 350-356.

[32] J.B. Goodenough, Journal of Physics and Chemistry of Solids, 6 (1958) 287-297.

[33] J.B. Goodenough, Physical Review, 100 (1955) 564-573.

[34] J.B. Goodenough, Magnetism and Chemical Bond, Interscience, New York/London, 1963.

[35] D.A.C. John N. Lalena, Principles of Inorganic Materials Design, John Wiley & Sons, New York, 2005.

[36] O. Matthias, Journal of Physics D: Applied Physics, 45 (2012) 033001.

[37] C. Zener, Physical Review, 82 (1951) 403-405.

[38] J.M.D. Coey, Magnetism and Magnetic Materials, Cambridge University Press, 2009.

[39] B.D. Cullity, C.D. Graham, Introduction to magnetic materials, Second ed., IEEE Press, Wiley, A John Wiley and Sons, Inc., Publication.

[40] R.B. Griffiths, Physical Review Letters, 23 (1969) 17-19.

[41] H.S. Nair, D. Swain, H. N., S. Adiga, C. Narayana, S. Elzabeth, Journal of Applied Physics, 110 (2011) 123919.

[42] A.H. Castro Neto, G. Castilla, B.A. Jones, Physical Review Letters, 81 (1998) 3531-3534.

[43] C. Magen, P.A. Algarabel, L. Morellon, J.P. Araújo, C. Ritter, M.R. Ibarra, A.M. Pereira, J.B. Sousa, Physical Review Letters, 96 (2006) 167201.

[44] S. Guo, D.P. Young, R.T. Macaluso, D.A. Browne, N.L. Henderson, J.Y. Chan, L.L. Henry, J.F. DiTusa, Physical Review Letters, 100 (2008) 017209.

[45] A. Ślebarski, J. Goraus, M. Fijałkowski, Physical Review B, 84 (2011) 075154.

[46] W. Jiang, X. Zhou, G. Williams, Y. Mukovskii, K. Glazyrin, Physical Review Letters, 99 (2007) 177203.

[47] P. Tong, B. Kim, D. Kwon, T. Qian, S.-I. Lee, S.W. Cheong, B.G. Kim, Physical Review B, 77 (2008) 184432.

[48] W. Jiang, X. Zhou, G. Williams, Y. Mukovskii, K. Glazyrin, Physical Review B, 77 (2008) 064424.

[49] S. Zhou, Y. Guo, J. Zhao, L. He, L. Shi, The Journal of Physical Chemistry C, 115 (2011) 1535-1540.

[50] D. Bhoi, N. Khan, A. Midya, M. Nandi, A. Hassen, P. Choudhury, P. Mandal, The Journal of Physical Chemistry C, 117 (2013) 16658-16664.

[51] A.K. Pramanik, A. Banerjee, Physical Review B, 81 (2010) 024431.

[52] N. Tsuda, Nasu, K., Fujimori, A., Siratori., K., Electronic Conduction in Oxides Springer, New York, 2000.

[53] A. Taylor, Acta Crystallographica Section A, 29 (1973) 773-774.

[54] N.F. Mott, Metal-Insulator Transitions, Taylor and Francis, London 1990.

[55] R. Schmidt, A. Basu, A.W. Brinkman, Physical Review B, 72 (2005) 115101.

[56] S. Young, X. Xiaojun, Z. Yuheng, Journal of Physics: Condensed Matter, 12 (2000) 10475.

[57] M.R. Lees, O.A. Petrenko, G. Balakrishnan, D. McK. Paul, Physical Review B, 59 (1999) 1298-1303.

[58] G. Lawes, A.P. Ramirez, C.M. Varma, M.A. Subramanian, Physical Review Letters, 91 (2003) 257208.

[59] G. Catalan, Applied Physics Letters, 88 (2006) 102902.

[60] Q. Jiang, S.J. Gong, The European Physical Journal B - Condensed Matter and Complex Systems, 43 (2005) 333-338.

[61] K. Dey, A. Indra, D. De, S. Majumdar, S. Giri, ACS Applied Materials & Interfaces, 8 (2016) 12901-12907.

[62] C.-H. Yang, S.-H. Lee, T.Y. Koo, Y.H. Jeong, Physical Review B, 75 (2007) 140104.

[63] K.D. Chandrasekhar, A.K. Das, C. Mitra, A. Venimadhav, Journal of Physics: Condensed Matter, 24 (2012) 495901.

[64] D. Choudhury, P. Mandal, R. Mathieu, A. Hazarika, S. Rajan, A. Sundaresan, U.V. Waghmare, R. Knut, O. Karis, P. Nordblad, D.D. Sarma, Physical Review Letters, 108 (2012) 127201.

[65] G.M. Md, G. Arijit, J. Sannigrahi, B.K. Chaudhuri, Journal of Physics: Condensed Matter, 24 (2012) 295902.

[66] Z. Zhang, H. Jian, X. Tang, J. Yang, X. Zhu, Y. Sun, Dalton Transactions, 41 (2012) 11836-11840.

[67] J. Krishna Murthy, A. Venimadhav, Journal of Applied Physics, 111 (2012) 024102.

[68] H. Guo, A. Gupta, M. Varela, S. Pennycook, J. Zhang, Physical Review B, 79 (2009) 172402.

[69] X. Luo, Y.P. Sun, B. Wang, X.B. Zhu, W.H. Song, Z.R. Yang, J.M. Dai, Solid State Communications, 149 (2009) 810-813.

[70] S. Ravi, C. Senthilkumar, Materials Letters, 164 (2016) 124-126.

[71] Y. Mao, J. Parsons, J.S. McCloy, Nanoscale, 5 (2013) 4720-4728.

[72] Y.Q. Lin, X.M. Chen, X.Q. Liu, Solid State Communications, 149 (2009) 784-787.

[73] Y. Guo, L. Shi, S. Zhou, J. Zhao, W. Liu, Applied Physics Letters, 102 (2013) 222401.

[74] P.A. Joy, Y.B. Khollam, S.N. Patole, S.K. Date, Materials Letters, 46 (2000) 261-264.

[75] V.L. Joseph Joly, S.D. Bhame, P.A. Joy, S.K. Date, Journal of Magnetism and Magnetic Materials, 261 (2003) 433-441.

[76] M. Viswanathan, P.S.A. Kumar, B. Venkata Srinu, N. Chandrabhas, A.K. Bera, S.M. Yusuf, Journal of Physics: Condensed Matter, 22 (2010) 346006.

[77] K. Manna, R.S. Joshi, S. Elizabeth, P.S.A. Kumar, Applied Physics Letters, 104 (2014) 202905.

[78] P.K. Siwach, H.K. Singh, O.N. Srivastava, Journal of Physics: Condensed Matter, 20 (2008) 273201.

[79] M.B. Salamon, S.H. Chun, Physical Review B, 68 (2003) 014411.

[80] M.B. Salamon, P. Lin, S.H. Chun, Physical Review Letters, 88 (2002) 197203.

[81] G.N. Rao, J.W. Chen, S. Neeleshwar, Y.Y. Chen, M.K. Wu, Journal of Physics D: Applied Physics, 42 (2009) 095003.

[82] J. Wanjun, Z. XueZhi, W. Gwyn, Y. Mukovskii, R. Privezentsev, Journal of Physics: Condensed Matter, 21 (2009) 415603.

[83] V.N. Krivoruchko, M.A. Marchenko, Y. Melikhov, Physical Review B, 82 (2010) 064419.

[84] A. Karmakar, S. Majumdar, S. Kundu, T.K. Nath, S. Giri, Journal of Physics: Condensed Matter, 25 (2013) 066006.

Chapter 2

Experimental Techniques

This chapter deals with the experimental procedures including the sample preparation of La_2BMnO_6, various characterization techniques utilized for the investigation and a brief description of their basic working principle.

2.1 Synthesis of La_2BMnO_6

The synthesis of ceramic materials with the desired stoichiometry is an important confront of research in the areas of materials science. It is done either by a mechanical treatment, or a heat treatment at higher temperatures or using chemical reactions from high-purity chemical solutions at low temperatures. The synthesis usually includes processes like milling, batching, mixing, forming, drying, firing, and assembly [1]. The two main categories of synthesis methods are mechanical methods and the chemical methods. The main synthesis techniques under the chemical method category include solid-state reaction method, liquid solution methods, and vapor phase reaction method [2]. The majority of the physical and chemical properties of materials have a direct or long-distant relationship with the way of synthesis. The crystal structure and lattice distortions have a significant influence on the physical properties of a perovskite. Also, the dielectric properties of a material depend on the density of the material [3]. Thus, to get reliable results with reproducible data on ceramic materials, a proper synthesis method has to be selected. Chemical synthesis is preferred to get the exact stoichiometry of a desired transition metal oxide perovskite with minimal impurity phase.

The solid-state reaction route is the most commonly used technique for the preparation of polycrystalline solids from a mixture of solid materials as starting materials. These solids are not reacting at room temperature for a reasonable period. They are subjected to very high temperatures for the reaction to take place at an appreciable rate. The technique involves the mixing of constituent oxides, carbonates, etc. of the cation element, in stoichiometric amounts and their subsequent heating at higher temperatures. The reaction between the constituent

oxides/carbonates is accelerated at high temperatures. Since the reaction rate is high in compact form, the powders are undergone grinding to fine particles and pelletizing to desired shapes by using a hydraulic press. The pellets are sintered at higher temperatures to get the final ceramic material with desired density. Higher temperatures are necessary to take place the reaction to overcome the slow diffusion rates between the solid materials. So, other synthesis methods have to be replaced the conventional solid state reaction synthesis method for synthesizing the perovskite oxide materials at comparatively low temperatures.

For the synthesis of oxides, soft chemical routes are found to be important for significantly lower temperature reactions [4]. The soft chemical approach employs chemical reactions such as co-precipitation, hydrolysis, ion exchange, sol–gel, acid leaching, etc. at considerably low temperatures compared to the solid state reaction method. The reagents are mixed in the liquid phase allowing the ions to be mixed at atomic scale with maximum homogeneity. It has an increased diffusion rate than that associated with the mixing of solid precursors in the solid state reaction synthesis. The ions in the liquid phase are co-precipitated or transformed into a gel (sol-gel method), dried and calcinated to obtain the final product. The sol-gel method is widely used for the synthesis of oxides as nanoparticles and thin film. The modified Pechini method is a common variant of the sol-gel method in which a complex gel undergoes pyrolysis. A chelation process is taking place between a hydroxyl carboxylic acid (e.g. citric acid) and metal cations in the form chlorides, nitrates, carbonates, or hydroxides with during the Pechini method [5, 6]. The cross-linked resin can provide a homogeneous mixing of the cations and has a less tendency for segregation during burning and calcinations [5, 6].

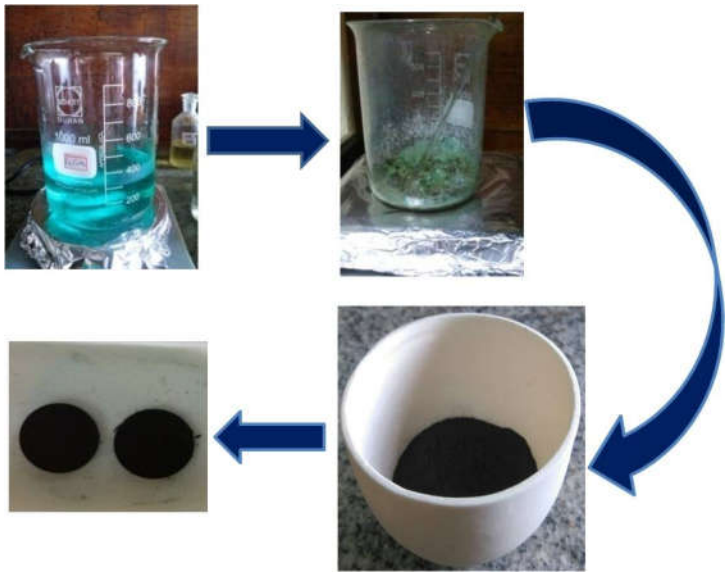

Figure 2.1 Various steps involved in the synthesis of La_2BMnO_6.

The perovskites La_2BMnO_6 (B = Fe, Cu, and Cr) samples were prepared in polycrystalline form by the citrate-gel combustion method, a modified Pechini method [6]. High purity chemicals $La(NO_3)_3.xH_2O$, $B(NO_3)_3.xH_2O$ and $Mn(NO_3)_2.xH_2O$ (Sigma-Aldrich, purity ~99.99%) are weighed according to the stoichiometry. Citric acid was added to this mixture as a chelating agent such that the citric acid and cation ratio is 1:3. The metal nitrates and citric acid were mixed in 1 L beaker in de-ionized water medium at 70 ºC with continuous stirring. The temperature was slowly raised and kept at 200 ºC until the combustion took place. The powder was kept in the same condition for one day to provide enough time for combustion. The precursor powder was ground well and loaded into a muffle furnace at 600 ºC for two hours and 900 ºC for six hours with intermediate grinding. The powders were ground well and pelletized using a hydraulic press. For pelletization, polyvinyl alcohol is used as a binder. The pellets were finally sintered at high temperatures with different duration. A picture of the main steps involved is given in figure 2.1.

2.2 Characterization Techniques

2.2.1 Powder X–ray diffraction

The phase identification of a crystalline material is made by using the powder X-ray diffraction (XRD). XRD is a quick non–destructive analytical technique used for phase identification and can provide information about the crystallographic structure and unit cell. The crystalline material is similar to the three-dimensional diffraction gratings for X-rays that are having wavelengths comparable to the interplanar spacing in the crystal lattice [7]. Hull reported that every crystalline material contributes a particular XRD pattern always, and in a mixture of crystalline substances each gives its XRD pattern independent of the others [8]. So, the powder XRD technique is the best method for identification and confirmation of phase of polycrystalline materials.

When an x-ray beam strikes a material, the electrons around the atoms in the materials will oscillate with the frequency of the incoming beam, just like an electron in an alternating electromagnetic field. In almost all the directions, the waves will combine out of phase leading to destructive interference and no resultant energy will be leaving the material. Since the atoms in a crystal are arranged in a regular pattern, the waves will combine in phase in few directions and lead to constructive interference for that particular orientations. There will be well-defined x-ray beams leaving the material in various orientations. So, the diffracted beam coming out of the sample is consisting of a large number of scattered rays mutually supporting one another.

Considering an X-ray beam incident on parallel planes P1 and P2, with interplanar spacing d, and they make an angle θ with the planes, as shown in figure 2.2 (a). The incident rays 1 and 2 will get reflected as 1' and 2'. The reflected beam with maximum intensity results when 1' and 2' are in phase. Then the difference in path length between 1 to 1' and 2 to 2' should be an integral number of wavelengths (λ). This condition is expressed mathematically as Bragg's Law: nλ=2d sin θ, where n is an integer.

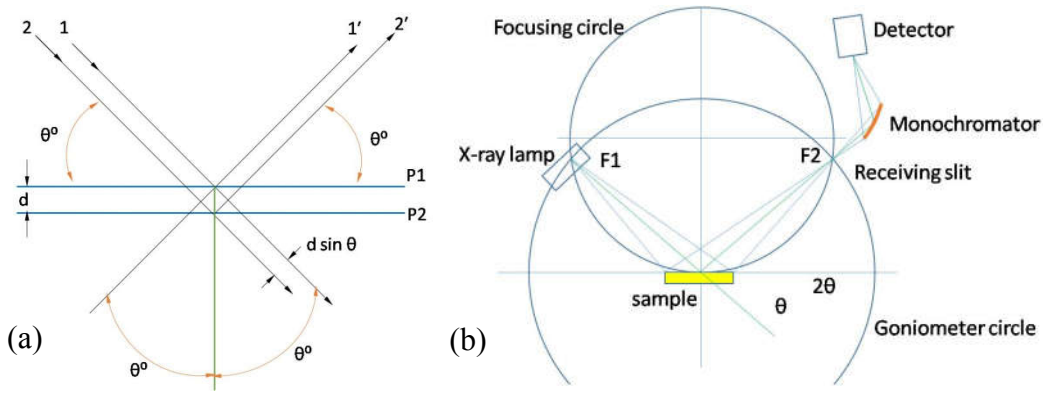

Figure 2.2 (a) Diffraction of incident X-Rays by parallel planes. (b) Schematic representation of powder X–ray Diffractometer.

The X-rays are produced by a cathode ray tube, which is filtered to generate a monochromatic beam of radiation, collimated to concentrate, and directed towards the sample. In polycrystalline powder, small crystallites of all possible orientations are assumed to be present. The incoming X-ray beam interacts with the crystallographic planes, and the diffraction occurs when the X–rays enter a crystalline substance which is then scattered. Then these diffracted X-rays are detected, processed and counted for a range of 2θ angles. The random orientation of the powdered material gives all the possible diffraction directions of the crystal lattice. The interaction of X-rays with crystalline substance produces diffraction

patterns corresponding to the Bragg angle. The plot of 2θ vs. intensity gives the intensities of the diffracted beam as peaks at particular 2θ. The schematic representation of a typical powder XRD recording machine is shown in figure 2.2 (b).

Even though the Bragg's condition is satisfied, the diffracted rays from certain planes won't appear in the XRD pattern. This is because of the destructive interference of X–rays scattered by different atoms present in the unit cell, causing the intensity to become zero. So the unit cell determines the XRD line position and the atom position, and a scattering factor determines the line intensities. Intensities of diffracted lines (I), ignoring the temperature and absorption factors, are related to structure factor (F) as: $I = |F|^2 \, p\left(\frac{1+\cos^2 2\theta}{\sin^2\theta \, \cos\theta}\right)$, where θ is the Bragg angle, p is the multiplicity factor. The ratio between the amplitude of the waves scattered by means of all atoms within the unit cell to the amplitude of the waves scattered through one electron is referred to as the structure factor. A simultaneous occurrence of non-zero structure factor and Bragg condition is necessary for a diffracted line to occur. The position, shape and relative intensity of a peak are correlated to crystallographic spacing, phase, and grain or particle size. Each crystal structure has a unique set of d-spacings. Thus the conversion of the diffraction peaks to d-spacings leads to the identification of crystal structure and confirmation of the phase of the substance. Usually, it is done by a comparison of d-spacings with standard reference patterns.

The XRD instrument used for identifying the phase purity of the materials of the present research work is PANalyticalX'Pert Pro X-ray Diffractometer powered by a Philips PW3040/60 standard resolution goniometer. The goniometer contains

the basic axes in X-ray diffractometry: the θ-axis and the 2θ-axis. The X-ray tube/generator, the incident beam optics, the sample stage, and the diffracted beam optics including the detector, are mounted on specific positions on the goniometer. X-rays were generated from a Cu anode supplied (generally) with a voltage of 40 kV and a current of 30 mA. The X'Celerator detector produces high-quality diffraction data in a significantly shorter period. The goniometer is positioned vertically so that the system has Bragg–Brentano θ–θ geometry. In this geometry, the sample stage does not rotate around the Θ-axis as in Bragg–Brentano θ–2θ diffractometers whereas it is fixed to the goniometer. The tube and the detector are moving in this case. The X-ray tube is fitted onto a movable goniometer arm with a fully automated operation and data collection. The finely powdered samples are filled in standard holders. The powder samples are exposed to the X-ray radiation (Cu-Kα, with λ=1.5418 Å). The data were collected (usually) over a range of 10-90º 2θ with a step size of 0.017º 2θ and nominal time per step of 15 s, using the scanning X'Celerator detector. Fixed anti-scatter and divergence slits were used together with a beam mask of 10 mm. All the scans were carried out in 'continuous' mode. The samples are finely powdered so that it will provide (theoretically) all permissible orientations of the crystal structure. The resulting XRD pattern is a set of peaks with intensity on the Y–axis and goniometer angle on the X–axis.

2.2.2 Rietveld refinement of the powder XRD pattern

Hugo Rietveld implemented the technique called Rietveld refinement in 1967 for extracting the crystallographic information from powder XRD and neutron diffraction data [9]. The Rietveld method is used to refine user-selected parameters to minimize the difference between an experimental pattern (observed data) and

calculated pattern modeled based on the hypothesized crystal structure and instrumental parameters [10]. The lattice parameters and space group are used to constrain peak positions, and the crystal structure is used to constrain peak intensities. The full profile is adjusted by the least-squares method to give the best fit.

The rectified intensity values are inferred by subtracting background corrections B_i from the observed intensity values at each element on the diffraction profile for which the contribution from any Bragg reflection is noteworthy [11]. For each Brag reflection, a Gaussian peak or pseudo–Voigt function is assumed initially, which allows a good modification to the Gaussian and Lorentzian peak shape.

For creating a structural model, an iterative procedure by the least squares method is employed in which some initial parameters like lattice constants, space group, atomic positions, atom types, etc., are used. By these initial parameters, a calculated XRD pattern is generated, which is then compared with experimentally observed XRD pattern. The intensity values are calculated (y^{cal}) by summing the contributions of all the Bragg reflections and background from the incident intensity (I_0), the scale factor for the particular phase (k_h) and the structure factor (F_h), the reflection multiplicity (m_h), and the correction factors (L_h) and background contribution (I_b) as $y^{cal} = I_0\left[\sum k_h F_h^2 m_h L_h P\left(\Delta_h\right) + I_b\right]$, where $P(\Delta_h)$ is the peak shape function. Instrument related factors such as the instrumental profile function, zero correction, background, wavelength, sample holder and sample related features like temperature factors, atomic coordinates, lattice parameters, occupancies,

crystallite size, absorption, etc. are also considered while calculating the intensity [11, 12].

The Rietveld refinement is done on each factor to minimize the difference between the observed pattern and the calculated pattern. The function M is minimized during the Rietveld method, which analyzes a calculated profile y^{cal} and the observed data y^{obs}. The function M is defined as the weighed divergence between the calculated and observed diffraction pattern. i.e. $M = \sum w_i \left(y_i^{obs} - y_i^{cal} \right)^2$ provided w_i are the corresponding weight, y_i^{obs} are the observed intensity at angular step i and y_i^{cal} are the corresponding calculated intensity.

The quality of the Rietveld refinement is measured with some quality factors such as profile factor (R_P), weighed profile factor ($_WR_P$), expectation factor R_{exp} [12]. They are described as follows: $R_P = \frac{\sum \left| y_i^{obs} - y_i^{cal} \right|}{\sum y_i^{obs}}$, $_WR_P = \left(\frac{\sum w_i (y_i^{obs} - y_i^{cal})^2}{\sum_i w_i y_i^{obs2}} \right)^{\frac{1}{2}}$, and $R_{exp} = \left(\frac{N - P + C}{\sum_i w_i y_i^{obs2}} \right)^{\frac{1}{2}}$ where N is the number of points in the pattern, P is a measure of refined parameters and C is the number of strict constraint functions [13]. (N-P+C) gives the number of degrees of freedom.

Further, the Bragg factor, $R_{Bragg} = \left(\frac{\sum \left| I_i^{obs} - I_i^{cal} \right|}{\sum I_i^{obs}} \right)$ where, I_i^{obs} and I_i^{cal} are the observed and calculated integrated intensities for the different Bragg peak, i. The

measure of the goodness of fit (χ^2) can be found out from the residual factors $_WR_P$ and R_P as $\chi^2 = \left(\frac{R_{wp}}{R_p} \right)^2$.

In this work, the Rietveld structural refinement of the powder XRD pattern is done by using the GSAS software (General Structure Analysis System) with EXPGUI (graphical user interface) platform [14]. The shifted Chebyshev polynomial is used to refine the background, with a number of variables ranging from 10-25. A pseudo–Voigt function is selected to refine the shape of the peak.

The parameters are refined as per the order: the scale factor, the zero correction for 2θ, background function, the cell parameters, the peak shape (profile) parameters, the coordinates, the isotropic displacement parameters and the thermal factors. After obtaining a good fit, the crystallographic information obtained is analyzed. This information is used as an input to the CrystalMaker® software to frame the crystal structure of the material.

2.2.3 Scanning Electron Microscopy

Scanning Electron Microscopy (SEM) is a microscope technique that provides the images of the material by scanning by means of electron beam focused on the surface of the material. SEM produces an electronic map of the specimen with resolution better than 1 nm. The surface of the material is scanned by focusing the electron beam into a small spot on the material to produce a two-dimensional image. The interactions of the electrons with the surface atoms of the material provide signals having information about the sample's surface topography and composition. The generated signals incorporate the secondary electrons (SE),

reflected or back-scattered electrons (BSE), photons of characteristic X-rays and light (cathodoluminescence) (CL), absorbed specimen current and transmitted electrons, resulted from the associations of the electron beam with atoms at different profundities inside the sample [15]. The secondary electrons are emitted from near the specimen surface. Thus the SEM secondary electron (SE) image mode would produce very high-resolution images of a sample surface, with a better resolution of less than 1 nm. The back-scattered electrons (BSE) are those reflected from the sample by elastic scattering. They are coming from the deeper sites of the material. The escape depth of BSE is greater than that of the SE resulting in a week resolution of surface topographical characteristics. Nevertheless, the BSE is sensitive to the atomic mass of the nuclei they scatter from, and consequently, the BSE image can provide information about the elements present in the material. Heavier elements that backscatter more effectively appear brighter than lighter elements in a BSE image.

SEM images have a large depth of field due to the extremely narrow beam of the electron. This gives a characteristic three-dimensional appearance to the two-dimensional image that is useful for understanding the surface morphology of material.

Non-conducting specimens may get charged when kept under an electron beam (especially in SE image mode) and cause scanning faults and other image artifacts. To avoid the accumulation of electrostatic charge, the insulating samples must be coated with an electrically conductive material and should be electrically grounded. In the present study, the entire specimens are coated with gold. Surface microstructures of the prepared samples are analyzed from the SE image taken by

using JEOL JSM-5610 Scanning Electron Microscope. A schematic representation of SEM microscope is shown in figure 2.3.

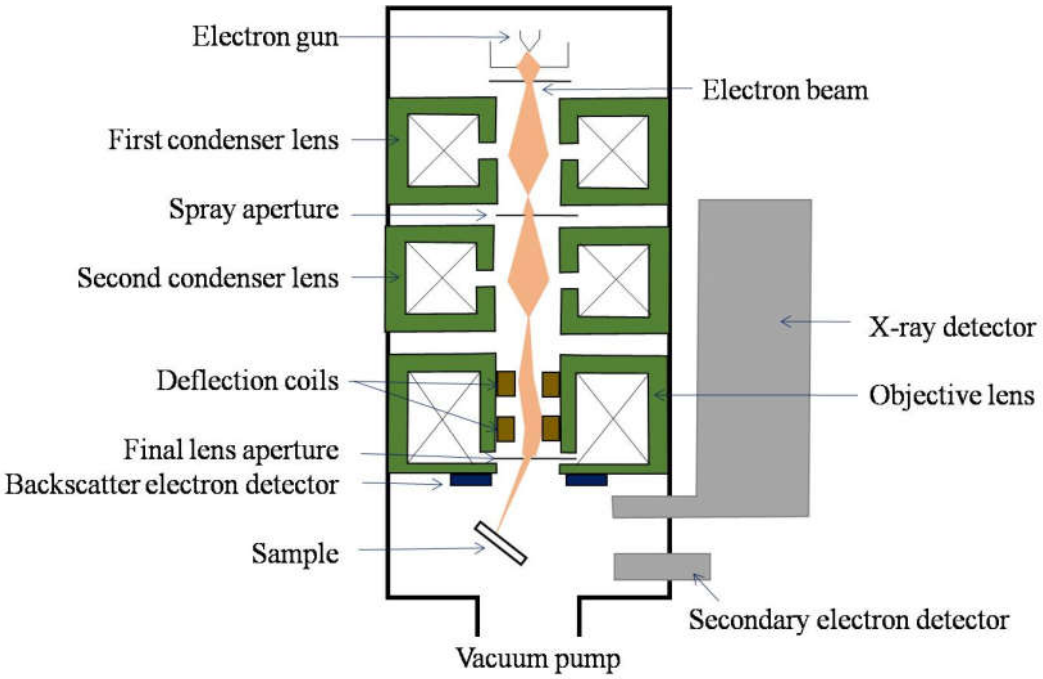

Figure 2.3 Schematic representation of a SEM microscope

2.2.4 X-Ray Photoelectron Spectroscopy

A surface-sensitive quantitative spectroscopic method called X-ray photoelectron spectroscopy (XPS) is used to determine the elemental composition of the surface, stoichiometric formula of pure materials, contaminated constituent elements on the surface, chemical state or electronic state of each element in the surface, uniformity of elemental composition across the surface, regularity of elemental composition, etc. [16]. The XPS spectra are obtained by irradiating a material with a beam of X-rays and concurrently evaluating the kinetic energy and quantity of electrons that escape from the top 0 to 10 nm of the specimen. The photoelectrons, emitted from the surface of the sample, on irradiating with mono-

energetic Al kα x-rays, are analyzed during an XPS measurement. An electron energy analyzer measures the energy of the emitted photoelectrons. From this, the BE is calculated. From the BE and the corresponding intensity of the peak of photoelectron, the chemical state, identity of elements, and quantity of a detected element can be optimized. XPS and SEM/EDS instruments are analogous to each other somewhat on their function such that SEM/EDS employ a finely focused electron beam to create SEM images and point spectra or images for compositional analysis. The XPS instruments employ a focused x-ray beam to create secondary electron images for viewing the sample and generate point spectra or images for compositional examination.

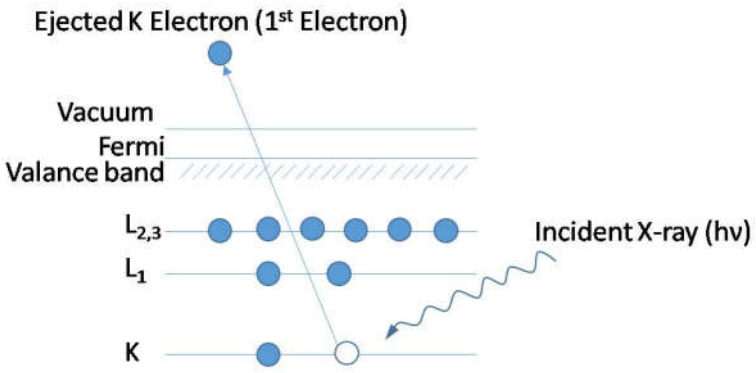

Figure 2.4. The photoemission process involved for XPS surface analysis.

XPS is based upon the interactions between electrons and X-rays. An incident X-ray photon collides with a core electron and the collision causes the electron to be ejected from the electronic shell is the main process (Compton scattering) taking place in an XPS measurement. A solid material irradiated with X-rays can emit electrons like photoelectrons from the valence and core energy levels, Auger electrons, and secondary electrons. If we are irradiating an X-ray of known energy, the binding energy of the emitted electrons can be calculated from the

measured kinetic energy of the emitted electrons [17] as $E_{binding} = E_{photon} - (E_{kinetic} + \phi)$, where $E_{binding}$ gives the binding energy (BE) of the electron, E_{photon} corresponds to the energy of the X-ray photons, $E_{kinetic}$ corresponds to the measured kinetic energy of the electron, ϕ is the work function dependent on both the instrument and the material. The BE depends on various factors like the element that emitted the electron, the orbital from where the electron is ejected, the chemical environment of the atom, etc. The photoemission process involved in XPS is depicted in figure 2.4.

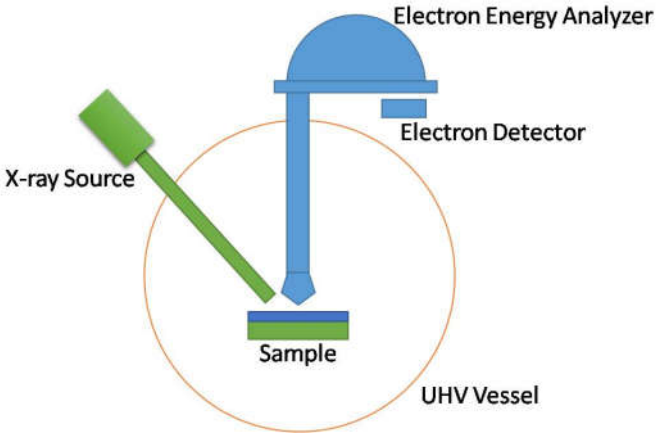

Figure 2.5. Schematic diagram of main instrumental components in XPS.

A schematic diagram of main instrumental components in XPS is shown in figure 2.5. The Fermi level of both the spectrometer and the sample surface is equivalent to the case of a conducting sample, and the above equation follows exactly in such situations. A conducting sample won't build up charges since the sample is grounded in the system. While the Fermi levels are not equivalent for an insulating sample and spectrometer. Charges accumulate on the surface of the sample and cause the Fermi level of the spectrometer to shift to a higher energy. This may cause a small shift in the measured electron kinetic energy. To correct the

shift in energy, the data is calibrated during the measurement by using C1s as reference energy [18].

In the present study, an Omicron Nanotechnology Multiprobe Instrument and a Thermo Scientific X-ray photoelectron spectrometer are used for measuring the photoelectron counts as a function of binding energy. The observed spectra are fitted by using the XPSPEAK4.1 peak fitting software after the correction in BE with that of the reference C1s.

2.2.5 Vibrating sample magnetometer

Vibrating sample magnetometer (VSM) is a measurement set up that measure the magnetic moment of a sample material with very high accuracy, based on the Faraday's law of electromagnetic induction. The Faraday's law states that an emf is induced in a conductor placed in a varying magnetic field and the induced emf is equal to the rate of change of the flux associated with it. On measuring the induced emf, one can get information about the changing magnetic field. A VSM measures the magnetic moment of a sample when it is vibrated perpendicularly to a uniform magnetizing field [19, 20].

The sample whose magnetic moment is to be measured is placed in a constant magnetic field. The magnetic field will magnetize the material (if the material is magnetic) by aligning the magnetic domains or individual magnetic spins along the field. This magnetic dipole moment of the material would generate a magnetic field around the sample (stray magnetic field). When the sample is vibrated up and down, this stray magnetic field will vary as a function of time, which can be detected by a set of pick-up coils. This changing magnetic field will

induce an emf in the pick-up coils according to the Faraday's law, which is directly proportional to the magnetic moment of the sample. This induced emf is amplified by a lock-in amplifier, which is then controlled and monitored by a software program and the corresponding magnetic moment is calculated.

The present work used the VSM attached to the Quantum Design DynaCool Physical Property Measurement System (PPMS) for DC magnetic moment measurements with a magnetic field in the range 0- ± 90 kOe and temperature in the range 2-400 (K) in standard mode and 300-1000 K in oven mode. This PPMS system has a single two-stage pulse tube cooler for cooling both the temperature control system and the superconducting magnet, providing a vibration-free environment for measurements, and without the requirement of a liquid cryogen [21].

The PPMS DynaCool has five main components, viz. Cryostat assembly, CAN module bay, pump cabinet and computer, Cryocooler compressor assembly, helium gas cylinder, and regulator. The cryostat assembly has the cryogenic components of the system, including the superconducting magnet, sample chamber, and pulse-tube assembly for the Cryocooler, gas handling valves and electronics. Fiberglass housing covers the exterior surface of the cryostat. Both the cryostat cover and the fiberglass side panels are attached to a steel magnet shield.

The VSM attached to the PPMS consists of a VSM linear motor transport (head) for vibrating the sample, a coil set detection puck, electronics for driving the linear motor transport and sensing the pickup coils response, and a MultiVu software for automation and control [21]. A schematic representation of VSM is shown in figure 2.6.

The dime-dependent induced voltage is given by $V_{coil}=d\Phi/dt=(d\Phi/dz)(dz/dt)$, where Φ is the magnetic flux enclosed by the pick-up coil, z is the vertical position of the sample with respect to the coil, and t is the time. For a sinusoidally oscillating sample position, the voltage is given by the equation $V_{coil}=2\pi fCmAsin(2\pi ft)$, where C is a coupling constant, m is the DC magnetic moment of the sample, A is the amplitude of oscillation, and f is the frequency of oscillation. On measuring the coefficient of the sinusoidal voltage response from the detection coil, the magnetic moment is acquired.

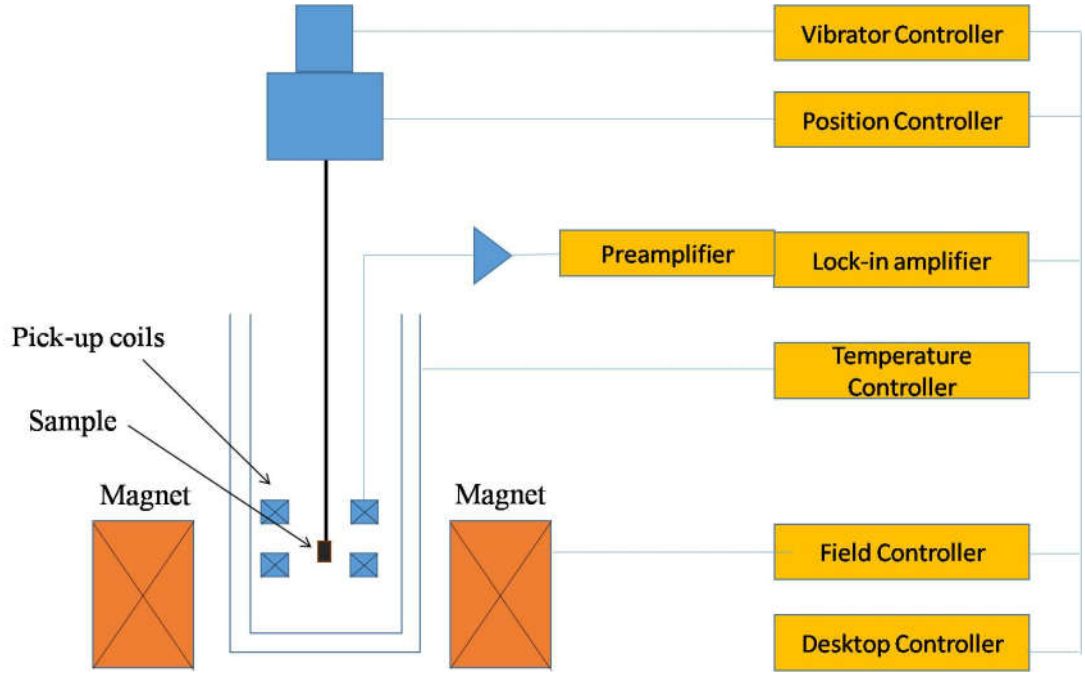

Figure 2.6. Schematic representation of VSM

2.2.6 AC magnetic characterization

The dynamic behaviour of the magnetic structure of the material can be identified from the AC magnetic measurements. Mostly, it is used to identify spin glass systems. In AC magnetic measurements, a small AC drive magnetic field is superimposed on the external DC field. A time-varying magnetization is developed

in the sample, which induces an emf (proportional to the magnetization) in the pickup coil, allowing measurements without sample motion.

For very low frequencies the magnetic moment of the sample follows the M(H) curve that would be measured in a DC experiment. For small AC field, the induced AC moment can be written in terms of the amplitude of the driving field (H_{AC}), the driving frequency (ω), and the slope of the M(H) curve ($\chi=\partial M/\partial H$, the susceptibility) as $M_{AC}= (\partial M/\partial H) H_{AC} \sin(\omega t)$. Different parts of the M(H) curve can be accessed by changing the applied DC magnetic field, giving a different χ. Small magnetic shifts can be detected in this technique even when the absolute moment is large since the AC measurement is responsive to the slope of M(H) and independent of the absolute value [22].

The AC moment of the sample may not match the DC M(H) at high frequencies due to the dynamic effects in the sample. The magnetization of the sample may lag behind the drive field in such cases. Thus the AC magnetic susceptibility has a magnitude of the susceptibility, χ, and a phase shift, φ (relative to the drive signal). So, the complex χ can be split into real (χ') and imaginary (χ'') as $\chi' = \chi \cos \varphi$, and $\chi'' = \chi \sin \varphi$, provided the $\chi= (\chi'^2+ \chi''^2)^{1/2}$, $\varphi= \tan^{-1}(\chi''/ \chi'')$. During the AC susceptibility measurement, the alternating magnetic field (generated by the primary of the coil set) is superimposed to the DC field of the PPMS superconducting magnet. This alternating field is created by the AC stimulus-response (ACSR) high-speed electronics' board and sent to a digital-to-analog converter [23]. The amplified analog signal is used to control the precise AC excitation currents sent to the drive and compensation coils.

2.2.7 Electron spin resonance (ESR) or electron paramagnetic resonance (EPR)

Materials with unpaired electrons are studied with electron paramagnetic resonance (EPR) or electron spin resonance (ESR) spectroscopy. Every electron has an intrinsic magnetic moment and spin quantum number s=1/2 with magnetic components m_s=+1/2 and m_s=-1/2. In the presence of an external magnetic field of strength B_0, electron's magnetic moment aligns itself either parallel (ms=-1/2) or antiparallel (ms=+1/2) to the field, with a particular energy, due to Zeeman Effect: $E = -m_s g\mu_B B_0$, where g≈2 for free electron, $\mu_B = eh/4\pi mc$ ($=9.27 \times 10^{-24}$ JT^{-1}) is the Bohr magneton. So, the separation between the lower and upper energy states will be directly proportional to the external magnetic field, as: $\Delta E = g\mu_B B_0$ for unpaired free electrons, as shown in figure 2.7.

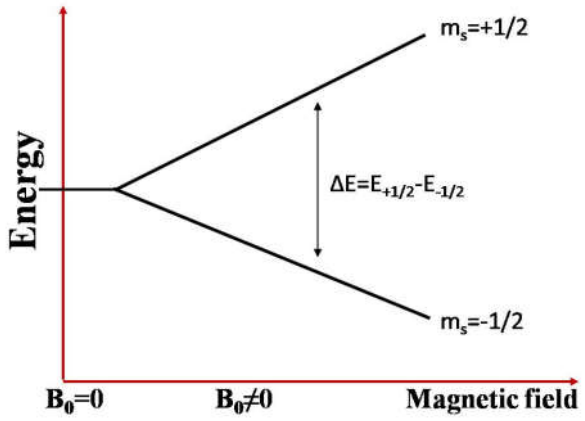

Figure 2.7. Splitting of electron spin states on an application of magnetic field.

An unpaired electron can move between the two energy states by absorbing or emitting a photon of energy hυ= ΔE (resonance condition). The basic principle behind the ESR spectroscopy is the equation $h\upsilon = g\mu_B B_0$. During the ESR measurements, the field of the spectrometer magnet is varied to excite electrons in

the lower energy level to the upper energy level at the same time the sample is exposed to a fixed microwave irradiation of frequency υ. At a particular magnetic field strength, a resonance condition is attained where the microwave irradiation flip some of the free electrons and orients against the spectrometer's magnetic field. This resonance condition is detected by the spectrometer. In the present work, the ESR spectra obtained using JES-FA200 ESR Spectrometer (ESR-JEOL, Japan) for confirming the presence of paramagnetic and ferromagnetic contribution at room temperature.

2.2.8. Electrical resistivity and magnetoresistance

The resistivity (ρ) of a material is a measure of the resistance offered by the material to the flow of current through, which always depends on its nature. The resistivity of a material is constant at a given temperature. It can be found from the resistance (R) and the dimension of the sample (length (l), the area of the cross-section (A)) as ρ=R A/l. When a current of known value (I) is supplied to a sample, on measuring the developed potential difference (V), the R can be obtained as R=V/I.

The main methods for resistivity measurements are two-probe and four-probe methods. In the two-probe method, the voltmeter and current source are connected to the same pair of leads. In the four-probe method, four probes of equal separation are in contact with a material as shown in figure 2.8 (a) The current is fed through the probes 1 and 4 while the voltage drop across the surface of the sample is measured across the probes 2 and 3. Figure 2.8 (b) shows the electric field lines through the material as solid curves and the equipotential lines as broken curves.

The inner probes do not draw any currents due to the presence of high impedance voltmeter in the circuit and the unwanted voltage drop (IR) at points B and C due to contact resistance between sample and probe would be eliminated. For measuring the magnetoresistance (MR) of the material, the resistivity measurement is performed in the presence of an external magnetic field. MR (%) is calculated by the equation MR (%)=$(\rho_H-\rho_0)/\rho_0$ x 100 % where ρ_H is the resistivity in the field and ρ_0 is the resistivity at zero applied field.

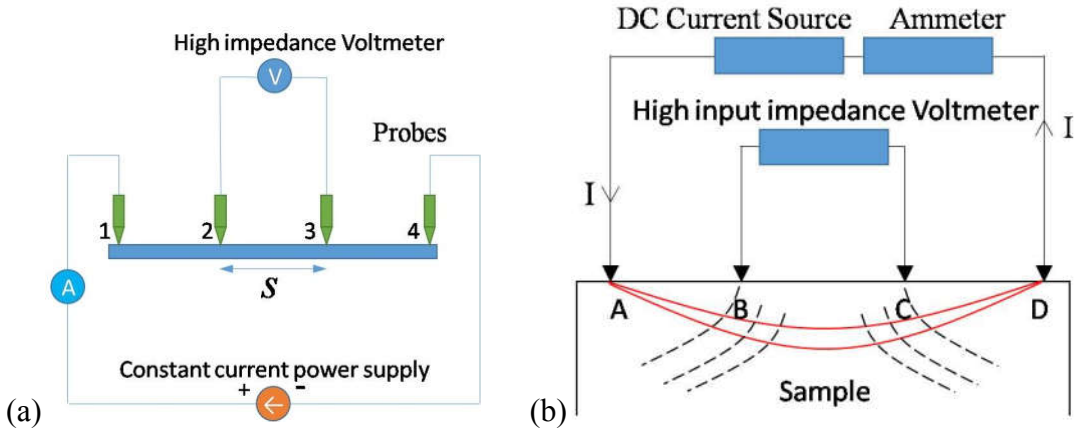

Figure 2.8 (a) Four-probe method of measuring resistivity. (b) Electrical field lines and equipotential lines in a material during the four-probe method.

In the present work, the resistivity and magnetoresistance of the materials are found by using the electrical transport option (ETO) attached to the PPMS DynaCool. ETO has two separate channels; each allows simultaneous and continuous resistance measurement of two different samples. Each channel has a precision current source and voltage preamplifiers, coupled to a Digital Signal Processor (DSP). A sinusoidal AC drive current is applied to the sample, and the corresponding AC voltage is recorded during the measurement [24].

2.2.9. Specific heat capacity measurements

The specific heat is the amount of heat per unit mass required to increase the temperature of a substance by one degree Celsius or Kelvin. Information regarding lattice, electronic, and magnetic properties, etc. can be fetched by measuring the heat capacity. By fitting the specific heat data with theoretical equations at the low-temperature region, the electronic and lattice contributions to the heat capacity could be calculated. In our present study, the specific heat capacity (C) is measured by using the Quantum Design Heat Capacity option attached to the PPMS DynaCool. It measures C at constant pressure, $C_P = (dQ/dT)_P$. It controls the heat added to and removed from a sample while monitoring the resulting change in temperature [25]. A particular amount of heat is applied at constant pressure for a fixed time. This heating period is followed by a cooling period of the same duration. At the bottom of the sample platform, a platform heater and a platform thermometer are connected. A thin layer of grease is used to mount the sample on the platform. A schematic diagram of the sample and sample platform connections in PPMS heat capacity option is shown in figure 2.9.

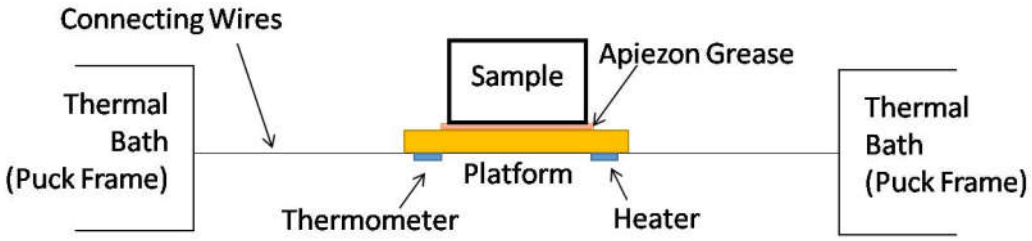

Figure 2.9. Thermal connections to sample and sample platforms in PPMS heat capacity option.

2.2.10. Dielectric and Magnetodielectric measurement

The ability of an insulator material to store electrical energy is determined by measuring the dielectric constant (ε), which is defined as the ratio of the permittivity of the material to that of free space. It gives the interaction of a material with an electric field. The complex **ε** can be split into the real part (ε'), which represents the storage capability and imaginary part (ε''), which represents the energy loss from the material arising from an external electric field. Loss tangent or dissipation factor is defined as the tangent of the ratio of ε'' and ε' (tan δ=ε'''/ε').

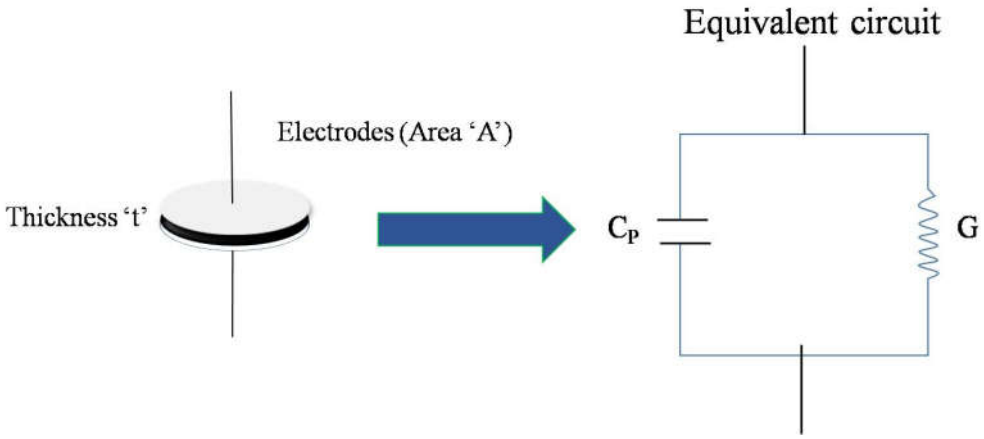

Figure 2.10. Parallel plate capacitor method

The dielectric properties of the samples in the present work are measured by using an LCR meter (Agilent E4980A), compensated for the coaxial cable length with open and short circuit calibrated. The sample in the form of a cylindrical pellet with thickness t~2 mm and diameter ~10 mm are connected to the LCR meter as a parallel plate capacitor. A silver coating is pasted on both the surfaces of the pellets by diluting it with isoamyl acetate. The silver coating on both the surfaces acts as the parallel plates, as shown in the figure 2.10. The parallel plate capacitor structure is

inserted into a cold head of a closed cycle Cryocooler (ARS-2HV). The actual voltage across the material is checked while the material is exposed to an AC source. The capacitance and the loss tangent are directly obtained from the LCR meter by the auto-balancing bridge technique [26]. The capacitance (C) is used to calculate the ε as $\varepsilon=Cd/(A\varepsilon_0)$, where d is the thickness of the material, A is the surface area of the parallel plate, ε_0 is the ε of free space. The dielectric constant measurement is repeated by placing a hollow cylindrical Neo magnet above the parallel-plate sample set-up, and the ε and tan δ with the field (ε_H and tan δ_H) are calculated. The magnetodielectric (MD) coupling and MD loss (MDL) coupling are calculated from these data by using the equations MD (%) = $(\varepsilon_H-\varepsilon_0)/\varepsilon_0$x 100 % and MDL (%) = (tan δ_H-tan δ_0)/tan δ_0 x 100 %.

2.3 References

[1] L.L.H. George Y. Onoda, Ceramic Processing before Firing, Wiley & Sons, New York, 1979.

[2] M.R.M.N. Rahaman, Ceramic Processing, CRC Press, 2006.

[3] S.O. Nelson, A.W. Kraszewski, Drying Technology, 8 (1990) 1123-1142.

[4] J. Gopalakrishnan, S. Uma, K.K. Rangan, N.S.P. Bhuvanesh, Proceedings of the Indian Academy of Sciences - Chemical Sciences, 106 (1994) 609-619.

[5] R. Casasola, J.M. Rincón, M. Romero, Journal of Materials Science, 47 (2012) 553-582.

[6] Y. Wu, Z. Yu, S. Liu, Journal of Solid State Chemistry, 112 (1994) 157-160.

[7] M. Eckert, Annalen der Physik, 524 (2012) A83-A85.

[8] A.W. Hull, Journal of the American Chemical Society, 41 (1919) 1168-1175.

[9] A. Hewat, W.I.F. David, L. van Eijck, Journal of Applied Crystallography, 49 (2016) 1394-1395.

[10] H. Rietveld, Journal of Applied Crystallography, 2 (1969) 65-71.

[11] M. Sakata, M.J. Cooper, Journal of Applied Crystallography, 12 (1979) 554-563.

[12] D. Cox, Journal of Applied Crystallography, 27 (1994) 440-441.

[13] Z. Chen, R.-J. Wang, J. Li, Chemistry of Materials, 12 (2000) 762-766.

[14] B. Toby, Journal of Applied Crystallography, 34 (2001) 210-213.

[15] F. Krumeich, ETH Zurich, Zurich.

[16] Wikipedia, the free encyclopedia, Wikipedia, the free encyclopedia.

[17] D. Briggs, Surface Analysis of Polymers by XPS and Static SIMS, 1998.

[18] J.F. Moulder, J. Chastain, Handbook of x-ray photoelectron spectroscopy : a reference book of standard spectra for identification and interpretation of XPS data, Physical Electronics, Eden Prairie Minnesota, 1995.

[19] S. Foner, Review of Scientific Instruments, 30 (1959) 548-557.

[20] L. Smith, R. Gluckstern, Instrmn, 27 (1956) 261.

[21] Part Number 1096-100, B0, 2011.

[22] D. Martien, QuantumDesign.

[23] Physical Property Measurement System AC Measurement System (ACMS II) Option User's Manual Quantum Design 2015.

[24] Electrical Transport Option (ETO) User's Manual, Quantum Design, 2015.

[25] Physical Property Measurement System® Heat Capacity Option User's Manual, Quantum Design, 2015.

[26] A. Technologies.

Chapter 3

High-temperature magnetic transition and existence of positive and negative magnetodielectric coupling in La_2FeMnO_6

This chapter has following sections:

1. *High-temperature magnetic transition and existence of ferromagnetic short-range correlations above transition in La_2FeMnO_6*
2. *Large positive and negative magnetodielectric coupling in La_2FeMnO_6*

Section 3-1

High-temperature magnetic transition and existence of ferromagnetic short-range correlations above transition in La_2FeMnO_6

This section deals with the observation of a high-temperature magnetic transition and existence of a Griffiths-like phase in disordered double perovskite La_2FeMnO_6.

3-1.1 Introduction

The perovskite oxides ABO_3 (A = alkaline or rare earth elements (R), B =transition elements) possess a vast variety of physical properties like ferromagnetism (FM), ferrimagnetism (FiM), half-metallicity, magnetoresistance, magnetodielectric (MD) coupling, etc. [1-10]. The manganite perovskites ($AMnO_3$) have received considerable attention due to their magnetic, transport and magnetotransport properties linked with the change in the spin state [11, 12]. Introducing the second element to the B-site will provide further characteristics to the system [Double Perovskite (DP)] by the differences in cationic radius which in turn affects the ordering, oxidation states, antiphase boundaries, multiple exchange interactions, lattice distortion, etc. [1-4]. Enormous studies are being carried out in nowadays on rare earth (RE) manganites with DP structure that exhibit multifunctional properties by their broad B/Mn cationic range [7-10]. Among these compounds, La_2NiMnO_6 is quite attractive since it is a FM semiconductor with good magnetodielectric and magnetoresistance properties at temperatures close to room temperature due to its frustrated spin state originating from Ni and Mn cations [13, 14]. Among the RE manganites, La_2FeMnO_6, the Fe counterpart of La_2NiMnO_6, remains unexplored fully, to a large extent.

The perovskites $LaFeO_3$ and $LaMnO_3$ are antiferromagnetic (AFM) insulators in bulk form with Néel temperature (T_N) 740 K and 140 K respectively, in which the superexchange interactions Fe^{3+}-O-Fe^{3+} and Mn^{3+}-O-Mn^{3+} lead to AFM coupling [15-17]. There are reports pertaining to the preparation of La_2FeMnO_6 having perovskite structure [18, 19]. Many researchers continued the work on La_2FeMnO_6 both experimentally and theoretically, but an apparent magnetic

transition was not identified experimentally on bulk La_2FeMnO_6. This section presents the observation of a high-temperature magnetic transition and the evidence for the existence of ferromagnetic short-range correlations (FSCs) far above room temperature in La_2FeMnO_6.

3-1.2 Experimental Details

Polycrystalline La_2FeMnO_6 is synthesized by employing Pechini method [19]. High purity chemicals $La(NO_3)_3.6H_2O$, $Fe(NO_3)_3.9H_2O$ and $Mn(NO_3)_2$ (Sigma-Aldrich, purity ~99.99%) were weighed according to stoichiometry. Citric acid was added to this mixture such that the citric acid and cation ratio is 1:3. The nitrates and citric acid were mixed in 1 L beaker in de-ionized water medium at 70ºC with continuous stirring. The temperature was slowly raised, and finally, the combustion took place at 200ºC. The powder was kept at same condition for one day. The precursor powder was ground well and loaded into a muffle furnace at 600ºC for 2 hours and 900ºC for two hours. The powders were ground well and pelletized using a hydraulic press. For pelletization, polyvinyl alcohol was used as a binder. The pellets were finally sintered at 900 ºC for 6 hours. The sintered pellets were ground well, and the final material was confirmed as phase pure La_2FeMnO_6 by using the X-ray diffraction (XRD) data obtained by Philips PANalytical X'Pert Pro Powder X-Ray Diffractometer, having a Ni-filtered Cu Kα radiation (λ=1.5406 Å). The Rietveld refinement of the XRD pattern was done by using the software GSAS – EXPGUI [20]. The crystallographic structure is framed by using CrystalMaker® [21]. X-ray photoelectron spectroscopy (XPS) measurements were carried out by using an Omicron Nanotechnology Multiprobe Instrument. The peaks are fitted by using the XPS PeakFit software. The magnetization measurements were

carried out on La_2FeMnO_6 powders by using a Vibrating Sample Magnetometer (VSM) attached to a Physical Property Measurement System (Dynacool, Quantum Design). The specific heat (C) is measured for the temperature range of 10-150 K by using the heat capacity option attached to the PPMS (Dynacool, Quantum Design). The electron spin resonance (ESR) spectra are obtained by using JES - FA200 ESR Spectrometer (ESR-JEOL, Japan) at temperatures 100 K, 170 K, and 300 K.

3-1.3 Results and Discussion

3-1.3.1 Structural characterization

The orthorhombic, *Pbnm* crystal structure is confirmed for La_2FeMnO_6 by the Rietveld refinement using GSAS – EXPGUI [20] ($_WR_P$ = 4.09 %, R_P = 3.16 % and χ^2=1.12). The observed, calculated and difference data are shown in figure 3-1.1 (a). The obtained lattice parameters are, a= 5.5398(4) Å, b= 5.5141(1) Å, c= 7.8122(3) Å, and α, β, γ = 90° with <Fe-O-Mn> bond angle of 161.75°. The crystallographic structure framed using CrystalMaker® is shown in figure 3-1.1 (b).

The XPS spectra corresponding to Fe 2p and Mn 2p of La_2FeMnO_6 are analyzed. The binding energies were corrected by taking C 1s as reference energy (C 1s = 284.8 eV). The peaks are fitted by using the XPS PeakFit software. The fitted curves are shown in figure 3-1.1 (c) and figure 3-1.1 (d). The fitted curves give single peak for Fe $2p_{3/2}$ and Mn $2p_{3/2}$ with peak positions at 710.14 eV and 641.36 eV respectively, which confirms the oxidation states of cations as Fe^{3+} and Mn^{3+} [22, 23].

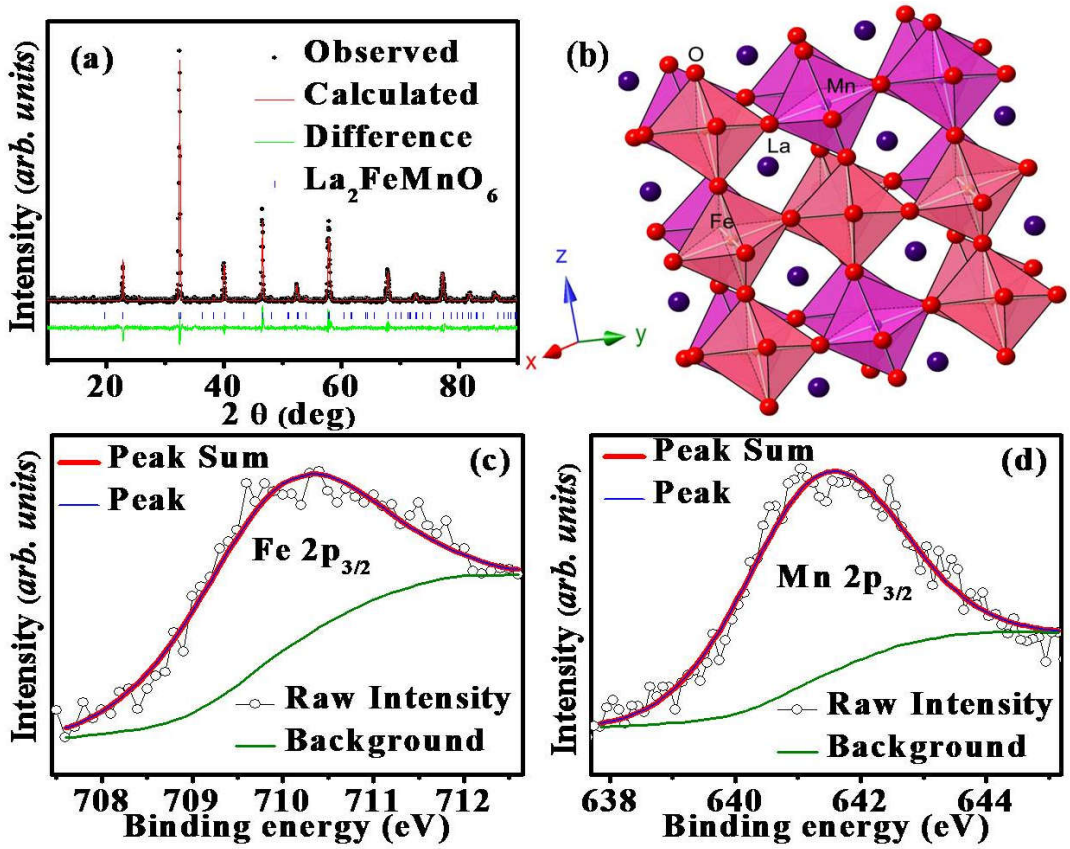

Figure 3-1.1 (a) Observed, calculated and the difference XRD pattern of La_2FeMnO_6 obtained from Rietveld refinement. (b) A small portion of the crystallographic structure of La_2FeMnO_6 crystal framed using CrystalMaker®. XPS spectra of (c) Fe $2p_{3/2}$ and (d) Mn $2p_{3/2}$ in La_2FeMnO_6 along with the fitted curves.

3-1.3.2 Magnetic characterization

Based on the reported density-functional calculations, La_2FeMnO_6 could be either a FM semiconductor or a FM half-metal or a FM metal or a FiM semiconductor under different biaxial strain conditions [24]. Also, de Lima *et al.* reported the magnetic properties of La_2FeMnO_6 bulk with T_C=65 K and coercivity (H_C) of 1160 Oe at 2 K and 170 Oe at 300 K [25]. Further, a hysteresis loop with small H_C and remanence (M_r) at 300 K was also reported for La_2FeMnO_6 [26]. In

the present study, zero field cooled (ZFC), and field cooled (FC) magnetizations were measured in the temperature range 5-385 K using the cryostat (Inset of figure 3-1.2) and in the range 300-950 K by using the oven (figure 3-1.2) in applied fields of 50, 200 and 1000 Oe. The temperature dependent magnetization (M-T) show irreversibility in magnetization as can be evidenced in the ZFC and FC bifurcation at lower temperatures and lower applied fields, which points towards the presence of spin frustration or spin glass state at low temperatures as per the previous reports on La_2FeMnO_6 [27-29]. The derivative dM/dT vs. T plot (figure 3-1.3 (a)) indicates a broad transition at T_{C1}=60 K, which corroborates the spin glass-like transition reported earlier [25, 27-29].

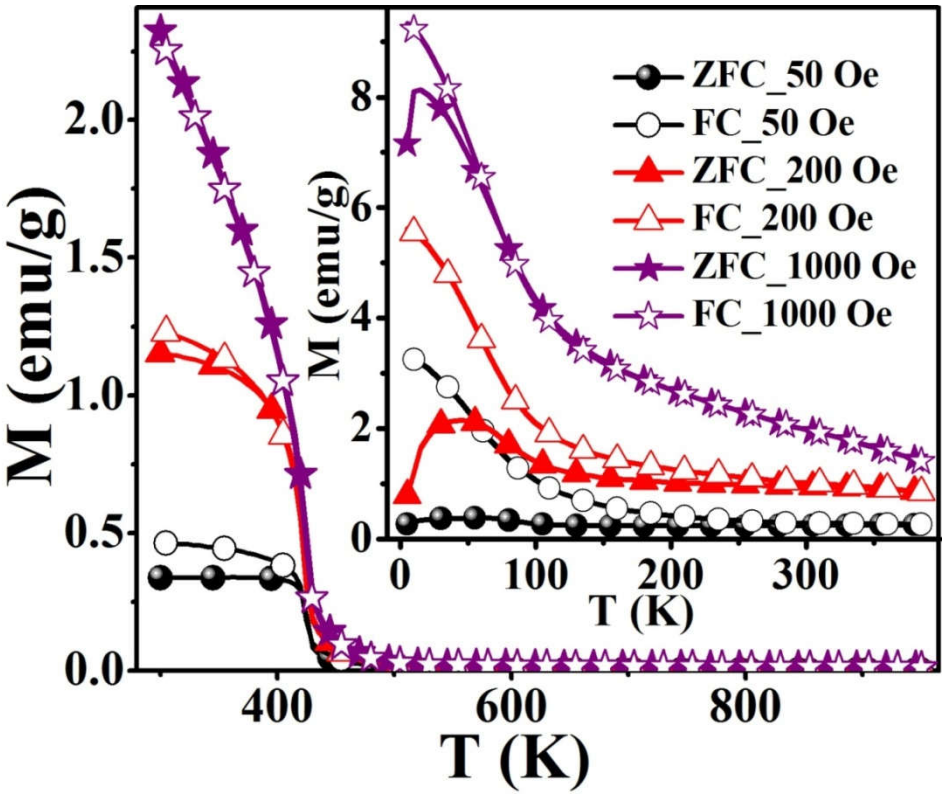

Figure 3-1.2 ZFC and FC curves at 50, 200, and 1000 Oe for 5-380 K. Inset showing ZFC and FC curves at 50, 200, and 1000 Oe for 300-950 K

Bhame *et al.* observed a positive value of Curie-Weiss constant (Θ) as an indication of the presence of ferromagnetic exchange interactions and H_C of 1170 Oe at 12 K for La_2FeMnO_6 [30]. The M-T in the range 5-300 K is similar to that observed in previous cases, and a closer look at the plot shows that the moment does not go to zero even at room temperature [30, 31]. Further, the room temperature hysteresis loop is also reported for La_2FeMnO_6 [25, 26]. Ueda *et al.* observed no transition in the M-T in the range of 50-400 K and predicted that there might be an AFM transition above 400 K [32]. They have also fabricated thin films of La_2FeMnO_6, by artificially creating superlattices and by natural growth and showed an FM to paramagnetic (PM) transition (T_C) at ~230 K and ~380 K respectively [32, 33].

This instigated us to carry out higher temperature (300-950 K) M-T measurements (figure 3-1.2), which showed a transition at T_C~425 K as shown in dM/dT vs. T plot (figure 3-1.3 (b)). This evidence of the onset of a magnetic transition above room temperature is in line with the theoretical predictions and experimental observations in La_2FeMnO_6 thin films [34, 35]. The disordered cation arrangements generate antisite boundaries leading to competing exchange interactions viz. Fe^{3+}-O-Mn^{3+} FiM interactions, Fe^{3+}-O-Fe^{3+}, and Mn^{3+}–O–Mn^{3+} AFM interactions and Mn^{3+}–O–Mn^{3+} dynamic FM interactions [17, 26]. Further, there is a key role played by the <B-O-B'> bond angle in determining the exchange interaction strength with a maximum at 180°. The superexchange interaction is rather favored in this case since the <Fe-O-Mn> bond angle is as high as 161.75°.

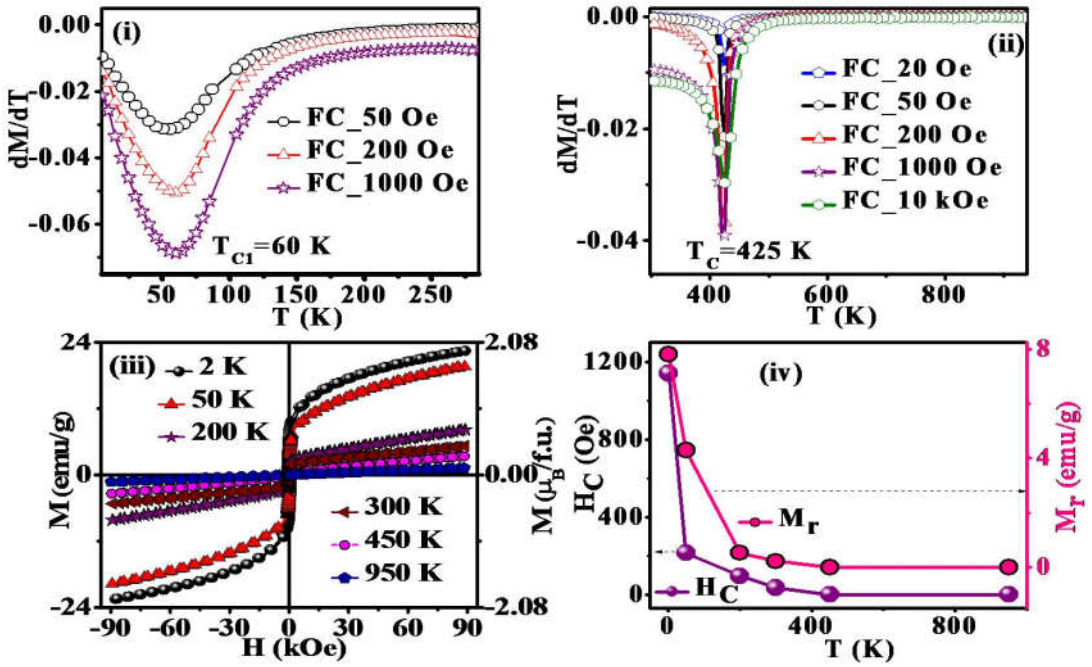

Figure 3-1.3 Derivative of magnetization (FC) with respect to temperature vs. temperature for (a) 5-300 K and (b) 300-950 K. (c) M-H curves recorded at different temperatures. (d) Variation of coercivity (H_C) and remanence (M_r) with temperature.

Field dependent isothermal magnetization (M-H) was measured in the field range of -90 kOe to +90 kOe at different temperatures ranging from 2 to 950 K, and representative results are summarized in figure 3-1.3 (c). The M-H is non-saturating even at the highest field due to the inhomogeneities associated with its structure. Variations of H_C and M_r with temperature are shown in figure 3-1.3 (d). It shows a hysteresis with H_C=1140 Oe and M_r=7.8 emu/g at 2 K and H_C=35 Oe and M_r=0.2 emu/g at 300 K that are in agreement with the earlier report [25, 30] and the loop disappears at higher temperatures. The room temperature loop is almost similar to that reported earlier [25, 26]. The coercivity value of 1140 Oe drops to 215 Oe as the sample is warmed to 50 K from 2 K and then a slow rate of decrease in H_C with temperature is observed. This is an indication of a decrease in strength of the FM

clusters and an increase in strength of the PM matrix. The straight line plot at 950 K, with no H_C, and M_r, shows the complete PM state. The M-H curves show a non-linear behavior at low fields (< 2 kOe) even above T_C, which is an indication of the presence of weak magnetization in the PM region.

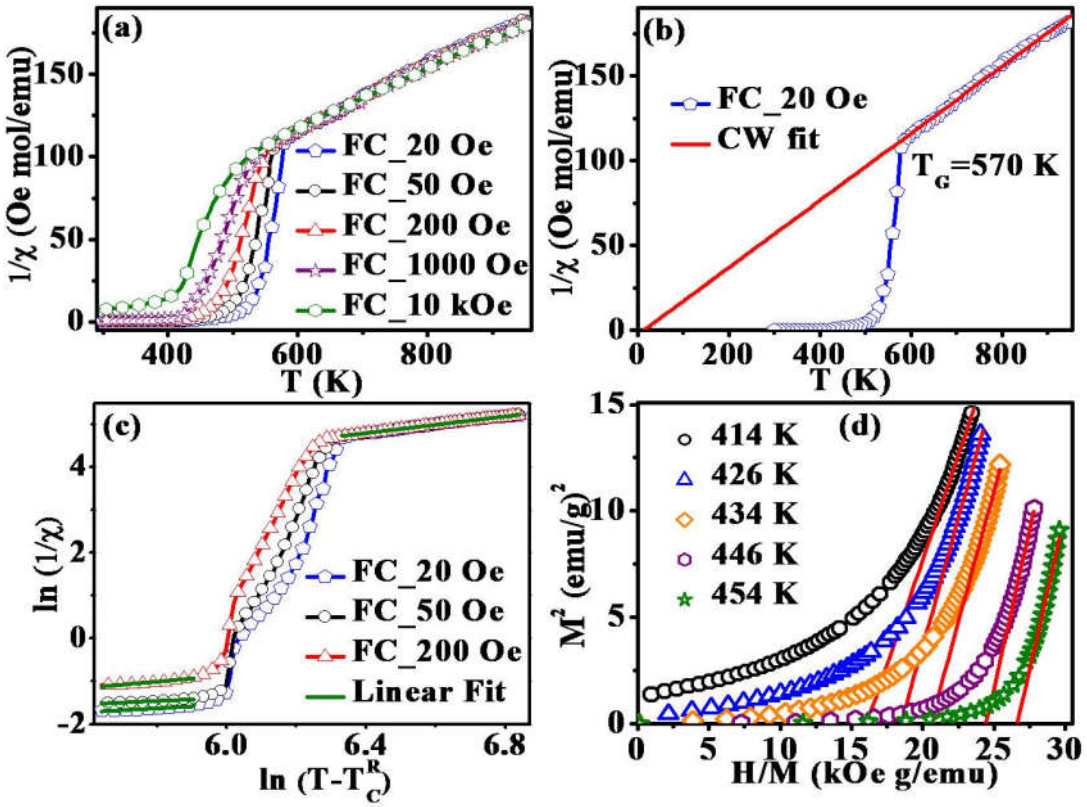

Figure 3-1.4 (a) Temperature dependence of inverse susceptibility (FC) at various fields. (b) CW fit (solid red line) on 1/χ (T) (FC) at 20 Oe. (c) ln (χ^{-1}) vs. ln ($T-T_C^R$) at 20, 50 and 200 Oe. The solid green line is the linear fit. (d) The Arrot plot (M^2 vs. H/M) at different temperatures below and above T_C. The solid red line is the linear fit.

The inverse susceptibility derived from FC magnetization for 20, 50, 200, 1000 Oe and 10 kOe is illustrated in figure 3-1.4 (a). A fit to Curie-Weiss (CW) law

$\chi = \frac{C_W}{T}$ for 20 Oe is shown in figure 3-1.4 (b). A CW fit is obtained only above T^*=570 K, and the presence of FSC is clearly evidenced in the plot as a sharp downturn below T^*, which is gradually reduced as the field is increased. This feature is usually considered as a manifestation of typical Griffiths-like phases (GP) [36-47]. GP was originally proposed as a randomly distributed Ising FM regions with nearest neighbor exchange interactions J and 0 with probabilities p and (1-p) respectively [45, 46]. The CW fit in PM region yields an effective magnetic moment, $\mu_{eff} = 2.828\sqrt{C_w}$ (C_W is the Curie constant) equal to 6.53(3) μ_B / f.u. The XPS spectra confirmed Fe^{3+} and Mn^{3+} spin states in La_2FeMnO_6. The theoretically expected μ_{eff} for La_2FeMnO_6 with Fe^{3+} and Mn^{3+} are given in Table 3-1.1. The obtained μ_{eff} proclaims that the Fe^{3+} and Mn^{3+} are not in a low spin state (LS) simultaneously, and if the spin-orbit coupling is present, Fe^{3+} should not be in LS. The FM state may arise from the high spin state (HS) Fe^{3+} (t_{2g}^3, e_g^2) and LS Mn^{3+} (t_{2g}^4, e_g^0), whereas the FiM state arises from LS Fe^{3+} (t_{2g}^5, e_g^0) and HS Mn^{3+} (t_{2g}^3, e_g^1), under certain strain conditions [24]. A recent study on La_2FeMnO_6 thin film confirmed AFM coupling of HS Fe^{3+} and HS Mn^{3+}, leading to FiM and observed an inverse relationship between saturation magnetization and Fe/Mn-order [35].

The disordered perovskite causes a random dilution of FM with different exchange interactions viz. superexchange and double exchange interactions as described before and causes the evolution of FSCs above T_C. The presence of inhomogeneous magnetic states, magnetic clusters and random competing exchange interactions in La_2FeMnO_6 are well reported previously [26-30]. Moreover, the quenched disorder, triggered by the random chemical replacement of ions of

different sizes can also induce intrinsic inhomogeneities in manganites [47-49]. The disorder is quenched within the distorted structure of La_2FeMnO_6 due to the strong coupling of Jahn-Teller distortion of the Fe^{3+}/Mn^{3+} ions and orthorhombic crystal lattice so that the FM bonds can be assumed as fixed within the lattice that form clusters and FSCs [47].

Table 3-1.1 Calculated μ_{eff} in units of μ_B/f.u. for La_2FeMnO_6 with Fe^{3+} and Mn^{3+}

Spin-Orbit Coupling	**Mn^{3+} (HS)**	**Mn^{3+} (LS)**
Fe^{3+} (HS)	5.916	5.916
Fe^{3+} (LS)	1.732	1.732
Spin Only interaction	**Mn^{3+} (HS)**	**Mn^{3+} (LS)**
Fe^{3+} (HS)	7.681	6.16
Fe^{3+} (LS)	5.196	3.317

Usually, the susceptibility of a Griffiths-like phase in low fields follows the power law [36-41, 43, 50, 51], $\chi^{-1} \propto (T - T_C^R)^{1-\lambda}$, where λ is the magnetic susceptibility exponent ($0 \leq \lambda \leq 1$) and T_C^R is the random critical temperature. T_C^R is taken as the temperature for which the equation yields a λ (λ_{PM}) value close to zero above T^*. The Θ obtained from CW fit is 18 K for 20 Oe (figure 3-1.4 (b)) and assuming T_C^R at 18 K well established a $\lambda_{PM} \approx 0.029(4)$. The linear part of the plot $\ln(\chi^{-1})$ vs. $\ln(T - T_C^R)$ (figure 3-1.6) is fitted with the power law and estimated the susceptibility exponent λ as 0.54(7) at 20 Oe and 0.29(6) at 200 Oe. The value of λ lies in between 0 and 1, and is decreasing with an increase in the field, a signature of

Griffiths-like phases [36-41, 43, 50, 51]. The Arrot plots (M^2 vs. H/M) at five different temperatures, below and above T_C are shown in figure 3-1.4 (d). The linear extrapolation to the high field region of the Arrot plot gives a negative M^2-axis intercept confirming the absence of a spontaneous magnetization (figure 3-1.4 (d)), with the existence of finite-sized FM interrelated spins without any static long-range magnetization [40, 41].

The presence of inhomogeneous magnetic phases with co-existence of FM and AFM states in La_2FeMnO_6 was reported where the FM phase originating from static Jahn–Teller distortions removed Mn^{3+}–O–Mn^{3+} dynamic interactions, and the AFM phase arising from Fe^{3+}–O–Fe^{3+} interactions [27]. De *et al.* reported a glassy complex system at low temperatures with two dynamical freezing points below room temperature (at 20 K and 255 K), in La_2FeMnO_6 due to phase separation that was observed in many mixed valence manganites and also due to the existence of several competing magnetic interactions induced by antiphase boundaries [28, 29]. Zhou *et al.* studied $LaMn_{1-x}Fe_xO_3$ ($0<x<1.0$) system and concluded that Mn favors double exchange interaction whereas Fe favors AFM superexchange [34]. Bhame *et al.* reported the material as a spin glass, with Fe^{3+} and Mn^{3+} ions having Mn-rich and/or Fe-rich clusters of different sizes, causing predominant FM or AFM interactions respectively [30]. These clusters are distributed within the lattice according to the synthesis conditions; wherein the magnetism is predicted by a two-phase model.

3-1.3.3 Specific heat and electron spin resonance spectra

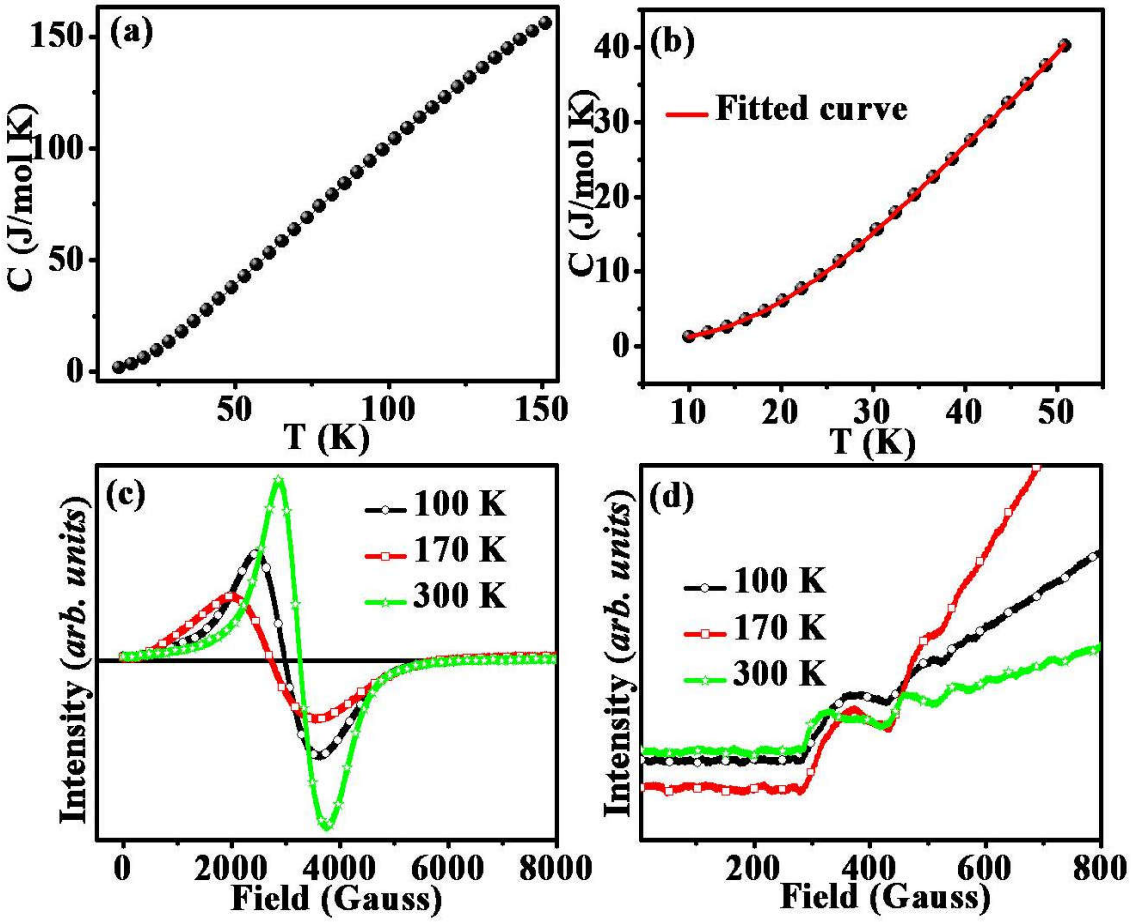

Figure 3-1.5 (a) Specific heat (C) as a function of temperature. (b) Low-temperature specific heat C fit. (c) ESR spectra of La_2FeMnO_6 at different temperatures. (d) Enlarged low field region of ESR spectra showing FMR signals.

To get a clear idea about the inhomogeneities, the specific heat (C) was measured for the temperature range of 10-150 K as shown in figure 3-1.5 (a). The low-temperature region from 10-50 K is fitted by using the polynomial [40] $C=\gamma T+\beta_3 T^3+\beta_5 T^5+\beta_7 T^7$ as shown in figure 3-1.5 (b). The γ gives the coefficient of electronic specific heat due to free charge carriers. The higher order T terms are the lattice contribution arising from phonons. The obtained values are γ=59.5(18)

$mJmol^{-1}K^{-2}$ for the linear term, β_3=0.694(5) $mJmol^{-1}K^{-4}$, β_5=-2.54(3)x10^{-4} $mJmol^{-1}K^{-6}$ and β_7=3.69(9)x10^{-8} $mJmol^{-1}K^{-8}$. The high value of the electronic linear contribution to the low-temperature specific heat could be an indication of the coexistence of FM metallic and charge ordered state [51]. A higher value of γ is obtained for materials having FSCs with GP [40, 43, 51].

The electron spin resonance spectra obtained at 100 K, 170 K, and 300 K are shown in figure 3-1.5 (c). ESR is highly sensitive to trivial magnetic correlations and is widely used for analyzing magnetic properties of manganites [49, 52, 53]. The ferromagnetic resonance signals, seen in the enlarged low field region of ESR spectra as shown in figure 3-1.5 (d) clearly demonstrate the presence of FSCs. The coexistence of PM resonance and FM resonance (FMR) signal is an indication of co-existence of PM and FM clusters [53].

3-1.4 Conclusions

In the present investigation, the disordered, orthorhombic La_2FeMnO_6 is found to possess double transition at T_{C1}=60 K and, T_C=425 K. The inverse susceptibility show a sharp downturn with temperature, below T*=570 K, as an indication of the occurrence of FSCs/GP. The oxidation states of cations are +3 (for Fe and Mn), and the effective PM moment is obtained as 6.5 μ_B / f.u. Fe^{3+}-O-Mn^{3+}, Fe^{3+}-O-Fe^{3+} and Mn^{3+}–O–Mn^{3+} superexchange interactions, and Mn^{3+}–O–Mn^{3+} dynamic FM interactions are present in the system. These competing interactions are responsible for the occurrence of a glassy-like transition near 60 K and Griffiths-like phase at higher temperatures. The total thermo-magnetic picture of La_2FeMnO_6 is as follows. At T_C^R = 18 K, a random dilution of FM phases starts due to the transition of

some of the magnetic phases. The FM clusters within the matrix interact with each other, and these clusters will undergo spin flipping with time and enters into a Griffiths-like phase above T_C^R. At T_{C1}=60 K, most of the FM phase will undergo magnetic transition into PM state, and at T_C=425 K, another magnetic transition occurs. Even though the T_C has reached, some of the FM clusters remain in the PM matrix and eventually transform completely into a PM state at T^*= 570 K, similar to a Griffiths-like phase. The Griffiths analysis yields a λ value equal to 0.54 at 20 Oe which decreases to 0.29 at 200 Oe. Below T_C, the FM clusters present themselves as a matrix in which PM clusters are embedded. Above T_C, it seems like the FM clusters are distributed within the PM matrix and eventually transforms to a complete PM state. The intrinsic inhomogeneities associated with the structure, quenched disorder related to the B-site cations and the antisite boundaries cause the presence of FSCs. The coefficient of low temperature electronic specific heat is as high as γ=59.5 $mJmol^{-1}K^{-2}$. The electron spin resonance spectra show ferromagnetic resonance signals pointing the possibility of the presence of FSCs at room temperature. Normally, magneto-transport properties co-exist with GP, which is done in the coming section of the present chapter. The coexistence of functionalities like FM, FiM, GP, magnetotransport coupling, etc. in a single material is of great interest for both the scientific aspects and for practical applications.

Section 3-2

Large positive and negative magnetodielectric coupling in La_2FeMnO_6

A large positive and negative magnetodielectric coupling is observed in disordered double perovskite La_2FeMnO_6. A charge localization phenomenon, spin glass property, and dielectric relaxation are observed in the material that is responsible to the origin of magnetodielectric effect.

3-2.1 Introduction

Magnetodielectric (MD) materials, with simultaneous magnetic and electric dipolar ordering, are rare due to the conflicting structural and electronic requirement [54]. They are attractive from scientific and technological aspects and are promising candidates for spintronic devices, in which the spin and charge degrees of freedom of electrons are controlled by the application of an external magnetic field [54-57]. The systems with strongly coupled magnetic and electronic degrees of freedom can have an interplay between ferromagnetism and charge order as observed in manganites showing magnetoresistance (MR) [58]. In the limit of localized charges, the coupling is mainly manifested through MD effects [58]. Competing magnetic and electronic phases usually arise in transition metal perovskite oxides [55-57]. A transition from a paramagnetic insulator to a ferromagnetic metal phase usually offers large MR while a magnetic transition or dielectric ordering with a semiconducting or insulating behavior give rise to an MD coupling [58-60]. Maximum MD coupling was observed around a magnetic or electric transition for the double perovskites La_2NiMnO_6 [61], La_2CoMnO_6 [62], Sm_2NiMnO_6 [63], Gd_2NiMnO_6 [64], etc. Ferromagnetic (FM) or antiferromagtic (AFM) materials like $SeCuO_3$, $TeCuO_3$ have a fluctuating spin-pair correlation around the T_C and originates MD coupling [59, 60]. Spin-phonon coupling and charge fluctuation originate MD in materials having a charge ordered state [58, 65, 66].

A spin-lattice coupling was assumed to be responsible for a negative MD coupling of 15 % (at 250 K) for a highly ordered La_2NiMnO_6 system [67]. A partially disordered La_2NiMnO_6 is showing a negative MD (20% at 270 K) attributed to the glassy dielectric properties [13]. For the La_2NiMnO_6 nanoparticles,

negative MD of 30% (at 215 K) is observed around the broad relaxor dielectric peak temperature (220 K) and near to the ferromagnetic transition temperature (196 K) [68]. La_2NiMnO_6 thin films show positive and negative MD, based upon the annealing temperature due to the Maxwell-Wagner (M-W) effect [69]. A very large value of positive MD (50 % at 115 K) originated by the influence of magnetic field on the dipolar relaxation was reported for La_2NiMnO_6 epitaxial film [61, 70]. A small positive extrinsic MD of 4% (at 80 K) was reported for La_2NiMnO_6 nanoparticles where the long range ferromagnetic ordering was absent [71]. Similarly, a positive MD of 2.2% (at 220 K) is reported for La_2NiMnO_6 with less Ni/Mn ordering which is attributed to an extrinsic origin by interfacial polarization [72]. A positive MD response of 11% at 220 K near to T_C was observed for La_2CoMnO_6 nanoparticles as a result of the coupling of dipolar relaxation with magnetic order parameter [73]. A very large MD of +110 % (at 90 K) was reported for La_2CoMnO_6 nanoparticles due to the presence of spin–lattice anomaly below T_C [62]. The basic mechanisms behind the MD coupling are reported to be spin-lattice/spin-phonon coupling, asymmetric hopping between ions, magnetostriction, exchange striction, charge ordering, MR, influence of a magnetic field on the dipolar relaxation, extrinsic factors like grain boundaries, interfacial polarization (Maxwell–Wagner (M-W) effect), etc. [13, 61-64, 74].

Though the MD properties of La_2NiMnO_6 and La_2CoMnO_6 are well studied, MD of its Fe counterpart La_2FeMnO_6, is not yet explored completely. La_2FeMnO_6 is known to possess a Griffiths phase (GP) with Griffiths temperature T*=570 K and a random critical point T_C^R=18 K as reported in section 3-1 [75]. Thus La_2FeMnO_6 is a diluted ising ferromagnet having paramagnetic correlations below T_C=425 K until

T_C^R and ferromagnetic correlations above T_C up to T* [45, 75]. Accordingly, multiple temperature zones for a successful magnetodielectric coupling are expected for the material, provided a change in electric phase.

In the present investigation, we identified La_2FeMnO_6 as a material that exhibit both the positive and negative magnetodielectric (MD) effects at different temperature regions with a very large MD coupling. DC resistivity (charge transfer) mechanism, spin glass property, and the dielectric relaxation are correlated to the observed large positive and negative MD coupling in La_2FeMnO_6.

3-2.2 Experimental details

La_2FeMnO_6 is synthesized by citrate-gel combustion method as described in the previous section [75]. In the present investigation, the samples for dielectric, transport properties etc were needed as sintered pellets with maximum density. Hence the final sintering temperature is increased to 1000º C for 6 hours. The sintered pellets were powdered for phase purity analysis. X-ray diffraction (XRD) is obtained by using the Philips PANalytical X'Pert Pro Powder X-Ray Diffractometer with a Ni-filtered Cu Kα radiation (λ=1.5406 Å) at 100 K and 300 K. The Rietveld structural refinements were by GSAS EXPGUI. JEOL JSM 5610 scanning electron microscope (SEM) was used to image the microstructure of the sintered pellets. X-ray photoelectron spectra (XPS) corresponding to Fe 2p and Mn 2p of La_2FeMnO_6 were obtained by a Thermo Scientific X-ray photoelectron spectrometer, MULTILAB 2000 Base system with x-Ray, Auger, and ISS attachments. The binding energies were corrected by taking C 1s as reference energy, and the XPS peaks were fitted by using XPS PeakFit software. The physical properties viz.

resistivity, specific heat, DC magnetization, and AC magnetic susceptibility of La_2FeMnO_6 are measured by using Physical Property Measurement System (PPMS - Quantum Design, Dynacool). The rectangular pellet was used for the resistivity measurement from 83-300 K. Specific heat of small solid pellet piece is measured for temperatures 65-150 K. DC magnetic moments are measured for 2-380 K and ±90 kOe with various protocols. Differential Scanning Calorimetry (DSC) was done by NETZSCH DSC 204F1 Phoenix. The dielectric constant and dielectric loss tangent are measured on the circular pellet kept inside a closed cycle Cryocooler (ARS-2HV) by using an LCR meter (Agilent E4980A). A magnetic field was applied on the capacitor connection by inserting a hollow cylindrical Neo magnet above the sample, and the magnetodielectric coupling was determined. AC magnetic susceptibility, dielectric constant, and loss tangent were measured, and the magnetodielectric coupling was determined in the temperature range 40-285 K at different frequencies.

3-2.3 Results and Discussion

3-2.3.1 Structural characterization

Phase purity with an orthorhombic *Pbnm* crystal structure is confirmed for the synthesized La_2FeMnO_6 by X-ray diffraction (XRD) analysis. The calculated and the observed XRD patterns along with the difference curve obtained after the structural refinement by using GSAS at temperatures 100 K and 300 K are given in figure 3-2.1 (a) and 3-2.1 (b) respectively. The parameters obtained from the refinement of XRD at 100 K and 300 K are compared in Table 3-2.1.

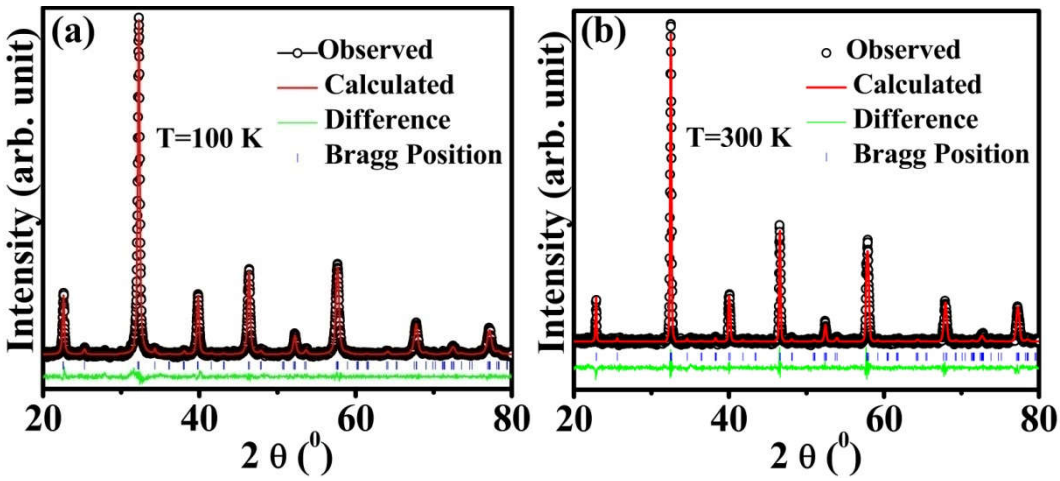

Figure 3-2.1 Observed and calculated powder XRD patterns of La_2FeMnO_6 along with the difference curve and Bragg positions at (a) 100 K and (b) 300 K.

Table 3-2.1 Lattice parameters, bond lengths, bond angle, J-T and angle distortion along with reliability factors for the structural refinement of La_2FeMnO_6 at 100 K and 300 K.

	at 100 K	***at 300 K***
Lattice parameters		
a (Å)	5.5069(5)	5.5082(2)
b (Å)	5.5300(7)	5.5413(2)
c (Å)	7.7853(8)	7.8092(3)
α, β, γ (º)	90	90
<Fe/Mn-O> Bond length (Å)		
	1.868	1.906
	1.995	1.977
	2.070	2.050

J-T distortion Δd (10^{-4})		
	17.6	8.8
<Fe/Mn-O-Mn/F> Bond Angle <θ> (°)		
	154.6	161.8
	164.4	162.0
Angle distortion <ω> (°)		
$\langle\omega_1\rangle$	25.4	18.2
$\langle\omega_2\rangle$	15.6	18.0
$\langle\omega\rangle$	20.5	18.1
Reliability factors		
$_{W}R_{P}$ (%)	6.45	4.6
R_P (%)	4.79	3.5
χ^2	2.01	1.4

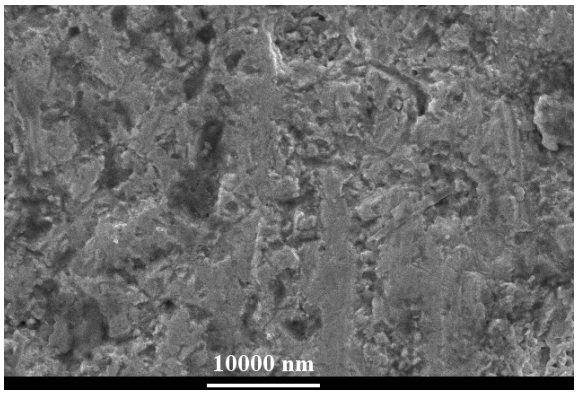

Figure 3-2.2 (c) SEM image showing the surface of the sintered pellet.

The surface SEM image of the highly densified pellet taken at 10 kV is shown in figure 3-2.2. The X-ray photoelectron spectra (XPS) corresponding to Fe 2p and Mn 2p of La_2FeMnO_6 are analyzed by using XPS PeakFit software. The XPS

spectra for Fe $2p_{3/2}$ depict two curves with peak positions at 710.05 eV and 711.23 eV corresponds to Fe^{2+} and Fe^{3+} cations respectively (figure 3-2.3 (a)) [76, 77]. Similarly, the XPS spectra for Mn $2p_{3/2}$ give curves with peak positions at 642.93 eV and 641.59 eV as shown in figure 3-2.3 (b) that points the presence of Mn^{4+} and Mn^{3+} cations in the material [78, 79].

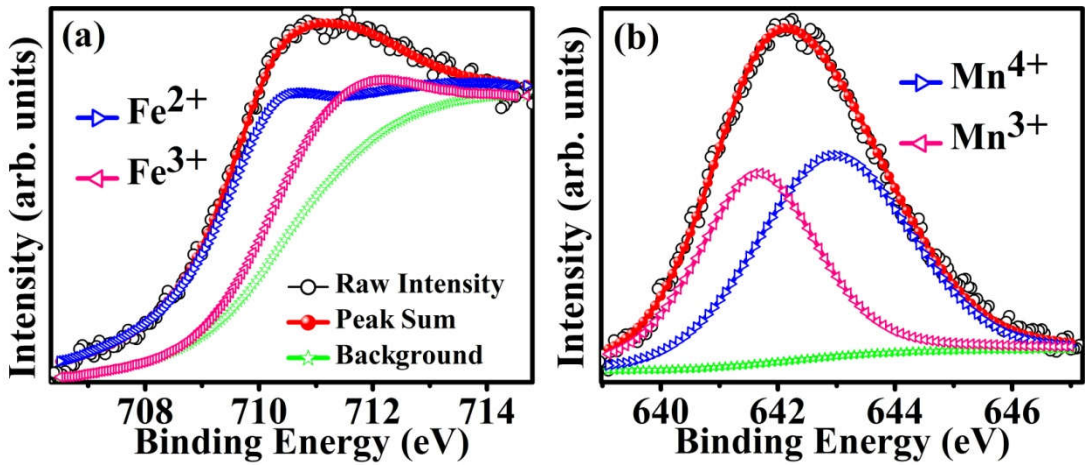

Figure 3-2.3 XPS spectra of La_2FeMnO_6 along with the fitted curves for (a) Fe $2p_{3/2}$ showing Fe^{2+} and Fe^{3+} and for (b) Mn $2p_{3/2}$ showing Mn^{4+} and Mn^{3+}.

The La_2FeMnO_6 material sintered at 900 ºC is reported to possess Fe^{3+} and Mn^{3+} cations as described in section 3-1 [75]. In the present study, the sintering temperature is increased to 1000 ºC to get maximum density intended for the dielectric measurements. This high-temperature sintered material has the same *Pbnm* crystal structure with a small variation in the lattice constants and contains cations of mixed oxidation state as evident from XPS studies. There are earlier reports on the existence of mixed valance state cations in La_2FeMnO_6 [26]. The mixed states of cations in the perovskite structure are stabilized when the FeO_6 octahedra are surrounded by the MnO_6 octahedra and vice versa [80]. The *Pbnm* structure and the

mixed valence of cations of La_2FeMnO_6 characterize a random distribution of the cations in the octahedra and a disordered perovskites structure [12].

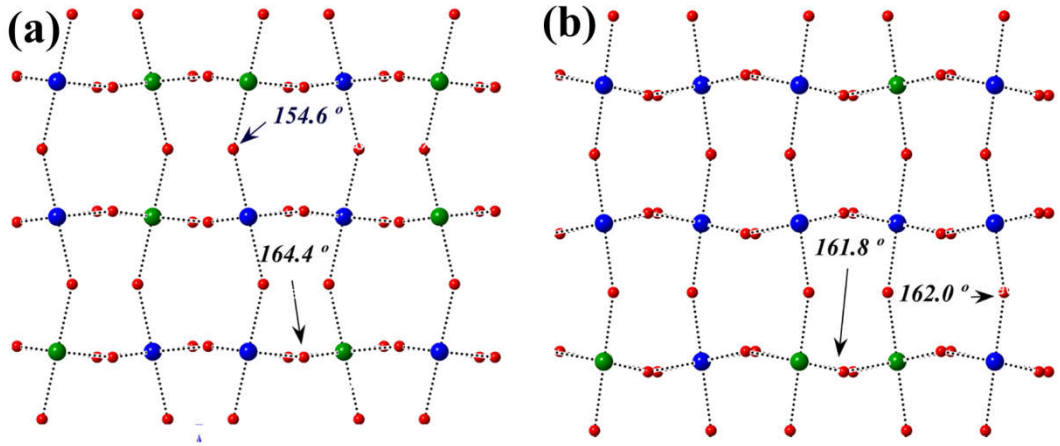

Figure 3-2.4 The arrangements of Mn/Fe-O-Fe/Mn bonds (Blue/Green-Fe/Mn and Red-O) marked with bond angle (b-axis view) for (a) 100 K (b) 300 K.

The Jahn-Teller (J-T) ion Mn^{3+} have electronic configuration $[Ar]4s^0 3d^4$ with outermost d-shell electronic configuration $(t_{2g})^3(e_g)^1$. The e_g electron will find both $d_{x^2-y^2}$ and d_{z^2} orbital with same energy and fill in a particular orbital asymmetrically which lead to an increase in the system energy. To minimize this system energy, the system undergoes a structural distortion. The asymmetric arrangements of the Fe/MnO_6 octahedra in *Pbnm* structure became disordered due to the mixed valence of cations and the J-T distortion. As given in the Table 3-2.1, the J-T distortion [81] calculated by the equation $\Delta d = \frac{1}{6}\sum_1^6 \left[\left(d_n - \langle d\rangle\right)/\langle d\rangle\right]^2$, is larger for 100 K than that for 300 K. The angle distortion calculated by the equation $\langle\omega\rangle = 180 - \langle\theta\rangle$ is also higher for 100 K than that for 300 K. These results indicate that the octahedra present in the crystal at 100 K are more structurally distorted than that at room temperature. The two types of <Fe/Mn-O-Mn/Fe> bond angles ($\langle\theta\rangle$) at 100 K are

154.6º and 164.4º, whereas the bond angles are almost the same (161.8º and 162.0º) at 300 K. The arrangements of Mn/Fe-O-Fe/Mn bonds marked with bond angles in a b-axis view for 100 K and 300 K are shown in figure 3-2.4 (a) and (b) respectively. The hopping conduction between adjacent sites depends on the bond angle which can result in a different conduction mechanism active at low temperatures.

3-2.3.2 DC transport properties and charge ordering

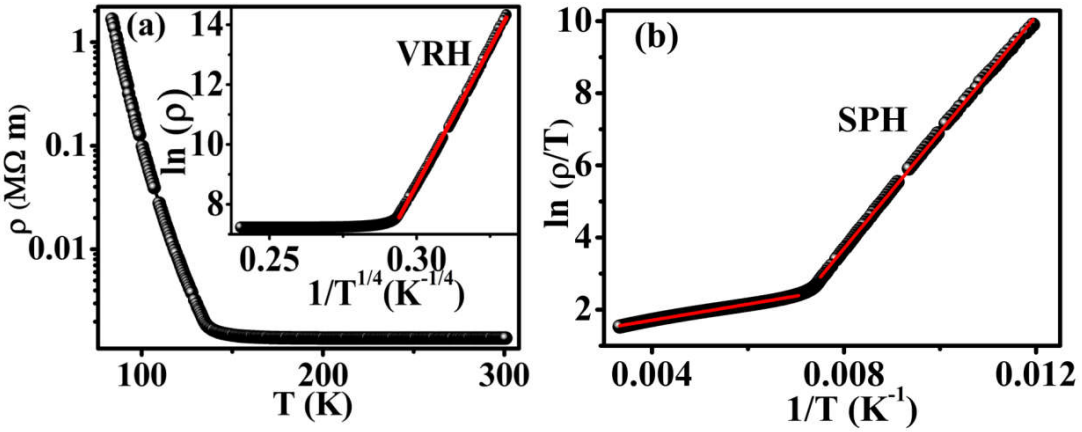

Figure 3-2.5 (a) Variation of resistivity (ρ) with temperature. The inset shows ln (ρ) vs. $1/T^{1/4}$ plot with a linear fit (red) for the VRH model. (b) ln (ρ/T) vs. 1/T plot with a linear fit (red) for the SPH model.

The charge carriers usually follow a cozy path to conduct electricity through a material. A signal of charge ordering is observed in the resistivity (ρ) vs. T curve of La_2FeMnO_6 as a steep increase in the value on cooling, as shown in figure 3-2.5 (a). A charge localization (like an ordered state) can be formed in the orthorhombic domains of the perovskite structure where the charges are localized to form a freeze-like state with insulating nature [82]. A charge ordered/localized state appears in the low temperature distorted phase [83] whilst the J-T distortion of 17.6 and angle distortion of 154.6º present a comparatively more distorted phase at 100 K (than

that at room temperature). Around the charge localization temperature (T_{CL}=133 K), ρ follows different conduction mechanisms with a change in slope in the ρ(T) [29, 82, 84, 85].

Table 3-2.2 The fitted parameters obtained from the resistivity data.

VRH		
	ρ_0 (Ω m)	**T_0 (K)**
$T<T_{CL}$	1.65×10^{-21}	1.13×10^{9}
SPH		
	A (Ω m K^{-1})	**E_A (eV)**
$T<T_{CL}$	1.02×10^{-4}	0.14
$T>T_{CL}$	2.25	0.02

The ρ is analyzed by variable range hopping (VRH) model [86] which is described as $\rho = \rho_0 \exp\left(\frac{T_0}{T}\right)^{1/4}$, where ρ_0 is the pre-exponential factor, and T_0 is the characteristic temperature and small polaron hopping (SPH) model [87] which is described as $\rho = AT \exp\left(\frac{E_a}{k_B T}\right)$ where A is the pre-exponential factor and E_a is the activation energy required for the conduction process. Figure 3-2.5 (b) shows the fitting of ρ data with SPH model. A change in the slope of the fitted data at T_{CL} suggests a variation in activation energy between a charge-active high-temperature region and a charge-localized low-temperature state. The observed E_A in the SPH fit for $T<T_{CL}$ is larger than that for $T>T_{CL}$, showing the difficulty for the small polarons

to move through the freeze-like charge ordered state. The inset of figure 3-2.5 (a) shows the fitting of ρ data with VRH model below T_{CL}. Since VRH is the localized variable range hopping of charge carriers, the absence of a VRH active region above the observed T_{CL} is a manifestation of the delocalized charge carriers [88]. A combination of the VRH and SPH mechanisms is valid for the conduction in the charge localized state whereas SPH is the mechanism governing the conduction in the charge disordered/delocalized state [85]. An asymmetric hopping of charge carriers is happening around T_{CL}. The parameters obtained from the fitting are tabulated in Table 3-2.2.

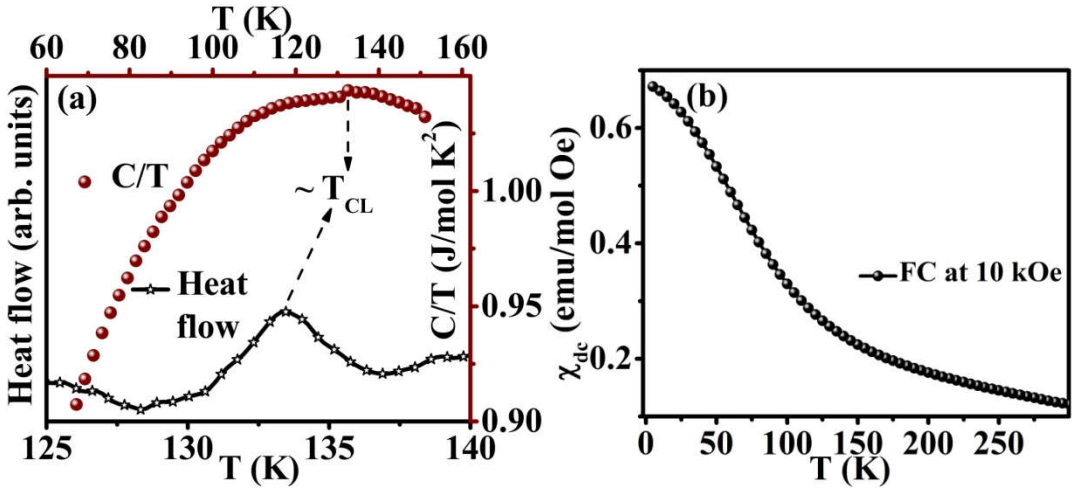

Figure 3-2.6 (a) Differential scanning calorimetry (left y-axis and bottom x-axis), showing a peak and C/T vs. T (right y-axis and upper x-axis) showing a kink near the T_{CL}. (b) Variation of DC susceptibility with temperature for field cooled measurement at 10 kOe.

To confirm the charge localization, the specific heat (C) and differential scanning calorimetry (DSC) data around T_{CL} are analyzed. A change in internal energy of the material system can be expected during the charge localization/delocalization phenomenon which can be evidenced from the specific

heat and DSC data [88, 89]. The C/T vs. T and heat flow vs. T are plotted to account for the possibility of charge localization (figure 3-2.6 (a)). It shows a small step-like kink in the C/T vs. T curve and a hump in the heat flow vs. T plot near the observed T_{CL}.

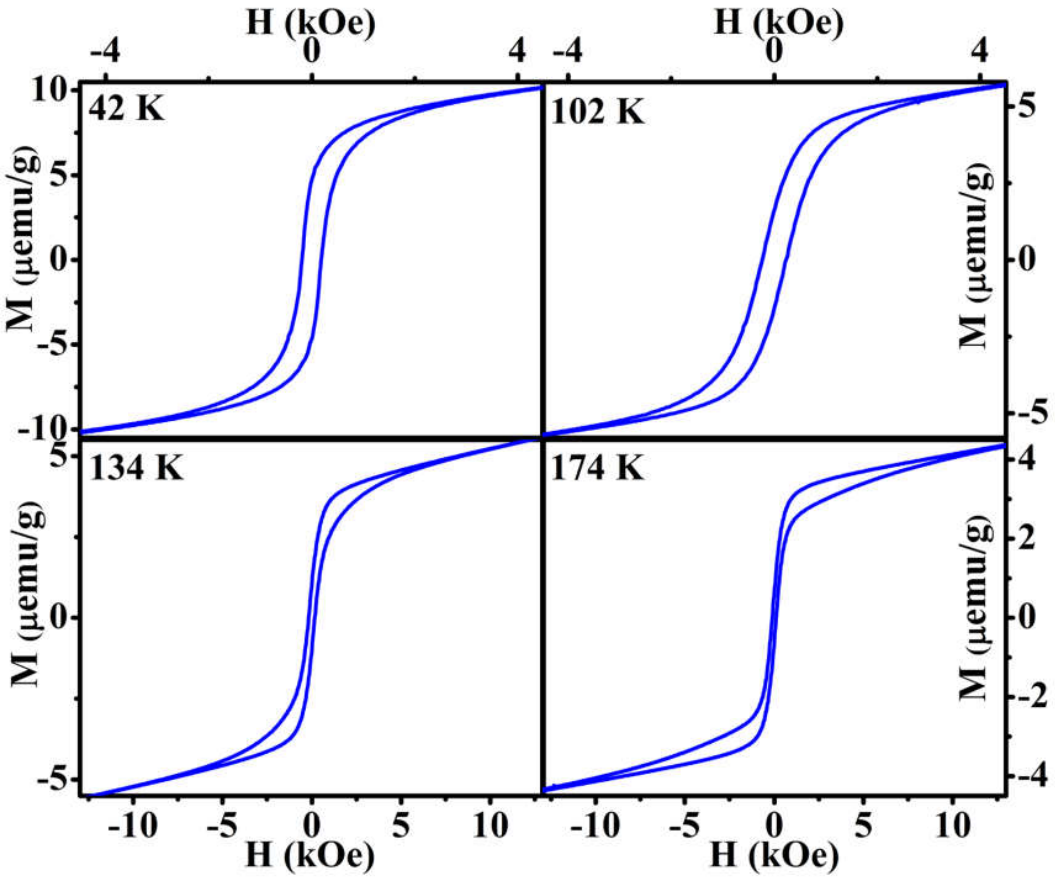

Figure 3-2.7 Magnetic moment vs. magnetic field at 42 K, 102 K, 134 K, and 174 K depicting the formation of wasp-waisted hysteresis loop near and above T_{CL}.

The presence of four types of cations would puzzle 'how and in which order' the cations/charges order. The <Fe-O-Mn> bond angles at 300 K are almost equal while that at 100 K are differing as shown in figure 3-2.4 (a) and (b) which gives an insight into the phenomenon of charge localization. The actual charges, ordering at low temperatures, stuck to ions leading to the increased insulating nature [90].

Charge ordering/localization can be viewed either as a disorder–order (charge disorder–charge order) transition in which Fe^{2+} and Fe^{3+} order on one of the Fe sub-lattices and Mn^{4+} and Mn^{3+} order on one of the Mn sub-lattices or as a disproportionation-driven transition [90-92]. A local moment formation will be favored by the strong correlations effects by the confinement of charges (intersite Coulomb repulsion) or vice versa [93]. Thus the increase in magnetic moment (χ_{DC} vs. T plot in figure 3-2.6 (b)) below T_{CL} further confirms the charge confinement [93].

The magnetic hysteresis (MH) loops taken both above and below T_{CL} are shown in figure 3-2.7. The MH above T_{CL} (134 K and 174 K) demonstrated a wasp-waisted (W-W) hysteresis loop, while that below T_{CL} (42 K and 102 K) does not show any W-W hysteresis loop. W-W MH loop is commonly found in mixed magnetic assemblages that may be generated by the changes in spin exchange coupling between the cations above T_{CL} [94, 95]. For understanding the glassy magnetic behavior, the AC susceptibility (χ) as a function of temperature is performed at various frequencies.

3-2.3.3 AC magnetic susceptibility

The imaginary part of χ_{ac}(χ_{ac}") vs. T at various frequencies is shown in figure 3-2.8 (a). Peaks at 85 K and ~220 K are observed for χ_{ac}". The peak at 85 K shows no frequency dependent shift which can be a kind of FM transition. The peak at 220 K shows a shift towards higher temperatures as frequency is increased and can be originated from spin-lattice relaxation [96]. Usually the relaxation time follows the Arrhenius law: $\tau = \tau_0 \exp\left(\frac{E_a}{k_B T_m}\right)$, where $\tau = (2\pi f)^{-1}$, f is the frequency, τ_0 is the

characteristic relaxation time, E_a is the activation energy, T_m is the temperature for peak maximum. The linear fit as shown in Figure 3-2.8 (b) gives a value of $\tau_0=8.44x10^{-14}$ s, which concludes the spin glass property of the material with a faster spin-flipping. The spin-lattice vibrations, realized through phonons (lattice vibration) can be assumed to be originating from fluctuating charge carries as it is observed above T_{CL} [96].

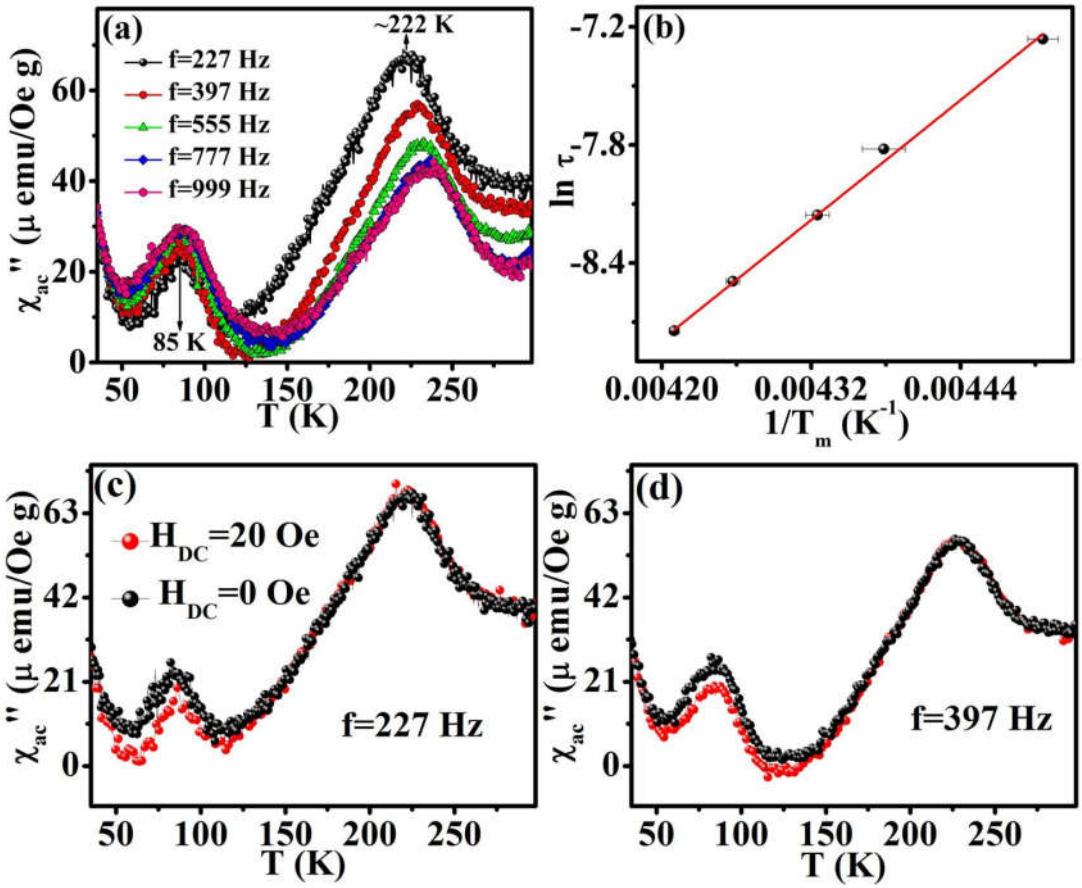

Figure 3-2.8 Variation of (a) imaginary part of AC susceptibility with temperature at various frequencies. (b) ln τ vs. $1/T_m$ plot along with the Arrhenius fit (solid red line). Variations of the imaginary part of AC susceptibility with temperature with and without a DC field at (c) 227 Hz and (d) 397 Hz.

The χ_{ac}" is measured with and without a DC magnetic field of 20 Oe at 227 Hz and 397 Hz as shown in figure 3-2.8 (c) and (d). The external DC field suppresses the peak in χ_{ac}" around 85 K whereas there is no field dependent change to the peak maximum in χ_{ac}" around 220 K. Since the χ_{ac}" gives the dissipated energy, the external field will reduce its value around FM transition whereas there is no considerable effect is observed around a spin glass transition [63, 96].

3-2.3.4 ZFC memory and aging tests

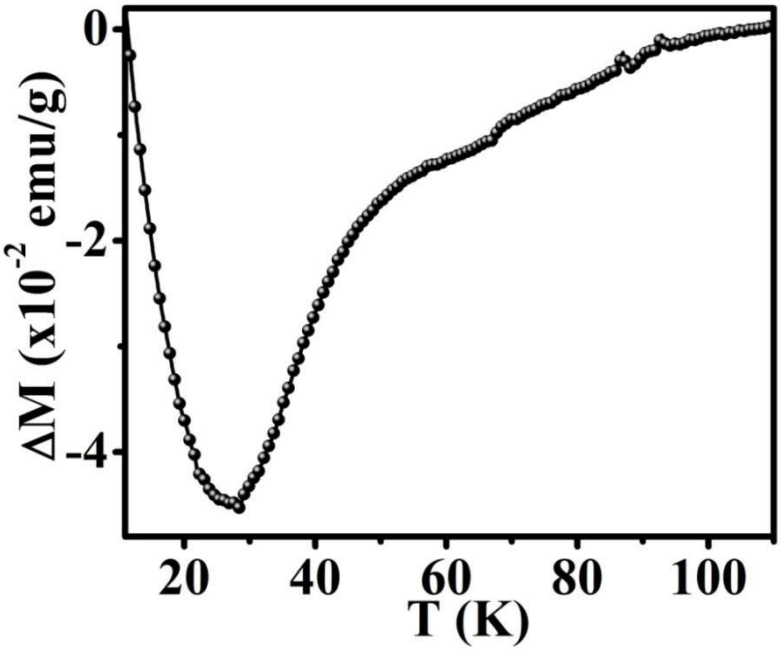

Figure 3-2.9 The variation of ΔM as a function of temperature.

The ZFC memory experiment and aging tests were performed to confirm the spin glass behavior of La_2FeMnO_6. While cooling from 380 K under ZFC condition, the sample was subjected to a wait time of 7200 s at an intermittent temperature 30 K, followed by cooling to 2 K. A dc magnetic field of 100 Oe was applid and the magnetic moment (M_{ZFCMem}) was recorded upon warming. The ZFC magnetic moment vs. temperature was recorded without a wait time at an intermittent point

(M_{ZFC}) . The difference between these curves (ΔM) is plotted as shown in figure 3-2.9. A memory of the wait time around 30 K is shown by the material, which is a characteristic feature of spin glass systems.

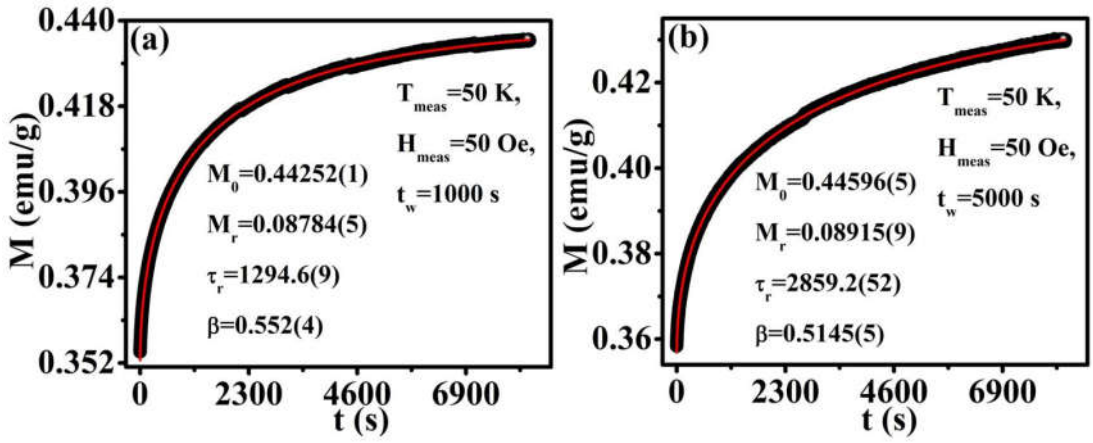

Figure 3-2.10 (b) Time evolution of ZFC magnetic moment measured at H_{meas}=50 Oe, T_{meas}=50 K, and t_w=1000 s, and 5000 s. Solid red lines are the best fit to the stretched exponential function.

For further confirmation, the aging measurement was carried out. During this test, the sample is cooled from 300 K (above the spin glass transition point) to the measuring temperature T_{meas} = 50 K. The sample was kept at T_{meas} for a wait time of t_w (1000 s, and 5000 s). Further the magnetic moment was recorded as a function of time with an applied dc field of 20 Oe. The time-dependent magnetization usually follows the stretched exponential function $M(t) = M_0 - M_r exp\left\{\left(-t/\tau_r\right)^{\beta}\right\}$, where M_0 is the intrinsic FM component, M_r is the glassy component, τ_r is the characteristic relaxation time, and β is the stretching parameter [97-99]. The time-dependent magnetization at T_{meas}=50 K, and H_{meas}=50 Oe along with the fitted curve for t_w=1000 s and 5000 s are shown in figure 3-2.10 (a) and (b) respectively. M_0, M_r, and τ_r, shows increase with t_w. The β shows a small decrease with t_w, however the

value $\beta \approx 0.5$ lies in the range reported for many spin glass systems [97, 100]. The value of β is less than 1 since multiple anisotropy barriers are distributed in the material. This is a characteristic feature of spin glass systems [97, 99, 101].

3-2.3.5 Dielectric properties

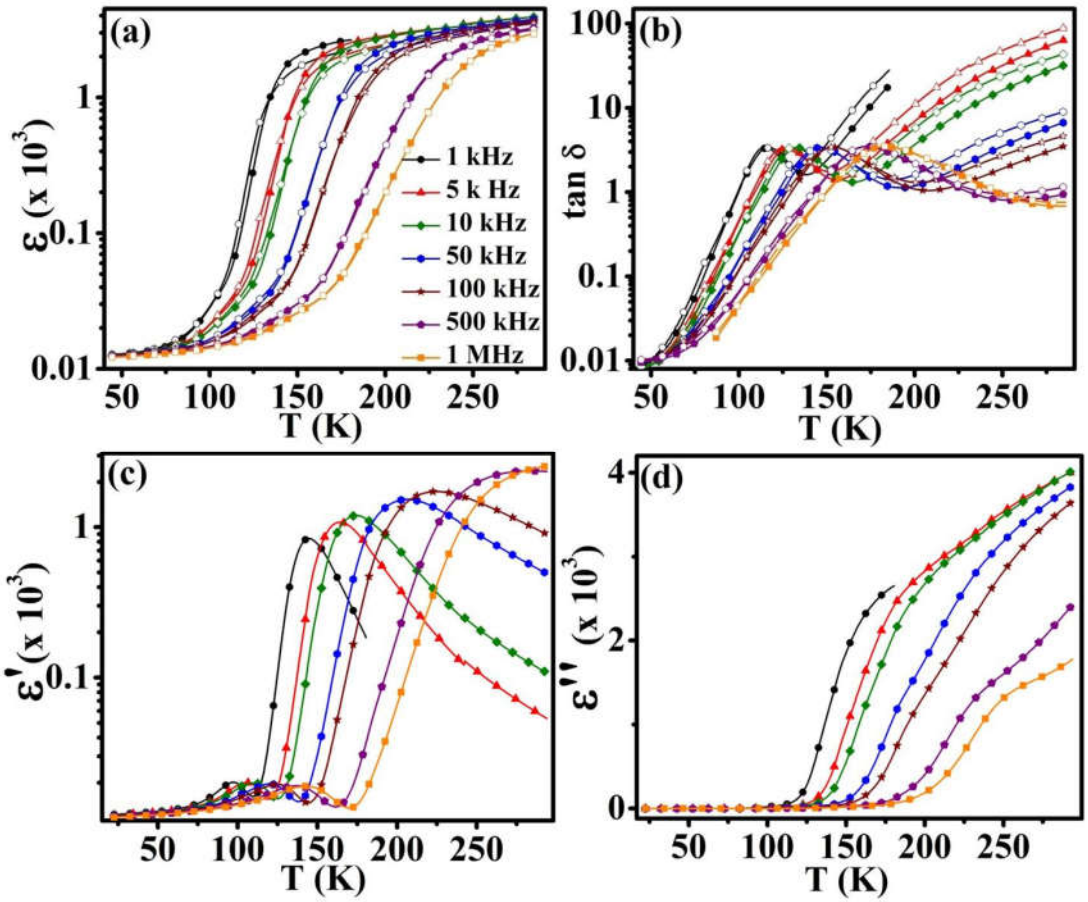

Figure 3-2.11 Variation of (a) ε (Closed symbols at 0 Oe and open symbols at 5 kOe), (b) tan δ (Closed symbols at 0 Oe and open symbols at 5 kOe), (c) ε' and (d) ε'' with the temperature at various frequencies.

Variation of dielectric constant (ε) and loss tangent (tan δ) with temperature at different frequencies are shown in figure 3-2.11 (a) and (b) respectively. The values are measured with and without a magnetic field of 5 kOe. The heat

dissipation associated with the movement of charge carriers is usually related to the loss tangent (tan δ) and can be converted into the formation of phonons [102]. A peak is observed in tan δ around T_{CL} that shifts to higher temperatures with increase in frequency. The relaxation time for tan δ is fitted with Arrhenius law as shown in figure 3-2.12 (a).

A temperature dependence of real part of ε (ε') at various frequencies is shown in figure 3-2.11 (c). The ε' is related to the intrinsic behavior of a material. ε' demonstrates low-temperature relaxation and a high-temperature broad relaxation. The relaxation time corresponding to both the relaxations follow the Arrhenius law as shown in figure 3-2.12 (b) and (c) respectively. For the low-temperature range, the maximum value of ε' (ε'_m) is lowered with frequency while ε'_m is increased with frequency in the high-temperature range. The spin glass transition around 220 K and the high-temperature relaxation in ε' are appearing in the charge delocalized state. The imaginary part of ε (ε") is shown in figure 3-2.11 (d). ε" is usually related to the movement of charge carriers, and it starts increasing near T_{CL} only. The characteristic relaxation times and activation energies, calculated for different relaxations from the Arrhenius fit, are tabulated in Table 3-2.3. The obtained values of τ_0 (10^{-10}-10^{-14} s) suggest that the relaxation processes are associated with dipolar reorientation phenomenon [96].

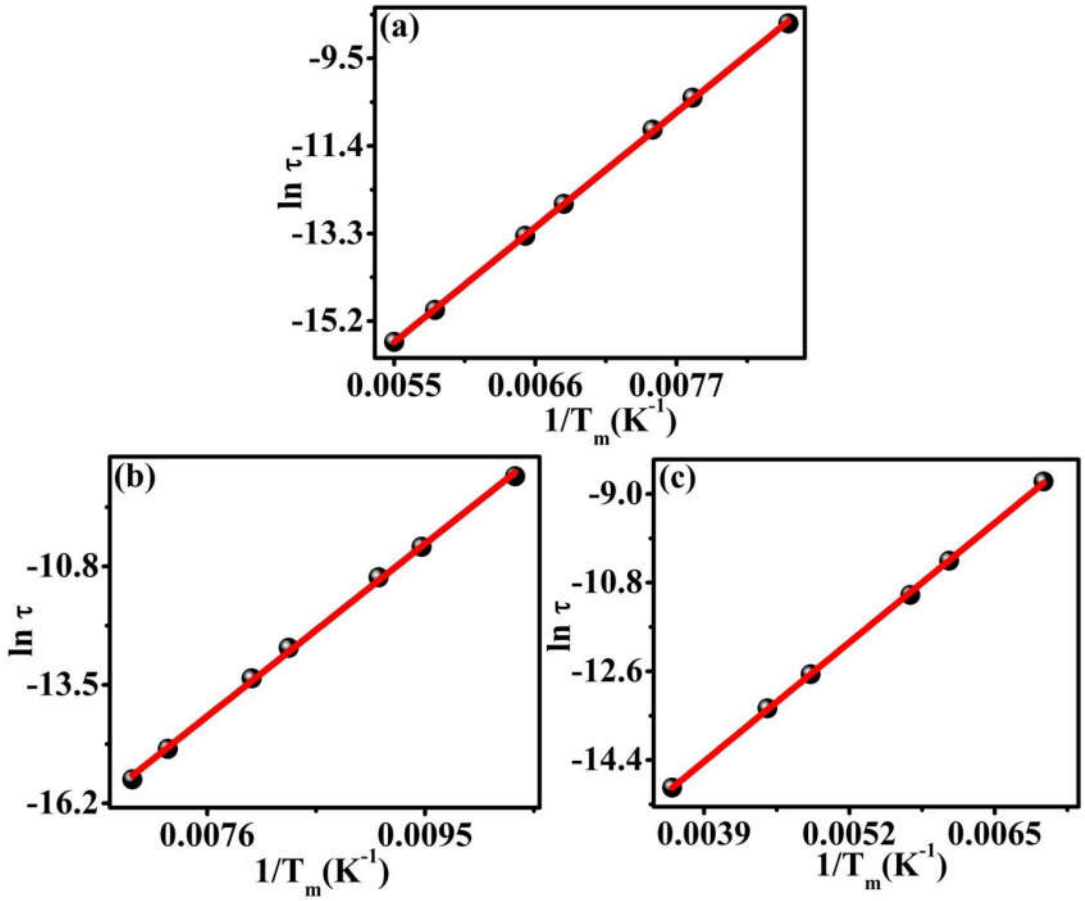

Figure 3-2.12 Arrhenius fits (solid red line) for the relaxations in (a) tan δ, (b) low-temperature relaxation in ε', and (c) high-temperature relaxation in ε'.

Table 3-2.3 The characteristic relaxation times and activation energies calculated for different relaxations obtained from the Arrhenius fit.

	τ_0	E_a
Relaxation in tan δ	6.11×10^{-13} s	0.19 eV
Low-temperature relaxation in ε'	9.89×10^{-14} s	0.18 eV
High-temperature relaxation in ε'	3.77×10^{-10} s	0.16 eV

3-2.3.6 Magnetodielectric coupling

The ε and tan δ for 0 Oe (closed symbol) and 5 kOe (open symbol) are shown in figure 3-2.11 (a) and (b). The MD coupling $\left(MD\% = \frac{[\varepsilon_H - \varepsilon_0]}{\varepsilon_0} \text{ x } 100 \right)$ and MD loss (MDL) coupling $\left(MDL\% = \frac{[\tan\delta_H - \tan\delta_0]}{\tan\delta_0} \text{ x } 100 \right)$ are calculated and plotted in figure 3-2.13 and inset of figure 3-2.13 respectively. As shown in the figure 3-2.13, the material exhibits both the positive and negative MD coupling [74, 103, 104]. Almost 0% MD and MDL are observed till ~70 K. A small positive MD of 0 - 4.5% is observed for 70 -100 K region, with 4.5% MD at 85 K, where the first peak in χ_{ac}'' is obtained. The temperature corresponding to the maximum MD (4.5%) is frequency independent alike to the peak at 85 K in χ_{ac}''. On approaching the T_{CL}, a high positive MD of 0 - 45% is observed in a temperature range of 100 - 140 K with a maximum MD at 122 K for a frequency of 1 kHz. The low-temperature relaxation in ε' is observed around this temperature. In this region, the magnetic field and magnetic order parameter influences the dipolar relaxation and is responsible for the observed high positive MD in La_2FeMnO_6 as reported for La_2NiMnO_6 film and La_2CoMnO_6 nanoparticles [61, 70, 73, 105].

Above T_{CL}, the material exhibits a colossal negative MD of -18% at 147 K for 1 kHz. On increasing the temperature further, MD reaches -6.8% near room temperature (284 K) for about 5 kHz. The extent of charge fluctuations get reduce above T_{CL} on application of magnetic field and causes a drop in the value of ε and a negative MD value [65, 106]. The maximum negative MD is observed around the temperature of spin glass transition and the high-temperature dipolar relaxation in ε'.

A spin-lattice coupling and the glassy dielectric properties were assumed to be responsible for the origin of negative MD coupling in many systems, particularly in manganites [13, 58, 61, 66-68, 70].

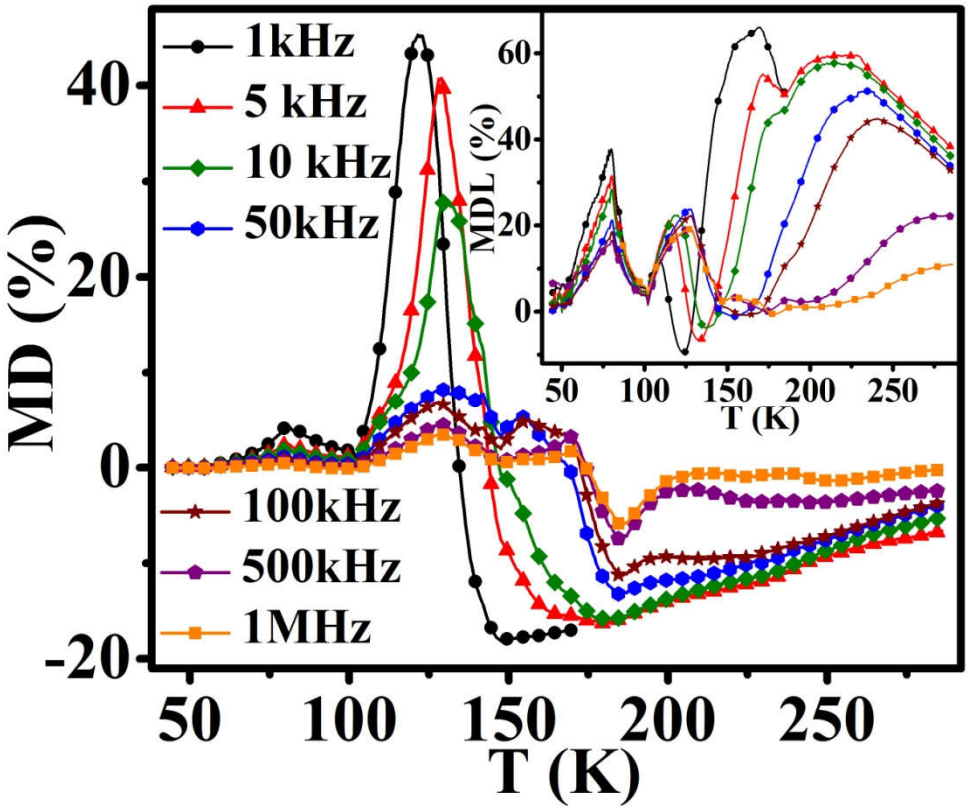

Figure 3-2.13 Variation of MD and MDL (inset) with the temperature at various frequencies.

Asymmetric hopping of charge carriers is happening around the charge localization temperature and we observed a partition to the MD coupling by T_{CL} as positive and negative. MD is positive below T_{CL} whereas it is negative above T_{CL}. The tanδ also changes with the applied magnetic field as ε and the MDL follows the same trend of MD. A combination of MR and the M-W effect are reported to be responsible for strong MD effects in material where a magnetoelectric coupling is absent [107]. In the present work, we observed a positive MD and a negative MDL

below T_{CL}. Such effect is reported to be originating from the interaction of a core grain dominated MR with the M-W polarization [107]. A negative MD and positive MDL are observed above T_{CL} which is reported to be originating from the influence of interface dominated MR and M-W effect [107]. Zhang *et al.* reported positive and negative MD developed from the M-W effect as per the annealing temperatures in La_2NiMnO_6 films [69].

A simultaneous occurrence of both the positive and negative MD effects with a colossal value make the material different from other perovskites reported. Simultaneous occurrences of positive and negative MD have been previously reported with small coupling value in comparatively large magnetic fields [74, 103, 104].

The careful analysis on the magnetic, transport and magnetotransport properties presented in this section give an insight into the physical origins of the positive and negative MD effects at multiple temperature regions in La_2FeMnO_6. The lack of structural and magnetic symmetry and the charge localization along with the spin glass property and dipolar relaxation are the fundamental reasons behind the origin of MD coupling in La_2FeMnO_6 [13, 103, 105, 106, 108, 109].

3-2.4 Conclusion

In summary, the perovskite La_2FeMnO_6 is identified to possess both the positive and negative MD coupling in a small applied field of 5 kOe, where the intrinsic structural, magnetic, and dielectric correlations contribute to the MD effects. Charge localization is observed in the low temperature distorted phase of La_2FeMnO_6 around T_{CL}~133 K. The material exhibits spin glass property, which is

confirmed by ac susceptibility, ZFC memory and aging measurements. The material La_2FeMnO_6 possesses double dielectric relaxations wherein both the relaxations follow Arrhenius law. The large MD coupling values of +4.5% at ~80 K, +45% at ~122 K, -18% at ~147 K, and -6.8% at ~284 K is established through a cooperative effect from charge localization phenomenon, spin glass property, and dielectric relaxation behavior.

3-2.5 References

[1] K.I. Kobayashi, T. Kimura, H. Sawada, K. Terakura, Y. Tokura, Nature, 395 (1998) 677-680.

[2] P. Baettig, C. Ederer, N.A. Spaldin, Physical Review B, 72 (2005) 214105.

[3] M.T. Anderson, K.B. Greenwood, G.A. Taylor, K.R. Poeppelmeier, Progress in Solid State Chemistry, 22 (1993) 197-233.

[4] L. Balcells, J. Navarro, M. Bibes, A. Roig, B. Martínez, J. Fontcuberta, Applied Physics Letters, 78 (2001) 781-783.

[5] R. von Helmolt, J. Wecker, B. Holzapfel, L. Schultz, K. Samwer, Physical Review Letters, 71 (1993) 2331-2333.

[6] M.-R. Li, M. Retuerto, Z. Deng, P.W. Stephens, M. Croft, Q. Huang, H. Wu, X. Deng, G. Kotliar, J. Sánchez-Benítez, J. Hadermann, D. Walker, M. Greenblatt, Angewandte Chemie, 127 (2015) 12237-12241.

[7] P. Neenu Lekshmi, M. Vasundhara, M.R. Varma, K.G. Suresh, M. Valant, Physica B: Condensed Matter, 448 (2014) 285-289.

[8] Y. Mao, J. Parsons, J.S. McCloy, Nanoscale, 5 (2013) 4720-4728.

[9] R. Yadav, H.S. Nair, A. Kumar, S. Adiga, H.L. Bhat, S.M. Yusuf, S. Elizabeth, Journal of Applied Physics, 117 (2015) 093903.

[10] P. Barrozo, J. Albino Aguiar, Journal of Applied Physics, 113 (2013) 17E309.

[11] J.M.D. Coey, M. Viret, L. Ranno, K. Ounadjela, Physical Review Letters, 75 (1995) 3910-3913.

[12] J.M.D. Coey, M. Viret, S. von Molnár, Advances in Physics, 48 (1999) 167-293.

[13] D. Choudhury, P. Mandal, R. Mathieu, A. Hazarika, S. Rajan, A. Sundaresan, U.V. Waghmare, R. Knut, O. Karis, P. Nordblad, D.D. Sarma, Physical Review Letters, 108 (2012) 127201.

[14] Y. Guo, L. Shi, S. Zhou, J. Zhao, W. Liu, Applied Physics Letters, 102 (2013) 222401.

[15] J.W. Seo, E.E. Fullerton, F. Nolting, A. Scholl, J. Fompeyrine, J.P. Locquet, Journal of Physics: Condensed Matter, 20 (2008) 264014.

[16] P. Mondal, D. Bhattacharya, P. Choudhury, P. Mandal, Physical Review B, 76 (2007) 172403.

[17] J. Kanamori, Journal of Physics and Chemistry of Solids, 10 (1959) 87-98.

[18] P. Ganguly, Bulletin of Materials Science, 3 (1981) 255-260.

[19] Y. Wu, Z. Yu, S. Liu, Journal of Solid State Chemistry, 112 (1994) 157-160.

[20] B. Toby, Journal of Applied Crystallography, 34 (2001) 210-213.

[21] CrystalMaker Software Ltd, Oxford, England.

[22] J. Blomquist, U. Helgeson, L.C. Moberg, B. Folkesson, R. Larsson, Inorganica Chimica Acta, 69 (1983) 17-23.

[23] J.C. Carver, G.K. Schweitzer, T.A. Carlson, The Journal of Chemical Physics, 57 (1972) 973-982.

[24] Y. Qian, H. Wu, E. Kan, J. Lu, R. Lu, Y. Liu, W. Tan, C. Xiao, K. Deng, Journal of Applied Physics, 114 (2013) 063713.

[25] O.F. de Lima, J.A.H. Coaquira, R.L. de Almeida, L.B. de Carvalho, S.K. Malik, Journal of Applied Physics, 105 (2009) 013907.

[26] Z.-X. Wei, Y. Wang, J.-P. Liu, C.-M. Xiao, W.-W. Zeng, Materials Chemistry and Physics, 136 (2012) 755-761.

[27] D.V. Karpinsky, I.O. Troyanchuk, V.V. Sikolenko, Journal of Physics: Condensed Matter, 19 (2007) 036220.

[28] K. De, M. Thakur, A. Manna, S. Giri, Journal of Applied Physics, 99 (2006) 013908.

[29] K. De, R. Ray, R. Narayan Panda, S. Giri, H. Nakamura, T. Kohara, Journal of Magnetism and Magnetic Materials, 288 (2005) 339-346.

[30] S.D. Bhame, V.L.J. Joly, P.A. Joy, Physical Review B, 72 (2005) 054426.

[31] P. Barrozo, N. O. Moreno, J. A. Aguiar, Advanced Materials Research, 975 (2014) 122-127.

[32] K. Ueda, H. Tabata, T. Kawai, Physical Review B, 60 (1999) R12561-R12564.

[33] K. Ueda, Y. Muraoka, H. Tabata, T. Kawai, Applied Physics Letters, 78 (2001) 512-514.

[34] X.-D. Zhou, L.R. Pederson, Q. Cai, J. Yang, B.J. Scarfino, M. Kim, W.B. Yelon, W.J. James, H.U. Anderson, C. Wang, Journal of Applied Physics, 99 (2006) 08M918.

[35] K. Yoshimatsu, K. Nogami, K. Watarai, K. Horiba, H. Kumigashira, O. Sakata, T. Oshima, A. Ohtomo, Physical Review B, 91 (2015) 054421.

[36] S.K. Giri, S.M. Yusuf, M.D. Mukadam, T.K. Nath, Journal of Alloys and Compounds, 591 (2014) 181-187.

[37] A.K. Pramanik, A. Banerjee, Physical Review B, 81 (2010) 024431.

[38] W. Jiang, X. Zhou, G. Williams, Y. Mukovskii, K. Glazyrin, Physical Review B, 77 (2008) 064424.

[39] P. Tong, B. Kim, D. Kwon, T. Qian, S.-I. Lee, S.W. Cheong, B.G. Kim, Physical Review B, 77 (2008) 184432.

[40] H.S. Nair, D. Swain, H. N., S. Adiga, C. Narayana, S. Elzabeth, Journal of Applied Physics, 110 (2011) 123919.

[41] A. Shahee, K. Singh, R.J. Choudhary, N.P. Lalla, physica status solidi (b), 252 (2015) 1832-1838.

[42] S. Zhou, Y. Guo, J. Zhao, L. He, C. Wang, L. Shi, The Journal of Physical Chemistry C, 115 (2011) 11500-11506.

[43] A. Ślebarski, J. Goraus, M. Fijałkowski, Physical Review B, 84 (2011) 075154.

[44] S. Guo, D.P. Young, R.T. Macaluso, D.A. Browne, N.L. Henderson, J.Y. Chan, L.L. Henry, J.F. DiTusa, Physical Review Letters, 100 (2008) 017209.

[45] R.B. Griffiths, Physical Review Letters, 23 (1969) 17-19.

[46] A. Moreo, M. Mayr, A. Feiguin, S. Yunoki, E. Dagotto, Physical Review Letters, 84 (2000) 5568-5571.

[47] V. Markovich, R. Puzniak, I. Fita, A. Wisniewski, D. Mogilyansky, B. Dolgin, G. Gorodetsky, G. Jung, Journal of Applied Physics, 113 (2013) 233911.

[48] R.-F. Yang, Y. Sun, W. He, Q.-A. Li, Z.-H. Cheng, Applied Physics Letters, 90 (2007) 032502.

[49] X.J. Liu, Z.Q. Li, A. Yu, M.L. Liu, W.R. Li, B.L. Li, P. Wu, H.L. Bai, E.Y. Jiang, Journal of Magnetism and Magnetic Materials, 313 (2007) 354-360.

[50] S. Zhou, Y. Guo, J. Zhao, L. He, L. Shi, The Journal of Physical Chemistry C, 115 (2011) 1535-1540.

[51] C.L. Lu, K.F. Wang, S. Dong, J.G. Wan, J.-M. Liu, Z.F. Ren, Journal of Applied Physics, 103 (2008) 07F714.

[52] S. Zhou, L. Shi, H. Yang, J. Zhao, Applied Physics Letters, 91 (2007) 172505.

[53] J. Deisenhofer, D. Braak, H.A. Krug von Nidda, J. Hemberger, R.M. Eremina, V.A. Ivanshin, A.M. Balbashov, G. Jug, A. Loidl, T. Kimura, Y. Tokura, Physical Review Letters, 95 (2005) 257202.

[54] J.P. Velev, S.S. Jaswal, E.Y. Tsymbal, Philosophical Transactions of the Royal Society of London A: Mathematical, Physical and Engineering Sciences, 369 (2011) 3069-3097.

[55] E. Dagotto, Science, 309 (2005) 257-262.

[56] J. Varignon, N.C. Bristowe, E. Bousquet, P. Ghosez, Scientific Reports, 5 (2015) 15364.

[57] P. Zubko, S. Gariglio, M. Gabay, P. Ghosez, J.-M. Triscone, Annual Review of Condensed Matter Physics, 2 (2011) 141-165.

[58] A.P. Ramirez, Journal of Physics: Condensed Matter, 9 (1997) 8171.

[59] Q. Jiang, S.J. Gong, The European Physical Journal B - Condensed Matter and Complex Systems, 43 (2005) 333-338.

[60] G. Lawes, A.P. Ramirez, C.M. Varma, M.A. Subramanian, Physical Review Letters, 91 (2003) 257208.

[61] P. Padhan, H.Z. Guo, P. LeClair, A. Gupta, Applied Physics Letters, 92 (2008) 022909.

[62] J.K. Murthy, K.D. Chandrasekhar, S. Murugavel, A. Venimadhav, Journal of Materials Chemistry C, 3 (2015) 836-843.

[63] P.N. Lekshmi, G.R. Raji, M. Vasundhara, M.R. Varma, S.S. Pillai, M. Valant, Journal of Materials Chemistry C, 1 (2013) 6565-6574.

[64] S.H. Oh, H.Y. Choi, J.Y. Moon, M.K. Kim, Y. Jo, N. Lee, Y.J. Choi, Journal of Physics D: Applied Physics, 48 (2015) 445001.

[65] M.A. Subramanian, T. He, J. Chen, N.S. Rogado, T.G. Calvarese, A.W. Sleight, Advanced Materials, 18 (2006) 1737-1739.

[66] P. Mandal, V.S. Bhadram, Y. Sundarayya, C. Narayana, A. Sundaresan, C.N.R. Rao, Physical Review Letters, 107 (2011) 137202.

[67] N.S. Rogado, J. Li, A.W. Sleight, M.A. Subramanian, Advanced Materials, 17 (2005) 2225-2227.

[68] G.M. Md, G. Arijit, J. Sannigrahi, B.K. Chaudhuri, Journal of Physics: Condensed Matter, 24 (2012) 295902.

[69] Z. Zhang, H. Jian, X. Tang, J. Yang, X. Zhu, Y. Sun, Dalton Transactions, 41 (2012) 11836-11840.

[70] C.-H. Yang, S.-H. Lee, T.Y. Koo, Y.H. Jeong, Physical Review B, 75 (2007) 140104.

[71] K.D. Chandrasekhar, A.K. Das, A. Venimadhav, Journal of Physics: Condensed Matter, 24 (2012) 376003.

[72] K.D. Chandrasekhar, A.K. Das, C. Mitra, A. Venimadhav, Journal of Physics: Condensed Matter, 24 (2012) 495901.

[73] A. Venimadhav, D. Chandrasekar, J. Krishna Murthy, Applied Nanoscience, 3 (2013) 25-28.

[74] N. Imamura, M. Karppinen, T. Motohashi, D. Fu, M. Itoh, H. Yamauchi, Journal of the American Chemical Society, 130 (2008) 14948-14949.

[75] J. Pezhumkattil Palakkal, P.N. Lekshmi, S. Thomas, K.G. Suresh, M.R. Varma, RSC Advances, 5 (2015) 105531-105536.

[76] E. Paparazzo, Journal of Electron Spectroscopy and Related Phenomena, 43 (1987) 97-112.

[77] D. Brion, Applications of Surface Science, 5 (1980) 133-152.

[78] R.O. Ansell, T. Dickinson, A.F. Povey, Corrosion Science, 18 (1978) 245-256.

[79] B.R. Strohmeier, D.M. Hercules, The Journal of Physical Chemistry, 88 (1984) 4922-4929.

[80] M.A. Peña, J.L.G. Fierro, Chemical Reviews, 101 (2001) 1981-2018.

[81] C.N.R. Rao, B. Raveau, Colossal Magnetoresistance, Charge Ordering and Related Properties of Manganese Oxides, World Scientific, 1998.

[82] J. Tao, J.M. Zuo, Physical Review B, 69 (2004) 180404.

[83] S.V. Streltsov, D.I. Khomskii, Physical Review B, 89 (2014) 201115.

[84] R. Schmidt, Physical Review B, 77 (2008) 205101.

[85] D. Indu, A. Das, A.K. Nigam, Journal of Physics: Condensed Matter, 21 (2009) 386002.

[86] N.F. Mott, Metal-Insulator Transitions, Taylor and Francis, London 1990.

[87] R. Schmidt, A. Basu, A.W. Brinkman, Physical Review B, 72 (2005) 115101.

[88] R.K. Zheng, A.N. Tang, Y. Yang, W. Wang, G. Li, X.G. Li, H.C. Ku, Journal of Applied Physics, 94 (2003) 514-518.

[89] H.D. Yang, H.L. Huang, P.L. Ho, W.L. Huang, C.W. Huang, S. Mollah, S.J. Liu, J.Y. Lin, Physica B: Condensed Matter, 329–333, Part 2 (2003) 801-802.

[90] E.P. Warren, Q. Yundi, P. Victor, Journal of Physics: Condensed Matter, 26 (2014) 274203.

[91] E.J.W. VERWEY, Nature, (1939).

[92] G. Parkin, Journal of Chemical Education, 83 (2006) 791.

[93] A. Amaricci, A. Camjayi, K. Haule, G. Kotliar, D. Tanasković, V. Dobrosavljević, Physical Review B, 82 (2010) 155102.

[94] A.P. Roberts, Y. Cui, K.L. Verosub, Journal of Geophysical Research: Solid Earth, 100 (1995) 17909-17924.

[95] Y. Tian, S. Shen, J. Cong, L. Yan, S. Wang, Y. Sun, Journal of the American Chemical Society, 138 (2016) 782-785.

[96] M. Bałanda, H.-A.K. von Nidda, M. Heinrich, A. Loidl, Dynamic Susceptibility of Magnetic Systems, in: W. Haase, S. Wróbel (Eds.) Relaxation Phenomena: Liquid Crystals, Magnetic Systems, Polymers, High-Tc Superconductors, Metallic Glasses, Springer Berlin Heidelberg, Berlin, Heidelberg, 2003, pp. 89-135.

[97] N. Khan, P. Mandal, D. Prabhakaran, Physical Review B, 90 (2014) 024421.

[98] T. Chakrabarty, A.V. Mahajan, S. Kundu, Journal of Physics: Condensed Matter, 26 (2014) 405601.

[99] S. Sarkar, A. Mondal, K. Dey, R. Ray, RSC Advances, 5 (2015) 81260-81265.

[100] D. Chu, G.G. Kenning, R. Orbach, Physical Review Letters, 72 (1994) 3270-3273.

[101] H. Khurshid, P. Lampen-Kelley, Ò. Iglesias, J. Alonso, M.-H. Phan, C.-J. Sun, M.-L. Saboungi, H. Srikanth, 5 (2015) 15054.

[102] J.M. Herbert, Ceramic Dielectrics and Capacitors, CRC Press, 1985.

[103] L.Y. Wang, Q. Li, Y.Y. Gong, D.H. Wang, Q.Q. Cao, Y.W. Du, Journal of the American Ceramic Society, 97 (2014) 2024-2026.

[104] W. Yi, A.J. Princep, Y. Guo, R.D. Johnson, D. Khalyavin, P. Manuel, A. Senyshyn, I.A. Presniakov, A.V. Sobolev, Y. Matsushita, M. Tanaka, A.A. Belik, A.T. Boothroyd, Inorganic Chemistry, 54 (2015) 8012-8021.

[105] F. Schrettle, P. Lunkenheimer, J. Hemberger, V.Y. Ivanov, A.A. Mukhin, A.M. Balbashov, A. Loidl, Physical Review Letters, 102 (2009) 207208.

[106] H.J. Xiang, M.H. Whangbo, Physical Review Letters, 98 (2007) 246403.

[107] G. Catalan, Applied Physics Letters, 88 (2006) 102902.

[108] X. Wang, Y. Chai, L. Zhou, H. Cao, C.-d. Cruz, J. Yang, J. Dai, Y. Yin, Z. Yuan, S. Zhang, R. Yu, M. Azuma, Y. Shimakawa, H. Zhang, S. Dong, Y. Sun, C. Jin, Y. Long, Physical Review Letters, 115 (2015) 087601.

[109] M.G. Masud, A. Ghosh, B.K. Chaudhuri, K. Hsiao, H.D. Yang, Journal of Applied Physics, 110 (2011) 113719.

Chapter 4

Unusual magnetodielectric effects in frustrated ferromagnetic perovskite La_2CuMnO_6

A dynamic (Arrhenius to Arrhenius) crossover at T_C is observed in the dielectric relaxation of disordered double perovskite La_2CuMnO_6. The external magnetic field alters the relaxation parameters in the vicinity of crossover and induces an unusual behavior in the magnetodielectric coupling around T_C with a large magnetodielectric coupling.

4.1 Introduction

Varying the dielectric property of a material upon the application of an external magnetic field has potential applications in spintronics and MD based devices like magnetic read heads, sensors, nonvolatile memories, etc. [1]. Strongly correlated electronic systems create competing magnetic and electronic phases along with an interplay between the spin and charge order. Such systems exhibit a coupling between the magnetic order and the charge order mostly during a magnetic or electric transition [2-10]. MD coupling is typically found around a paramagnetic to ferromagnetic transition where the charges are localized to possess insulating or semiconducting behavior [3-10]. A coupling between magnetism and dielectric behavior in perovskite can be induced either by an influence of magnetic field on the dipolar relaxation or by an interaction of grain/grain boundary dominated MR with Maxwell-Wagner (M-W) effect associated with the interfacial polarization [5, 8, 9, 11-14].

Recently, ferromagnetism with Griffiths-like phase and magnetoresistance were observed in double perovskite La_2CuMnO_6 [15, 16]. Though the MD properties of La_2NiMnO_6 and La_2CoMnO_6 have been widely studied for last few years; MD of La_2CuMnO_6 is not yet explored [8, 10-12, 14]. Both positive and negative MD coupling occurs in materials at certain temperature ranges as a result of the magnetic field dependence of various spin/lattice relaxations. Usually, the maximum value of MD coupling (MD_{Max}) decreases and the temperature corresponding to MD_{Max} increases upon increasing the frequency [12]. The dielectric relaxation is occurring in perovskite material as a result of hopping of the charge carriers between spatially fluctuating lattice potentials [14, 17]. The main

types of dielectric relaxation in materials are Maxwell-Wagner relaxation and Debye relaxation [18, 19]. A significant frequency dependency in the dielectric response at low frequencies is resulting from the accumulation of charges due to Maxwell-Wagner (M-W) effects at the inner dielectric boundary or the external electrode-sample interface [20]. An asymmetric hopping of charge carriers causes the non-interacting dipoles in the lattice to relax with an alternating external electric field which is the Debye-type relaxation [14].

A dynamic crossover in the neighborhood of a transition point was observed for relaxation phenomenon in many polymers, supercooled liquids in bulk such as water, glycerol, hydrated proteins, etc. [21-25]. A crossover from relaxor to ferroelectric behavior has also been extensively examined for many perovskite systems with multifunctional properties [26, 27]. A dynamic Arrhenius to Arrhenius transition in relaxation time around T_C is observed for perovskite systems like La_2CoMnO_6, Y_2NiMnO_6, Y_2FeCrO_6, etc. due to the differences in the alignment of spins below and above T_C [19, 28, 29].

In the present investigation, we have analyzed the magnetic and dielectric behavior of La_2CuMnO_6 in detail. A dynamic crossover in the Arrhenius relaxation around the observed T_C is identified for the material which causes an unusual trend in the variation of MD coupling around the crossover. The role of the frustrated magnetic structure and the dielectric relaxation for the occurrence of this unusual trend is discussed in this chapter.

4.2 Experimental

The DP La_2CuMnO_6 was prepared by citrate-gel combustion method. A detailed synthesis method was explained in chapter 3 [30]. The sintered pellets were checked for phase purity by X-ray diffraction (XRD) studies using PANalytical X'Pert Pro Powder X-ray diffractometer with a Ni-filtered Cu Kα radiation (λ=1.5405 Å). GSAS EXPGUI [31] software was used to perform the Rietveld structural refinement of the obtained XRD pattern. A part of the crystallographic structure was framed by the CrystalMaker® software. JEOL JSM 5610 scanning electron microscope (SEM) was used to image a microstructure of the sintered pellets. X-ray photoelectron spectroscopy (XPS) is performed by Thermo Scientific X-ray photoelectron spectrometer. The obtained Cu and Mn spectra were fitted by the XPS peak Fit software. The magnetic moment was measured in a temperature range 2-300 K and a magnetic field range -90 kOe to +90 kOe by the Quantum Design Vibrating Sample Magnetometer option for the Physical Property Measurement System (PPMS). AC susceptibility for the temperature ranges 2-300 K for different frequencies was measured by ACMS option attached to PPMS. DC resistivity measurements for 60-300 K were done by Quantum Design Electrical Transport option for the PPMS. The specific heat in 5-300 K temperature ranges was measured by using the Quantum Design Heat Capacity option for the PPMS. An LCR meter (Agilent E4980A) with a closed cycle Cryocooler (ARS-2HV) was used for dielectric measurements in 30-300 K range at various frequencies. Magnetodielectric coupling was calculated by using the dielectric data with and without a magnetic field of 5 kOe.

4.3 Results and Discussion

4.3.1 Structural properties

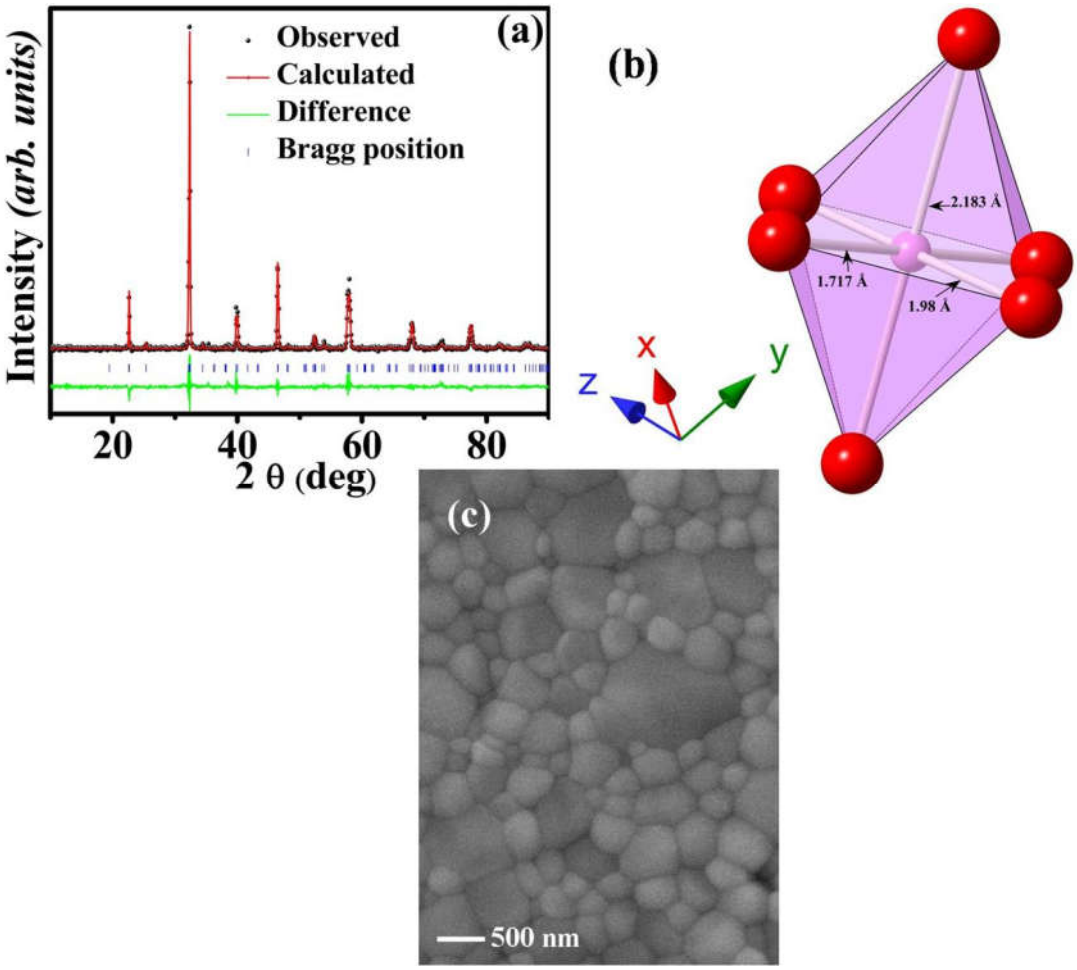

Figure 4.1 (a) XRD pattern of La_2CuMnO_6 after Rietveld refinement. (b) Distorted octahedron of La_2CuMnO_6. (c) SEM image, showing the ceramic microstructure.

The Rietveld refinement of the obtained XRD pattern (figure 4.1 (a)) gives a centric, primitive, orthorhombic *Pbnm* crystal structure with Laue symmetry *mmm*. The unit cell parameters obtained from the structural refinements are a=5.5149(3) Å, b=5.4706(3) Å, c=7.7543(4) Å, and α=β=γ=90º. The Rietveld fitting factors are $_WR_P$=13%, R_P=10%, and χ^2=1.19. The two types of <Cu/Mn-O-Cu/Mn> bond

angles are 156.46º and 169.55º for each type of oxygen (O1 and O2). The Cu/MnO_6 octahedron is depicted in figure 4.1 (b). SEM image of the sintered pellets taken at 15 kV is shown in figure 4.1 (c). The grain size distribution can be described as bimodal with a mean size ~200 nm and ~750 nm for each population.

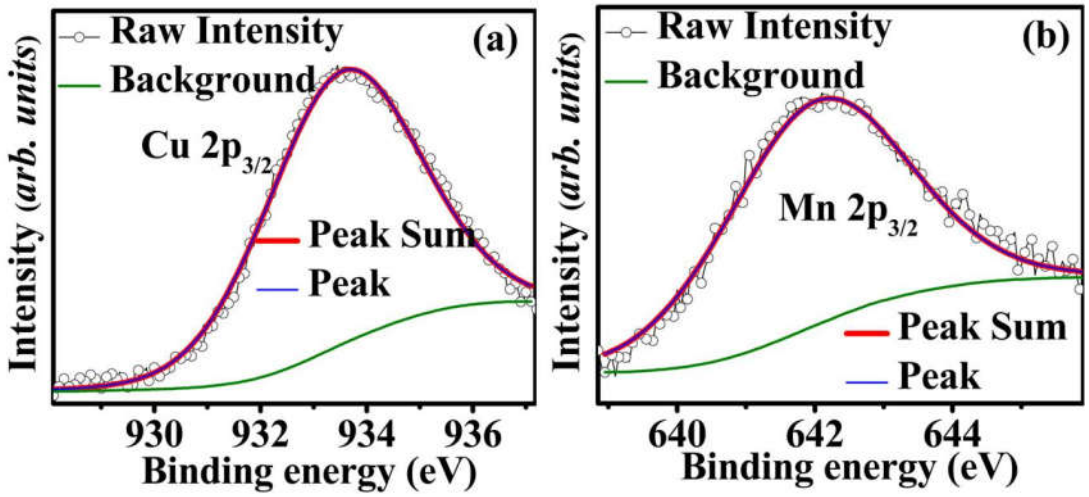

Figure 4.2 XPS spectra of (a) Cu $2p_{3/2}$ and (b) Mn $2p_{3/2}$ in La_2CuMnO_6 along with the fitted curves.

The XPS spectra for the Cu 2p and Mn 2p of La_2CuMnO_6 were corrected for the shift in binding energies by taking C 1s as reference energy. The fitting of the curve gives a single peak at 933.52 eV for Cu $2p_{3/2}$ (figure 4.2 (a)) and 642.00 eV for Mn $2p_{3/2}$ (figure 4.2 (b)). This confirms the presence of Cu^{+2} [32] and Mn^{+4} cations [33], which support the studies by Electron Energy Loss Spectroscopy [15]. The presence of Cu^{2+} ion expects a strong Jahn-Teller effect and distortion due to the unevenly occupied e_g orbitals. The three vector lengths 1.717 Å, 1.980 Å, and 2.183 Å for <Cu/Mn-O> bonds illustrate the distorted Cu/MnO_6 octahedron as shown in figure 4.1 (b). The calculation of the J-T distortion by the equation [2]

$\Delta d = \frac{1}{6}\sum_1^6 \left[\left(d_n - \langle d\rangle\right)/\langle d\rangle\right]^2$ (where d_n is the average of the nth Cu/Mn-O bond length and <d> is the average for all the Cu/Mn-O bond lengths), gives a value of 9.47x10^{-3} that is large compared to that of $LaMnO_3$, due to the large distortion associated with J-T Cu^{2+} ion. The angle distortions $\left(\langle\omega\rangle = 180^\circ - \langle\theta\rangle\right)$ are $\langle\omega_1\rangle$ =23.54º and $\langle\omega_2\rangle$ =10.45º with an average $\langle\omega\rangle$ =16.99º.

4.3.2 DC and AC Magnetic Properties

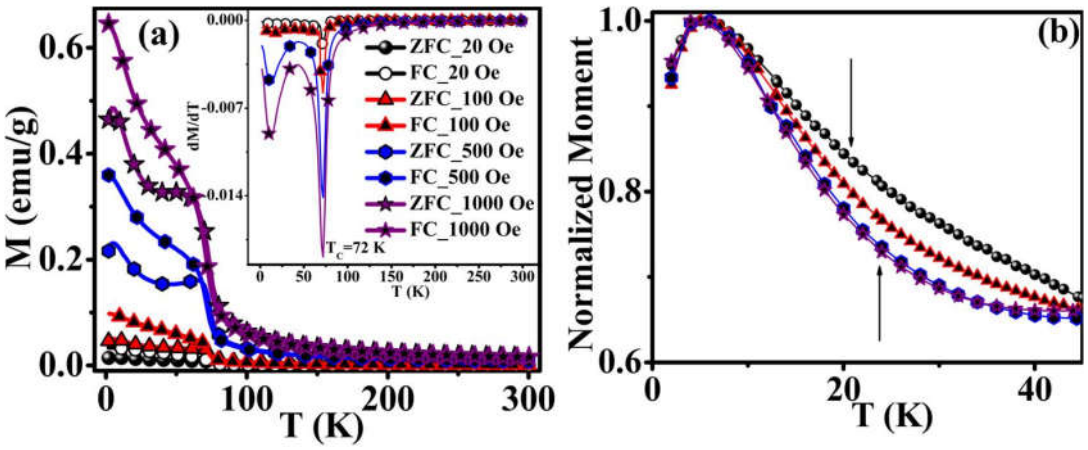

Figure 4.3 (a) ZFC and FC thermomagnetic curves at various fields. Inset is showing the dM/dT vs. T plot. (b) ZFC curves for low-temperature region showing AFM interactions.

The zero field cooled (ZFC), and field cooled (FC) magnetizations as a function of temperature (MT) for magnetic fields 20 Oe, 100 Oe, 500 Oe, and 1000 Oe are shown in figure 4.3 (a). The dM/dT vs. T plot (inset of figure 4.3 (a)) shows two magnetic transitions at 13 K and T_C=72 K. The bifurcation in the FC and ZFC curves gives an insight into the frustrated magnetic behavior of the system. The magnetism in the material is a combination of antiferromagnetic (AFM) and ferromagnetic (FM) interactions [15]. To account for the lower temperature

AFM+FM interactions, the ZFC curves with normalized magnetic moments for 2-45 K with 20 Oe, 100 Oe, 500 Oe, and 1000 Oe are shown in figure 4.3 (b). It is clearly seen that the peak position at 5 K is not altering with an increase in the magnetic field which can be ascertained to an AFM ordering temperature (T_N). The dip in the ZFC curve, appearing in between T_N and T_C, becomes pronounced as the field increases from 20 Oe to 1000 Oe, which is ascribed to a diminishing of the magnetic moment after T_N. The dip is not appearing in the FC curve since the FM phase got dominated over the AFM phase by the application of field during the cooling.

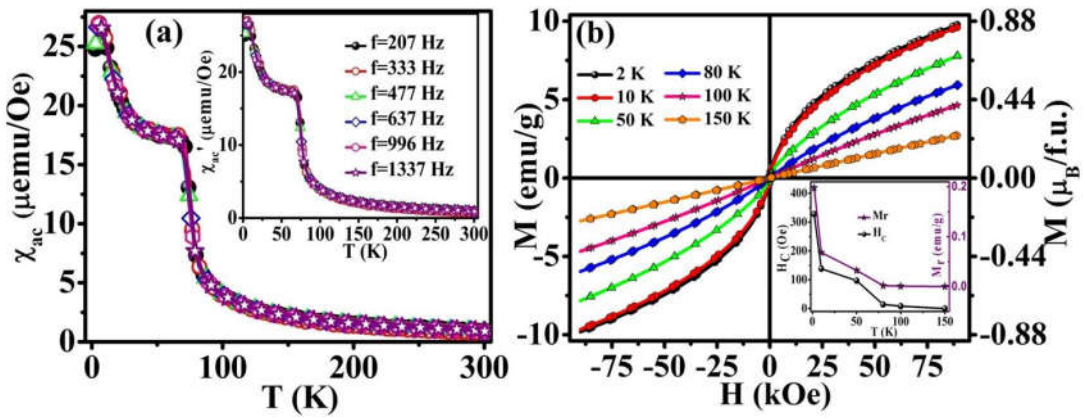

Figure 4.4 (a) Temperature dependence of AC susceptibility (χ_{ac}) and inset showing real part of AC susceptibility (χ_{ac}'') at various frequencies. (b) Isothermal magnetization curves recorded at different temperatures. Inset depicting the variation of coercivity (H_C) and remanence (M_r) with temperature.

For further distinction of the AFM+FM interactions from the spin glass behavior, the AC susceptibility (χ_{ac}) measurements of La_2CuMnO_6 are carried out for temperatures 2-300 K at different frequencies. χ_{ac} and real part of χ_{ac} (χ_{ac}') are shown in figure 4.4 (a) and inset of figure 4.4 (a), respectively. There is no frequency dependent variation in either χ_{ac} or χ_{ac}', which proves that the observed

bifurcation in the FC/ZFC curves is originating from the AFM+FM clusters and not from any spin glass type interactions.

The hysteresis (MH) loops at 2 K, 10 K, 50 K, 80 K, 100 K, and 150 K are non-saturating even at 90 kOe as shown in figure 4.4 (b), due to the presence of competing magnetic interactions. The obtained coercivity and remanence are shown in the inset of figure 4.4 (b). The MH above T_C at 80 K and 100 K are showing small coercivity indicating the presence of FM clusters above T_C while MH at 150 K is linear showing that the system is completely PM. The inverse DC susceptibility (χ^{-1}) derived from FC curves for external fields 20 Oe, 100 Oe, 500 Oe, 1000 Oe, and 10 kOe are shown in figure 4.5 (a). A fit to Curie-Weiss (CW) law $\frac{1}{\chi} = \frac{T - \Theta}{C_W}$ for the FC at 100 Oe is shown in the inset of figure 4.5 (a). The χ^{-1} shows a sharp deviation (as a downturn) from the CW fit below a particular temperature T^*=115 K. The downturn is gradually reduced with increasing field as shown in figure 4.5 (a) which is a characteristic feature of a Griffiths-like phase (GP) with short-range ferromagnetic correlations above T_C [30, 34-45]. GP is a diluted ising FM [35]. A Griffiths singularity is previously reported in the material with T*=81 K [16]. The CW fit in the paramagnetic (PM) region yields an effective magnetic moment, μ_{eff} =4.12 μ_B / f.u. For spin only interaction, La_2CuMnO_6 with Cu^{2+} and Mn^{4+} cations has a theoretical effective moment $\left[\mu_{eff} = g\sqrt{s(s+1)}\mu_B\right]$ 4.24 μ_B / f.u. which is very close to the experimentally observed one. The experimentally observed μ_{eff} ruled out the possibility of a spin-orbit interaction in the material in which the theoretically expected μ_{eff} is 7.52 μ_B / f.u. The Cu^{2+} (t_{2g}^6 e_g^3) and the Mn^{4+} (t_{2g}^3 e_g^0) superexchange interaction would be FM. The presence of antisite defect and interplanar interactions

would explain the presence of AFM contribution at low temperatures. Even though the MH hysteresis loops are observed above T_C, the linear fit to the high field region of the M^2 vs. H/M plot above T_C has a negative M^2-axis intercept, as shown in the inset of figure 4.5 (b), which shows on the absence of a spontaneous magnetization above T_C. This further proves the presence of GP in the material.

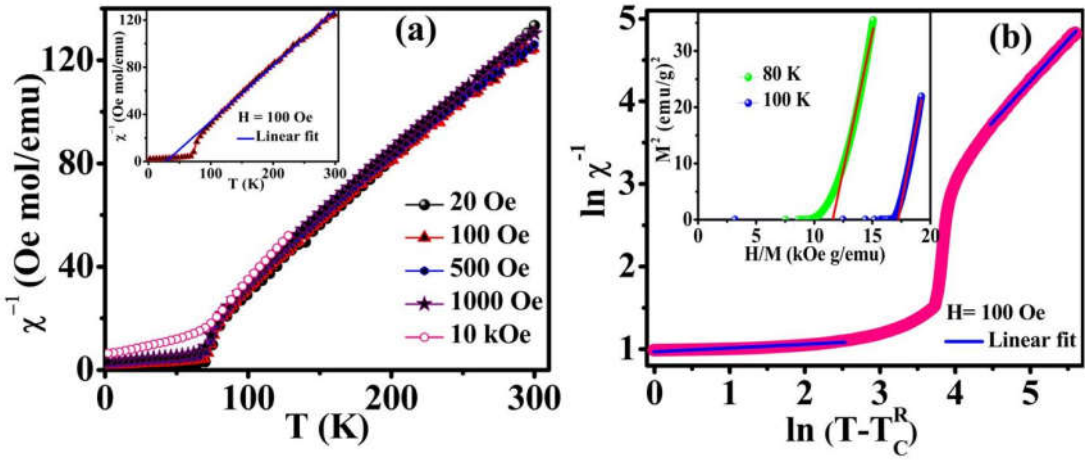

Figure 4.5 (a) Temperature dependence of inverse dc susceptibility (FC) at various fields. Inset of (a) showing the CW fit (solid blue line) on 1/χ (T) for FC at 100 Oe. (b) ln (χ^{-1}) vs. ln ($T-T_C^R$) at 100 Oe with the linear fit (solid blue line). Inset of (b) showing the M^2 vs. H/M plot above T_C depicting the absence of a spontaneous magnetization.

The susceptibility of GP deviates from CW law and follows the power law $\chi^{-1} \propto (T - T_C^R)^{1-\lambda}$ at low magnetic fields, provided $0 \leq \lambda < 1$ where T_C^R is the critical temperature of random FM [30, 37-45]. T_C^R is the temperature that yields a λ for PM region (λ_{PM}) close to zero above T^*. A good estimate for the λ_{PM} is obtained by assuming the T_C^R value as Θ=27 K (obtained from the CW fit). ln (χ^{-1}) vs. ln ($T-T_C^R$) plot with T_C^R=27 K is shown in figure 4.5 (b), and the linear fit gives λ_{PM}=0.003 and

λ_{GP}=0.96. The higher λ_{GP} value points the larger deviation from the CW law [41]. The magnetic structure of the material within 2-300 K temperature range can be summarized as an AFM+FM structure with transitions at T_N=5 K, and T_C=72 K. FM short-range correlations are present even above T_C. Above T^*=115 K, the material becomes fully PM.

4.3.3 Specific heat and dc resistivity

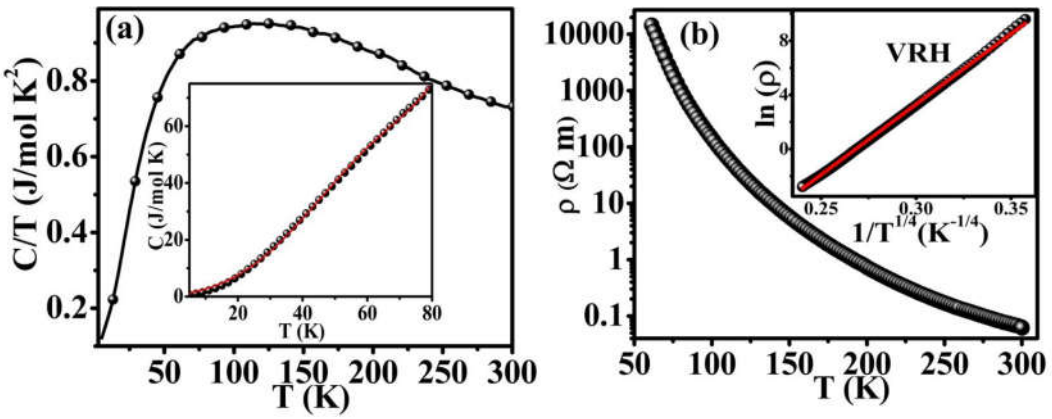

Figure 4.6 (a) Temperature dependence of specific heat (C/T) vs. T plot. The inset is showing the specific heat fit for the low-temperature region (5-80 K). (b) Temperature dependence of resistivity (ρ). Inset is showing the ln (ρ) vs. $1/T^{1/4}$ plot with the solid red line showing the linear fit for VRH model.

The specific heat (C) for a temperature range of 5-300 K is measured, and the C/T vs. T is shown in figure 4.6 (a). The low-temperature C follows the equation: $C= \gamma T+\beta_3T^3+\beta_5T^5+\beta_7T^7$ where γT is the electronic specific heat, and the other terms are lattice contributions arising from phonons [46]. The values obtained after fitting the C for 5-80 K (inset of figure 4.6 (a)) are γ=230 mJmol^{-1}K^{-2} for the linear term, β_3=0.403 mJmol^{-1}K^{-4}, β_5=-8.3x10^{-5} mJmol^{-1}K^{-6} and β_7=5.96x10^{-9} mJmol^{-1}K^{-8}. The obtained high value for the electronic linear contribution is an

indication of the coexistence of FM and a variable rage hopping (VRH) active charge localized state [47, 48]. The high value of γ is obtained for systems with a localized charges and ferromagnetic correlations like GP [30, 44, 48, 49].

The variation of resistivity (ρ) with temperature is shown in figure 4.6 (b). The ρ has a value of $67x10^{-3}$ Ω m at room temperature which increases on decreasing the temperature, pointing on a semiconducting nature. Similar to the conduction mechanism in strongly correlated systems with localized charge carrier states, ρ(T) follows Mott's VRH conduction mechanism where the charge carriers are hopping over the sites with different energies [50]. VRH is described by the equation $\rho = \rho_0 \exp\left(\frac{T_0}{T}\right)^{1/4}$, where ρ_0 is the pre-exponential factor, and T_0 is the characteristic temperature [51]. The hopping energy to nearby sites (E_a) depends on the temperature and is obtained from T_0 as $E_a = \frac{k_B}{4} T_0^{\frac{1}{4}} T^{\frac{3}{4}}$. Inset of figure 4.6 (b) shows the ln (ρ) vs. $1/T^{1/4}$ plot with the linear fit to the VRH with varying E_a (0.05 to 0.16 eV for 61 to 300 K). There is no onset of a charge ordering phenomenon, but a localized variable range hopping of charge carriers is observed.

4.3.4 Dielectric properties

The dielectric constant (ε) and dielectric loss tangent (tan δ) are measured with the temperature at various frequencies ranging from 4 kHz to 1 MHz with and without a magnetic field of 5 kOe. The ε and tan δ at 0 Oe are shown in figure 4.7 (a) and 4.7 (b) respectively. The ε is almost frequency independent with small intrinsic ε (~20) at low temperatures below ~50 K. The drop in ε below 100 K (for 4 kHz) is associated with the loss tangent resonance observed as dielectric relaxation

in tan δ. This is due to the resonance between the dipole relaxation in the material and the externally applied oscillating electric field. After this temperature, ε becomes frequency dependent and starts increasing with temperature. The sample possesses a colossal dielectric constant (~4000) at high temperatures, and the frequency dispersion becomes lower above ~200 K.

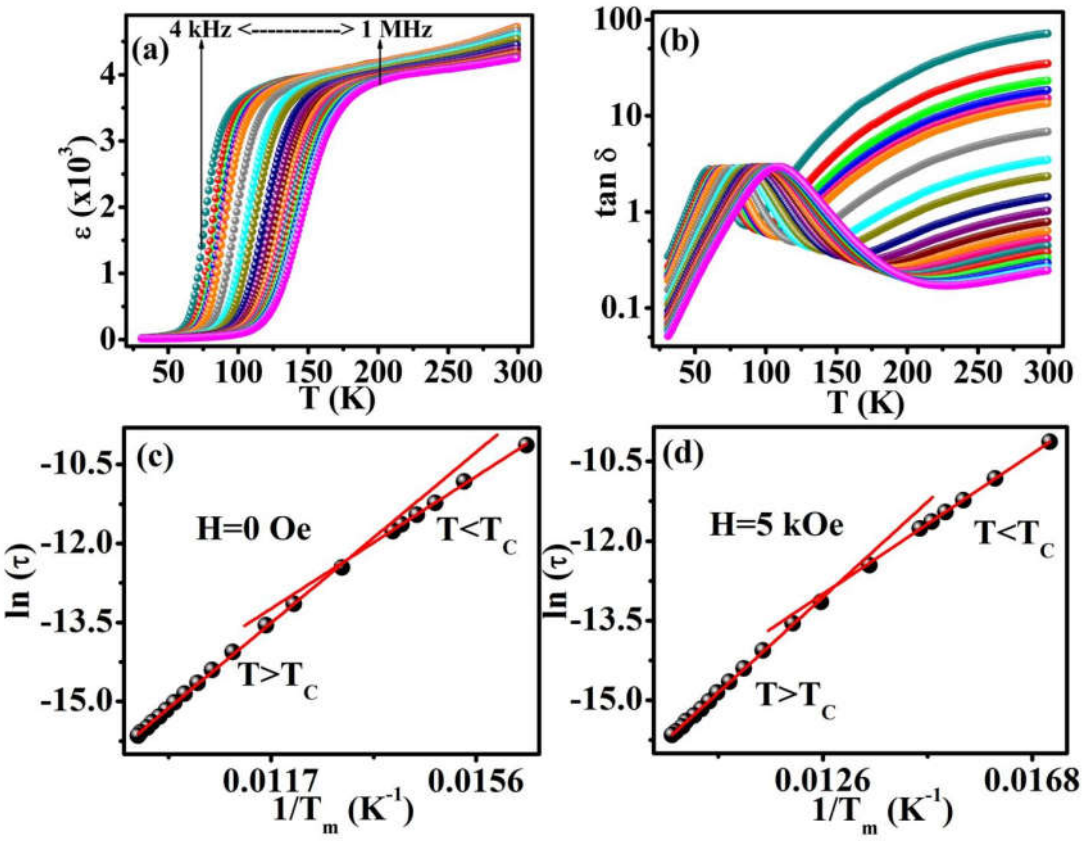

Figure 4.7 Temperature dependence of (a) dielectric constant (ε) and (b) loss tangent (tan δ) at various frequencies: 4 kHz, 8 kHz, 12 kHz, 15 kHz, 18 kHz, 20. 5 kHz, 40.9 kHz, 81.7 kHz, 122.5 kHz, 204.2 kHz, 285.8 kHz, 367.4 kHz, 449.0 kHz, 530.7 kHz, 612.3 kHz, 693.9 kHz, 775.5 kHz, 857.2 kHz, 938.8 kHz, and 1 MHz. Arrhenius fit to the relaxation time in tan δ for (c) 0 Oe and (d) 5 kOe.

The peak in tan δ at the temperature (T_m) around the T_C shows relaxation by a shift towards higher temperatures on increasing the frequency, as reported in some

perovskites [52, 53]. Figure 4.7 (c) shows the ln (τ) vs. $1/T_m$ plot where $\tau = (2\pi f)^{-1}$ is the relaxation time for each frequency (f). A linear fit to the plot by using the Arrhenius equation $\tau = \tau_0 \exp\left(\frac{E_a}{k_B T_m}\right)$ (where E_a is the activation energy, k_B is the Boltzmann constant and τ_0 is the characteristic relaxation time) yield different activation energy below and above T_C. Figure 4.7 (c) and (d) show the Arrhenius fit for relaxation time without and with a magnetic field (5 kOe), respectively. The obtained activation energy is 0.0555 eV below T_C (4 kHz to 20.5 kHz) and 0.0716 eV above T_C (40.9 kHz to 1 MHz) without a magnetic field. With the magnetic field of 5 kOe, the activation energy is 0.0542 eV below T_C and 0.0737 eV above T_C. The proximity in the activation energies for VRH and dielectric relaxation suggests a similar physical origin for the two processes. The hopping of localized charge carriers between the spatially fluctuating lattice potentials gives rise to the dielectric relaxation [17].

The linear fits (solid red line) below and above T_C are extrapolated to show the dynamic transition point where the two Arrhenius active regions meet [19, 28, 29]. This dynamic Arrhenius to Arrhenius transition point is matching with the T_C as seen in figure 4.7 (c) and (d). The spin ordered FM phase has a lower activation energy compared to that of the paramagnetic phase since the dipoles relax in the spin-ordered state more easily [19, 28]. On the application of a magnetic field, the E_a decreases for $T<T_C$. The frustrations caused by the AFM+FM interaction are suppressed to a great extent by the application of field as observed in the thermomagnetic data. Application of the magnetic field would align the spins and favors the dielectric relaxation. Above T_C, the situation is different as the E_a

increases by the application of magnetic field. La_2CuMnO_6 has a Griffiths-like phase with ferromagnetic short range correlations above T_C. As seen in figure 4.5 (a), the GP collapses in the presence of the high magnetic field. Thus, the field makes the dipoles more difficult to relax above T_C since the FM contribution is reduced by external field [19, 28, 30]. This suggests a correlation between the magnetic order and the dipole relaxation. Since the relaxations above and below T_C follow the Arrhenius law, we can consider a distribution of relaxation times around the T_C with different activation energy [54].

The complex dielectric constant (ε) can be split into a real part (ε') and imaginary part (ε") such that ε"/ε' (tan δ) stands for the phase lag between the applied ac field and induced voltage in the material. ε' and ε" are plotted as a function of temperature at various frequencies as shown in figure 4.8 (a) and 4.8 (b) respectively. ε does not vary much with frequency at high temperatures (above 200 K) whereas the ε' and ε" show large frequency dispersion. We observed small ε' with high ε" at lower frequencies whereas high frequencies offer large ε' with small ε". Thus ε is not much compliant to large frequency dispersion at high temperatures.

The large frequency dispersion in ε' and ε" appears to be originating from Maxwell-Wagner (M-W) relaxation while the relaxation peaks in tan δ around the T_C appears to be of Debye relaxation and the asymmetric peak broadening hints a contribution from non-Debye type relaxation [20].

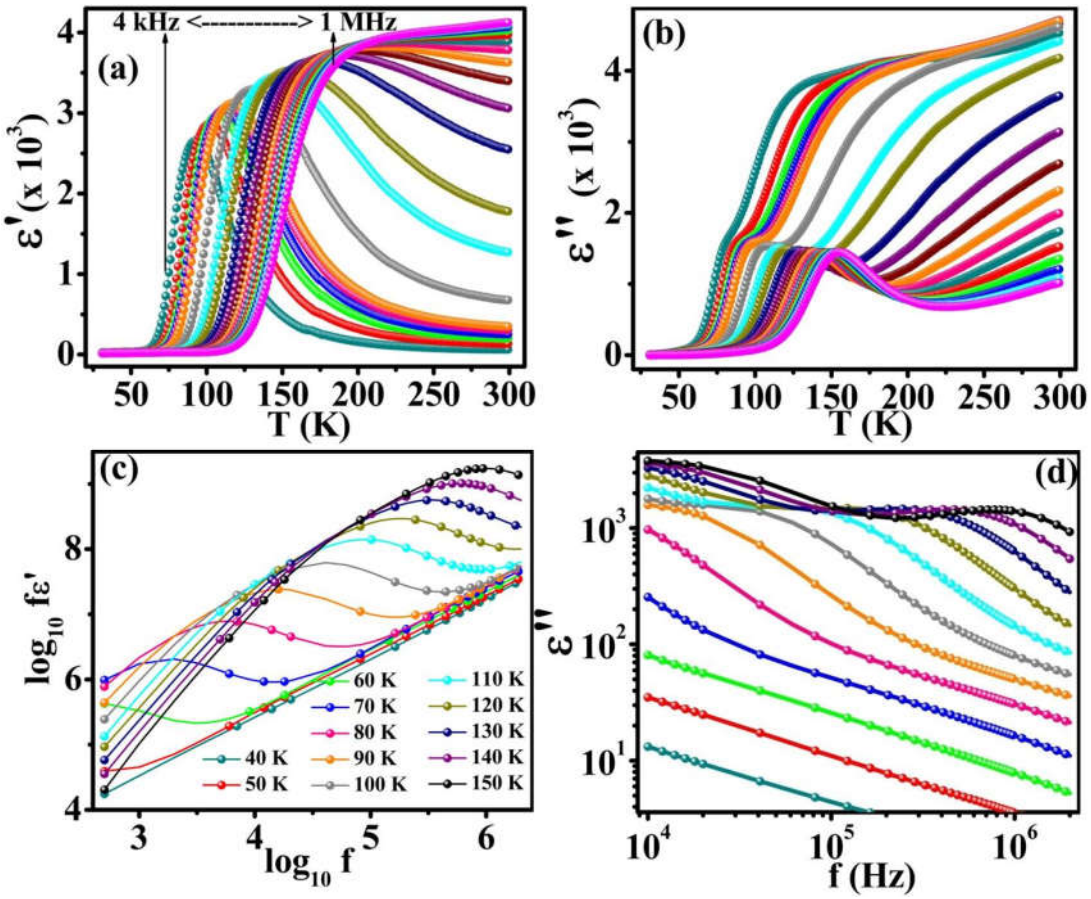

Figure 4.8 Variation of (a) real part (ε') and (b) imaginary part (ε'') of dielectric constant with temperature at various frequencies ranging from 4 kHz to 1 MHz. (c) log (ε'f) vs. log f and (d) variation of ε'' with frequency at selected temperatures.

The dielectric property as a function of frequency for the case of polaron hopping conduction is described by the Jonscher's power law for the universal dielectric response as $f\varepsilon' = \frac{\tan\left(s\pi/2\right)\sigma_0}{2\pi\varepsilon_0} f^S + \varepsilon_\infty$ where σ_0 and s are temperature dependent terms, and ε_0 is the permittivity of free space [55]. ε_∞ denotes the high-frequency limit of the dielectric constant arising from the ionic and electronic polarization [56]. The log-log plot $\log_{10}(f\varepsilon')$ vs. $\log_{10}(f)$ should be a straight line with slope s for a given temperature. In figure 4.8 (c), a straight line is observed for the

high-temperature (150 K), low-frequency regime. With lowering the temperature (150 K to 80 K), the straight line part is reduced due to the freezing of charge carriers that reduce the dipolar effects [17, 57]. At very low temperature (40 K), only a straight line is seen where the dielectric contribution is intrinsic and obeys the universal power law regardless of the frequency [57]. The universal dielectric response law is applicable for materials with localized hopping of charge carriers.

The ε" vs. f plot in the log scale (figure 4.8 (d)) shows linearity for $T<T_C$. At very low temperature, the high spin moment localizes the charge carriers, and a straight line is observed regardless of the frequency (40 K, and 50 K). For temperatures near and above T_C (60 K, 70 K, and 80 K), a linear part is present at the low-frequency region due to the presence of a Maxwell-Wagner (M-W) type relaxation [19]. A Debye-type relaxation occurs in the high-frequency region at these temperatures as an appearance of a curve. For high temperatures (90 K and above), the linear region disappears while the curve appears distinctly. Thus we could conclude that the M-W interfacial polarization persists in the material around T_C. Around the T_C, a combination of M-W and Debye relaxation occurs, where the M-W dominates below T_C and Debye-type dominates above T_C. The difference in activation energy below and above T_C is due to the difference in relaxation mechanisms. Similar relaxation was reported for $LaCo_{0.5}Mn_{0.5}O_3$ [19].

4.3.5 Magnetodielectric coupling

The ε and tan δ are measured with and without a magnetic field of 5 kOe. The equations: $MD\% = \frac{[\varepsilon_H - \varepsilon_0]}{\varepsilon_0}$ x 100 and $MDL\% = \frac{[\tan\delta_H - \tan\delta_0]}{\tan\delta_0}$ x 100 are used for calculating the MD and MD loss (MDL) coupling. Variation of MD and

MDL as a function of temperature at frequencies 4 kHz, 8 kHz, 12 kHz, 15 kHz, 18 kHz, 20. 5 kHz, 40.9 kHz, 81.7 kHz, 122.5 kHz, 204.2 kHz, 285.8 kHz, 367.4 kHz, 449.0 kHz, 530.7 kHz, 612.3 kHz, 693.9 kHz, 775.5 kHz, 857.2 kHz, 938.8 kHz, and 1 MHz are shown in figure 4.9 (a) and 4.9 (b) respectively. MD coupling is observed for temperature range 50-150 K with maximum MD response found for 67-120 K for the frequencies ranging from 4 kHz to 1 MHz. The MD starts increasing from ~0% at 50 K and reaches the maximum value (MD_{Max}) ~55% at 67 K (for 4 kHz). After reaching MD_{Max}, MD decrease to 0% with increasing temperature. The MD_{Max} decreases and the temperature corresponding to MD_{Max} increases as frequency is increased up to 20.5 kHz. The trend in changing the MD_{Max} with a frequency above 20.5 kHz (40.9 kHz to 1 MHz) is quite different from that in the low-frequency region (4 kHz to 20.5 kHz). Here, the activation energy is ~0.05 eV, and in the further increased frequency region, the activation energy is 0.07 eV. Generally, the MD_{Max} decrease on increasing the frequency [12]. The trend in changing the MD_{MAX} is altered as per the dynamic crossover observed in relaxation. The peak corresponding to MD_{Max} has shifted to a higher temperature and the MD_{Max} increases with increasing frequency up to 285.8 kHz. A maximum of 61% MD is observed for 285.8 kHz at 105 K. MD decreases with frequency after this point. The variation of MD_{Max} with frequency is plotted in the inset of figure 4.9 (c). The change in MDL with temperature and frequency is similar to the MD behavior. It can be seen that a negative MDL is observed for a particular frequency at a temperature where a maximum positive MD is observed. Also, a positive MDL is obtained corresponding to the lowest MD (figure 4.9 (d)). Such MD effects occur

when the core of the grain influences the coupling between magnetic and charge order rather than the grain interface or boundary [5].

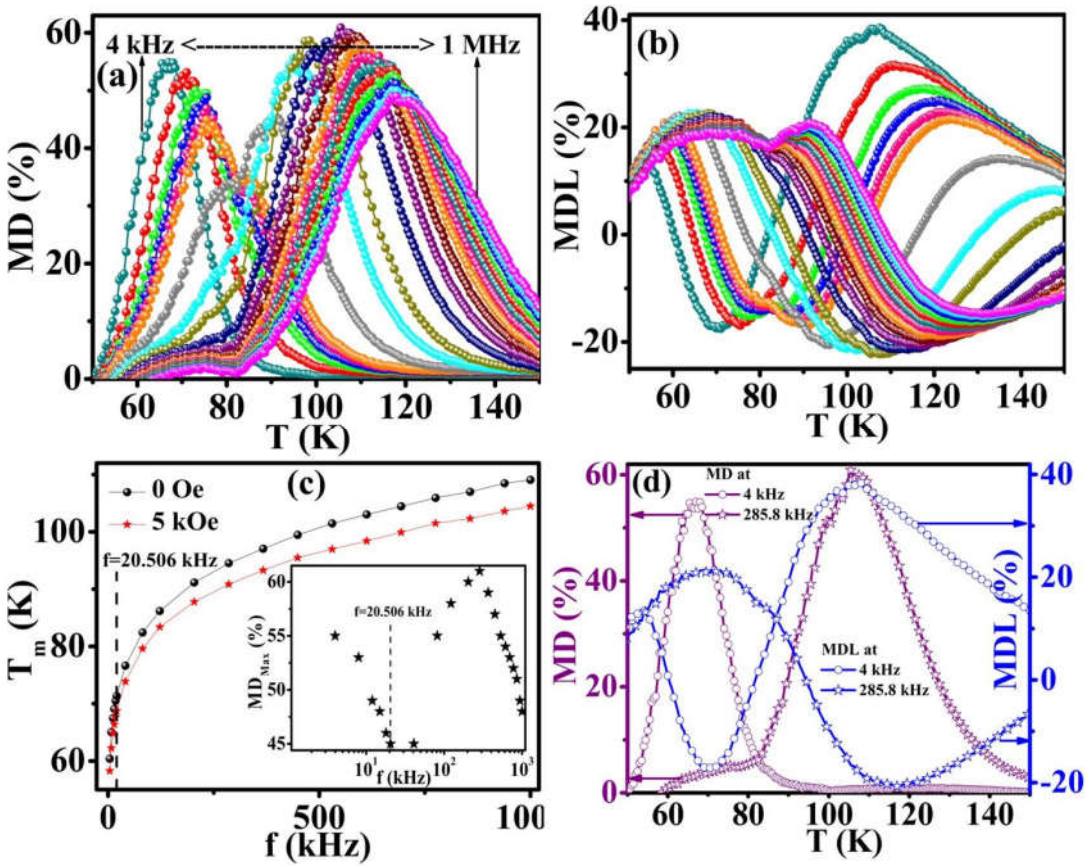

Figure 4.9 Temperature variations of (a) magnetodielectric coupling and (b) magnetodielectric loss coupling at various frequencies (c) The maximum in tan δ (T_m) corresponding to each frequency with 0 Oe and 5 kOe. Inset is showing the maximum MD coupling observed for each frequency. (d) Variation of magnetodielectric coupling and magnetodielectric loss coupling with the temperature at 4 kHz and 285.8 kHz; depicting negative MDL corresponding to positive MD and positive MDL corresponding to a low value of MD.

Effect of the core-dominated MR on the Maxwell-Wagner interfacial polarization is responsible for the positive MD and negative MDL [5]. The magnetic

ordering with the presence of GP and the polarization effects are responsible for the unusual trends in the MD behavior. The Maxwell-Wagner polarization ceases above 120 K as in figure 4.8 (d), and the material becomes completely PM above T^*=115 K as in figure 4.5 (a). Thus the MD coupling is zero above this temperature. Accordingly, the occurrence of MD in La_2CuMnO_6 is correlated to the presence of FM short-range correlations and the Maxwell-Wagner interfacial polarization. The changes in the dielectric behavior in La_2CuMnO_6 are brought by both the magnetic ordering and the external magnetic field. A large MD around T_C is reported in ferromagnetic/ferroelectric materials, as a result of the fluctuation in spin-pair correlation [6, 8-10, 13]. It is seen that the temperature (T_m) corresponding to the maxima in tan δ is shifting to lower temperature on an application of the magnetic field as shown in figure 4.9 (c). Below the frequency 20.5 kHz, the difference between T_m (0 Oe) and T_m (5 kOe) is smaller than that above this frequency. On application of the magnetic field, the spins align in order and the resonance can be easily achieved at a lower temperature. This phenomenon demonstrates the influence of the magnetic field on the relaxation of the dipole. The electric dipole fluctuations are affected by the magnetic ordering, and the dielectric relaxations are magnetically controllable.

4.4. Conclusion

The perovskite La_2CuMnO_6 is synthesized with orthorhombic *Pbnm* crystal structure. The microstructure of the sintered pellet contains a bimodal distribution of grains with mean average size distributed around 200 nm to 750 nm. The magnetic measurements demonstrated a combined AFM and FM interaction below T_C=72 K with T_N=5 K. The material exhibit ferromagnetic short range correlations above T_C

signifying the existence of a Griffiths-like phase in between T_C^R=27 K and T^*=115 K with λ_{GP}=0.96 and λ_{PM}=0.003. A high contribution from electronic specific heat to the total specific heat is observed which points to the possibility of the co-existence of an FM and a VRH active charge localized state. The conduction mechanism in the material follows the VRH model. A frequency independent intrinsic dielectric constant ~20 is observed below 50 K. The material shows a dynamic Arrhenius to Arrhenius crossover in the relaxation phenomena. The dynamic crossover in distributing the relaxation around T_C is attributed to the magnetic ordering along with the existence of GP. Just above T_C, the Maxwell-Wagner effect along with a contribution from Debye relaxation occurs while the Maxwell-Wagner relaxation dominates for low frequency below T_C. MD coupling is observed for 50-150 K with maximum MD response found for 67-120 K for the frequencies ranging from 4 kHz to 1 MHz. A maximum MD of 55% is observed at 67 K for 4 kHz, and 61% is observed at 105 K for 285.8 kHz. The different trend is observed for MD with a dynamic crossover around T_C. MDL behaves in a manner similar to that of MD. A negative MDL is observed corresponding to a positive MD and a positive MDL is observed corresponding to a low value of MD. The origin of MD in La_2CuMnO_6 is correlated to the presence of FM short-range correlations, and the influence of a core grain dominated MR on Maxwell-Wagner interfacial polarization. The magnetic ordering and the external magnetic field have control over the electric dipole relaxations in the material.

4.5. References

[1] A.K. Kundu, Magnetic Perovskites, Springer India, 2016.

[2] C.N.R. Rao, B. Raveau, Colossal Magnetoresistance, Charge Ordering and Related Properties of Manganese Oxides, World Scientific, 1998.

[3] A.P. Ramirez, Journal of Physics: Condensed Matter, 9 (1997) 8171.

[4] G. Lawes, A.P. Ramirez, C.M. Varma, M.A. Subramanian, Physical Review Letters, 91 (2003) 257208.

[5] G. Catalan, Applied Physics Letters, 88 (2006) 102902.

[6] Q. Jiang, S.J. Gong, The European Physical Journal B - Condensed Matter and Complex Systems, 43 (2005) 333-338.

[7] K. Dey, A. Indra, D. De, S. Majumdar, S. Giri, ACS Applied Materials & Interfaces, 8 (2016) 12901-12907.

[8] P. Padhan, H.Z. Guo, P. LeClair, A. Gupta, Applied Physics Letters, 92 (2008) 022909.

[9] C.-H. Yang, S.-H. Lee, T.Y. Koo, Y.H. Jeong, Physical Review B, 75 (2007) 140104.

[10] A. Venimadhav, D. Chandrasekar, J. Krishna Murthy, Applied Nanoscience, 3 (2013) 25-28.

[11] K.D. Chandrasekhar, A.K. Das, A. Venimadhav, Journal of Physics: Condensed Matter, 24 (2012) 376003.

[12] J.K. Murthy, K.D. Chandrasekhar, S. Murugavel, A. Venimadhav, Journal of Materials Chemistry C, 3 (2015) 836-843.

[13] T. Kimura, S. Kawamoto, I. Yamada, M. Azuma, M. Takano, Y. Tokura, Physical Review B, 67 (2003) 180401.

[14] D. Choudhury, P. Mandal, R. Mathieu, A. Hazarika, S. Rajan, A. Sundaresan, U.V. Waghmare, R. Knut, O. Karis, P. Nordblad, D.D. Sarma, Physical Review Letters, 108 (2012) 127201.

[15] R. Cortés-Gil, M.L. Ruiz-González, J.M. Alonso, M. García-Hernández, A. Hernando, J.M. González-Calbet, Chemistry of Materials, 25 (2013) 2100-2108.

[16] A.K. Biswal, J. Ray, P.D. Babu, V. Siruguri, P.N. Vishwakarma, AIP Conference Proceedings, 1591 (2014) 1630-1632.

[17] C.C. Wang, L.W. Zhang, New Journal of Physics, 9 (2007) 210.

[18] T. Prasit, T. Suwat, Y. Teerapon, M. Santi, Journal of Physics: Condensed Matter, 20 (2008) 395227.

[19] K. Manna, R.S. Joshi, S. Elizabeth, P.S.A. Kumar, Applied Physics Letters, 104 (2014) 202905.

[20] A.S. Friedrich Kremer, Broadband Dielectric Spectroscopy, 23, 2003.

[21] C.M. Roland, Soft Matter, 4 (2008) 2316-2322.

[22] K. Sasaki, R. Kita, N. Shinyashiki, S. Yagihara, The Journal of Physical Chemistry B, 120 (2016) 3950-3953.

[23] R. Casalini, C.M. Roland, Physical Review B, 71 (2005) 014210.

[24] S. Pawlus, M. Paluch, M. Sekula, K.L. Ngai, S.J. Rzoska, J. Ziolo, Physical Review E, 68 (2003) 021503.

[25] K.L. Ngai, Relaxation and Diffusion in Complex Systems, 1 ed., Springer-Verlag New York, 2011.

[26] J. Gardner, F. Yu, C. Tang, W. Kockelmann, W. Zhou, F.D. Morrison, Chemistry of Materials, 28 (2016) 4616-4627.

[27] C.G.F. Stenger, A.J. Burggraaf, physica status solidi (a), 61 (1980) 653-664.

[28] H. Nhalil, H.S. Nair, C.M.N. Kumar, A.M. Strydom, S. Elizabeth, Physical Review B, 92 (2015) 214426.

[29] V.G. Nair, A. Das, V. Subramanian, P.N. Santhosh, Journal of Applied Physics, 113 (2013) 213907.

[30] J. Pezhumkattil Palakkal, P.N. Lekshmi, S. Thomas, K.G. Suresh, M.R. Varma, RSC Advances, 5 (2015) 105531-105536.

[31] B. Toby, Journal of Applied Crystallography, 34 (2001) 210-213.

[32] B. Folkesson, P. Sundberg, L. Johansson, R. Larsson, Journal of Electron Spectroscopy and Related Phenomena, 32 (1983) 245-256.

[33] N.N.A. Ivanov-Emin B.N., Zaitsev B.E., Ivanova T.M., Zh. Neorg. Khimii 27 (1982) 2.

[34] A.K. Pathak, D. Paudyal, W.T. Jayasekara, S. Calder, A. Kreyssig, A.I. Goldman, K.A. Gschneidner, V.K. Pecharsky, Physical Review B, 89 (2014) 224411.

[35] R.B. Griffiths, Physical Review Letters, 23 (1969) 17-19.

[36] O. Chauvet, G. Goglio, P. Molinie, B. Corraze, L. Brohan, Physical Review Letters, 81 (1998) 1102-1105.

[37] W. Jiang, X. Zhou, G. Williams, Y. Mukovskii, K. Glazyrin, Physical Review Letters, 99 (2007) 177203.

[38] C. Magen, P.A. Algarabel, L. Morellon, J.P. Araújo, C. Ritter, M.R. Ibarra, A.M. Pereira, J.B. Sousa, Physical Review Letters, 96 (2006) 167201.

[39] S. Guo, D.P. Young, R.T. Macaluso, D.A. Browne, N.L. Henderson, J.Y. Chan, L.L. Henry, J.F. DiTusa, Physical Review Letters, 100 (2008) 017209.

[40] W. Jiang, X. Zhou, G. Williams, Y. Mukovskii, K. Glazyrin, Physical Review B, 77 (2008) 064424.

[41] A.K. Pramanik, A. Banerjee, Physical Review B, 81 (2010) 024431.

[42] P. Tong, B. Kim, D. Kwon, T. Qian, S.-I. Lee, S.W. Cheong, B.G. Kim, Physical Review B, 77 (2008) 184432.

[43] S. Zhou, Y. Guo, J. Zhao, L. He, L. Shi, The Journal of Physical Chemistry C, 115 (2011) 1535-1540.

[44] A. Ślebarski, J. Goraus, M. Fijałkowski, Physical Review B, 84 (2011) 075154.

[45] D. Bhoi, N. Khan, A. Midya, M. Nandi, A. Hassen, P. Choudhury, P. Mandal, The Journal of Physical Chemistry C, 117 (2013) 16658-16664.

[46] M.R. Lees, O.A. Petrenko, G. Balakrishnan, D. McK. Paul, Physical Review B, 59 (1999) 1298-1303.

[47] R.K. Zheng, A.N. Tang, Y. Yang, W. Wang, G. Li, X.G. Li, H.C. Ku, Journal of Applied Physics, 94 (2003) 514-518.

[48] C.L. Lu, K.F. Wang, S. Dong, J.G. Wan, J.-M. Liu, Z.F. Ren, Journal of Applied Physics, 103 (2008) 07F714.

[49] A. Shahee, K. Singh, R.J. Choudhary, N.P. Lalla, physica status solidi (b), 252 (2015) 1832-1838.

[50] N.F. Mott, Philosophical Magazine, 19 (1969) 835-852.

[51] N.F. Mott, Metal-Insulator Transitions, Taylor and Francis, London 1990.

[52] J. Krishna Murthy, A. Venimadhav, Journal of Applied Physics, 111 (2012) 024102.

[53] K.D. Chandrasekhar, A.K. Das, C. Mitra, A. Venimadhav, Journal of Physics: Condensed Matter, 24 (2012) 495901.

[54] K.S. Cole, R.H. Cole, The Journal of Chemical Physics, 9 (1941) 341-351.

[55] A.K. Jonscher, Dielectric Relaxation in Solids, Chelsea Dielectrics Press, London, 1983.

[56] P. Lunkenheimer, S. Krohns, F. Gemander, W.W. Schmahl, A. Loidl, Scientific Reports, 4 (2014) 6020.

[57] C. Ganeshraj, S. Kavita, R. Mahendiran, N. Sharma, A. Das, P.N. Santhosh, Applied Physics Letters, 103 (2013) 112909.

Chapter 5

Multiple magnetic transitions, Griffiths-like phase, and Magnetoresistance in La_2CrMnO_6

This chapter deals with the magnetic, dc transport and magnetoresistance of disordered double perovskite La_2CrMnO_6. Multiple magnetic transitions and Griffiths-like phase are observed in this material. A combination of variable range hopping and nearest neighbor small polaron hopping governs the conduction mechanism in the material. A negative magnetoresistance of 22% at 105 K is observed for the material at 90 kOe which increases to 29% near 110 K and reduced gradually to zero on further increase in the temperature.

5.1 Introduction

The magnetism in transition metal oxides always facilitates science and technology on the foundation of spin, charge, and orbital contribution from the transition element cations [1-3]. The rare-earth (RE) based manganites ($REMnO_3$) further provide different physical properties due to the presence of Mn^{3+} and Mn^{4+} cations along with the structural and Jahn-Teller (J-T) distortion [3-5]. The magnetic and crystal structure plays a significant role in determining various magneto-physical properties like magnetoresistance (MR), magnetodielectric coupling, etc. observed for such systems [4, 6, 7]. The J-T ion Mn^{3+} provides J-T distortion in the high-spin state. The presence of Mn^{4+} and Mn^{3+} facilitate the double exchange interaction in addition to the 180º superexchange interaction among the cations (Mn-O-Mn). The manganite with double perovskite (RE_2BMnO_6) structure has a greater contribution to the frustrated crystallographic structure and its magnetic properties due to the addition of another transition element (B) cation. The superexchange interaction between the B and Mn cations (B-O-Mn) will further give complex magnetism since there is the possibility for four types of cations (B^{2+}, B^{3+}, Mn^{4+}, and Mn^{3+}). If the cationic radii of the B and Mn are comparable, the possibility to form an exact double ordered perovskite structure is very less. The resulting antisite disorder will further introduce complex magnetic interactions since the antiferromagnetic (AFM) superexchange interaction arises among the cations itself (B-O-B or Mn-O-Mn). Such competing magnetic interactions often lead to Griffiths-like phase (GP) which constitutes a matrix of both ferromagnetic (FM) and paramagnetic (PM) correlations [8-18]. R B Griffiths originally demonstrated the GP as a nonanalytic behavior of random Ising FM above the critical temperature

(T_C) where an FM phase get diluted with an increasing PM contribution as the temperature is increased [8]. In other words, GP is a diluted Ising FM [8]. The susceptibility of a PM material will follow the Curie law: $\chi^{-1} = \frac{T}{C_W}$ and an FM material follows the Curie-Weiss (CW) law: $\chi^{-1} = \frac{T-\Theta}{C_W}$. Since the material contains both PM and FM correlations above transition for the case of GP, it will show a deviation from the CW law above T_C, and the deviation gets decreased on increasing the external field. On reaching a temperature called Griffiths temperature (T*), the material becomes PM completely and follows the CW law above T*. A power law: $\chi^{-1} \propto (T - T_C^R)^{1-\lambda}$ is used to fit the susceptibility of a GP, provided $0 \leq \lambda < 1$ where T_C^R is the critical temperature of the random FM [9-20]. The T_C^R is the point which gives a λ_{PM} value close to 0 above T* such that the power law becomes the CW law in the PM region. The GP is more clearly observable at low magnetic fields, and the λ_{GP} is close to 1 at small magnetic fields which reduce to 0 as the field is increased, where it follows the CW law.

Though the observation of MR in a material is found to be of different origin, many reports are claiming that the presence of GP can be a cause for the occurrence of MR in many manganite systems [4, 6, 21-24]. In the present chapter, detailed magnetic properties of the material are analyzed with the aid of dc and ac magnetometry. The dc transport mechanism is investigated, and a considerable MR is observed for the system.

5.2 Experimental

The combustion method is used to synthesize La_2CrMnO_6 where citric acid is added as a fuel. A complete synthesis method is reported on La_2FeMnO_6 in chapter 3 [18]. The precursor powders were pelletized by using a hydraulic press by adding polyvinyl alcohol as a binder. The sintering of the pellets was done at 1100ºC for 22 hours. The powder X-ray diffraction (XRD) data of the material is obtained by Philips PANalytical X'Pert Pro Powder X-Ray Diffractometer with a Ni-filtered Cu Kα radiation (λ=1.5406 Å). The GSAS – EXPGUI [25] software is used to do the Rietveld refinement of the XRD pattern. A portion of the crystal structure of La_2CrMnO_6 is framed by using CrystalMaker® software, CrystalMaker Software Ltd, Oxford, England. Thermo Scientific X-ray photoelectron spectrometer is used to take the X-ray photoelectron spectroscopy (XPS) of the material. The peaks are fitted by using the XPS Peak Fit software. The magnetic moment is measured as per different protocols for temperatures ranging from 2 to 300 K and magnetic field ranging from -90 kOe to +90 kOe by using Vibrating Sample Magnetometer attached to the Physical Property Measurement System (PPMS, the Quantum Design). AC susceptibility for the temperature ranges 2-300 K for different frequencies is done by ACMS option attached to PPMS with a drive ac field 5 Oe with dc magnetic field of 0 Oe and 100 Oe. The heat capacity option for the PPMS is used to measure the specific heat for 2-300 K temperatures. DC resistivity measurement is done at temperatures 101-286 K for field 0- ±90 kOe by using Electrical Transport option for the PPMS.

5.3 Results and Discussion

5.3.1 Structural properties

The observed, calculated, and difference XRD pattern of La_2CrMnO_6 is plotted in figure 5.1 (a) after the Rietveld structural refinement. The Bragg positions are indicated, and prominent peaks are indexed. The crystal structure is orthorhombic, with space group *Pbnm,* which is consistent with previous reports on La_2CrMnO_6 existing in orthorhombic structure [26-30]. The (011) reflection, which is considered as the superlattice reflection, is expected to present at 2θ=19.80º in *Pbnm* crystal structure (ICSD Collection Code: 154966). Since this is absent in the present data, it is considered that the cations are not ordered in the perovskite B-lattice [31, 32]. A portion of the crystal structure along with the reference axes is depicted in figure 5.1 (b). The unit cell parameters obtained from the structural refinements are *a= 5.5130(3) Å, b= 5.4752(3) Å, c= 7.7601(4) Å*, and *α=β=γ=90º*. The Rietveld fitting factors are $_WR_P$=8.7%, R_P=6.7%, and χ^2=1.6. The two types of <Cr/Mn-O-Cr/Mn> bond angles are $\langle\theta_1\rangle$ =156.5(16)º and $\langle\theta_2\rangle$ =165.5(15)º for each type of oxygen (O1 and O2). The angle distortions are calculated by the equation $\langle\omega\rangle = 180 - \langle\theta\rangle$ as $\langle\omega_1\rangle$=23.5º and $\langle\omega_2\rangle$=14.5º with average $\langle\omega\rangle$=19º. The J-T distortion is calculated by the equation $\Delta d = \frac{1}{6}\sum_1^6\left[\left(d_n - \langle d\rangle\right)/\langle d\rangle\right]^2$ (where d_n is nth Cr/Mn-O bond length and <d> is the average for all the Cu/Mn-O bond lengths) [3]. The calculated Δd is 4.34x10^{-3}.

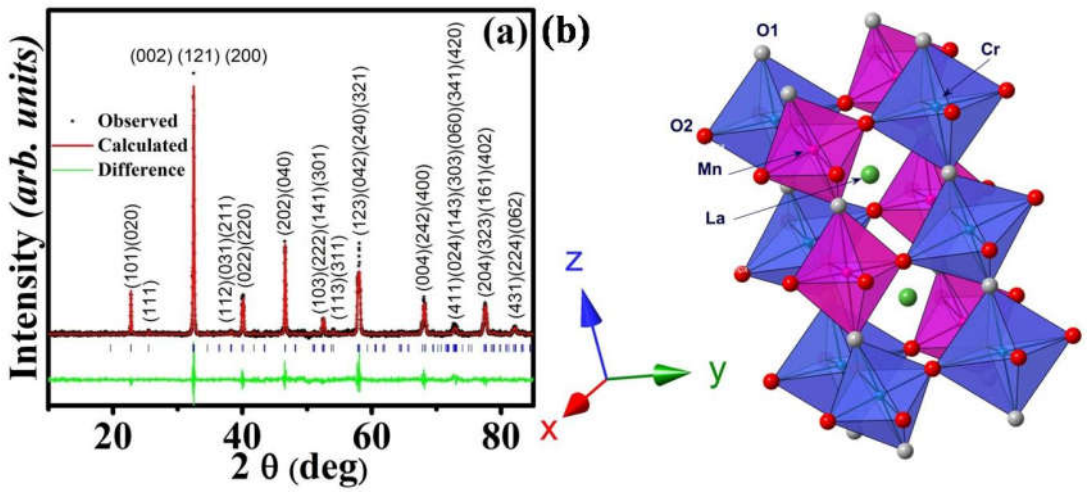

Figure 5.1. (a) Observed, calculated, and the difference XRD pattern of La_2CrMnO_6 obtained from Rietveld refinement. The blue bars indicate the Bragg positions. (b) A portion of the La_2CrMnO_6 crystal structure along with the reference axes.

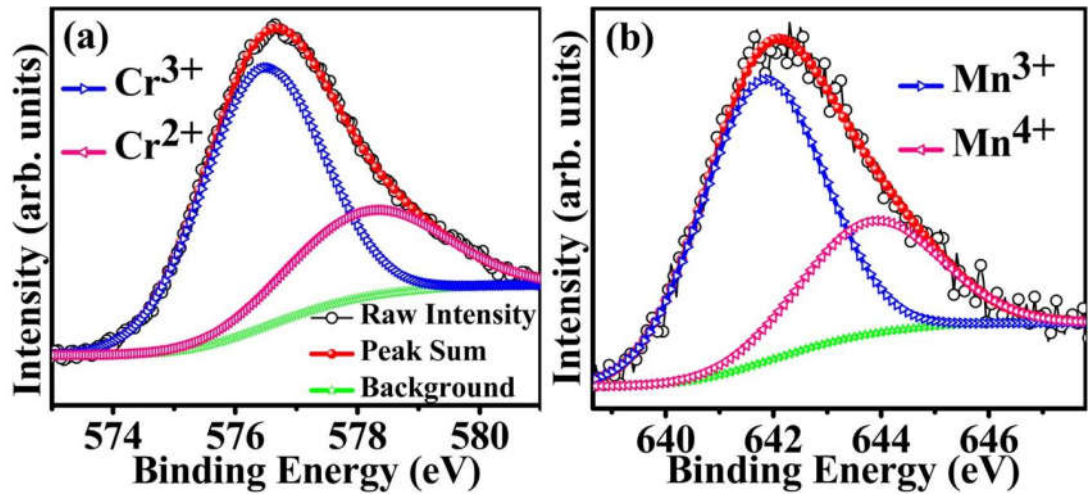

Figure 5.2. XPS spectra of (a) Cr $2p_{3/2}$ and (b) Mn $2p_{3/2}$ in La_2CrMnO_6 along with the fitted curves.

The XPS spectra for the Cr 2p and Mn 2p of La_2CrMnO_6 are obtained. The C 1s is taken as the reference energy for correcting the binding energies. The fitted curves give peak positions at 576.43 eV and 578.14 eV for the Cr $2p_{3/2}$ (figure 5.2 (a)) which point the presence of Cr^{3+} and Cr^{2+} cations in La_2CrMnO_6 [33, 34].

Similarly the fitted curves have peak positions at 641.79 eV and 643.80 eV corresponding to the Mn^{3+} and Mn^{4+} cations (figure 5.2 (b)) respectively [35, 36]. From the peak area of specific cations, the percentage contribution from each cation is determined. As of the area under the fitted curves in figure 5.2 (a), 70.56 % Cr^{3+} and 29.44% Cr^{2+} contribute to the total Cr present in the material. Similarly, from the area under the fitted curves in figure 5.2 (b), 69.17 % Mn^{3+} and 30.83% Mn^{4+} contribute to the total Mn present in La_2CrMnO_6.

5.3.2 DC and AC Magnetic Properties

The variation of zero field cooled (ZFC) and field cooled (FC) magnetic moment as a function of temperature from 2-300 K is measured at 100 Oe, 500 Oe, and 1000 Oe as shown in figure 5.3 (a). At low temperatures, the FC and ZFC are not merging as a result of the competing magnetic interactions. Different magnetic exchange interactions are possible in the disordered La_2CrMnO_6 system containing mixed valence cations, with the lack of cationic ordering. The material having Cr^{2+}, Cr^{3+}, Mn^{3+}, and Mn^{4+} cations is subjected to various superexchange and double exchange interactions viz. Cr^{2+}-O-Mn^{3+}, Cr^{2+}-O-Mn^{4+}, Cr^{3+}-O-Mn^{3+}, Cr^{3+}-O-Mn^{4+}, Cr^{2+}-O-Cr^{2+}, Cr^{3+}-O-Cr^{3+}, Mn^{3+}-O-Mn^{3+}, Mn^{4+}-O-Mn^{4+}, Cr^{2+}-O-Cr^{3+}, and Mn^{3+}-O-Mn^{4+} leading to FM and AFM contributions. Competition among these interactions, quantified through different J values occurs, and hence a frustrated magnetic behavior is shown by the material. A ferromagnetic-like behavior below 190 K and a competitive interaction between Cr and Mn have reported previously for La_2CrMnO_6 [37]. The bifurcation between the FC and ZFC curves starts at 170 K for 100 Oe and the temperature of bifurcation decreases as the field is increased. It is due to the suppression of magnetic inhomogeneities on the application of the high

magnetic field. Initially, the magnetic moment in the ZFC curve increases as the temperature is increased from 2 K to 9 K and then decreases with further increase in the temperature for high field similar to AFM. The dM/dT vs. T plot as shown in the inset of figure 5.3 (a) has two minima corresponding to magnetic transitions at T_{C1}=56 K and T_C=115 K for 100 Oe. The minima at 56 K is independent of the field while that at 115 K is shifting to low temperature with increase in the field. The ZFC at 100 Oe is almost similar to the reported one, but the irregularity at 60 K is not observed in reports [30, 37]. The irregularity at 60 K in the ZFC curve is equivalent to the T_{C1} which is clearly observable in the M/H vs. T plot (figure 5.3 (b)). All these suggest the presence of a combination of magnetic interactions in the low-temperature phase.

The magnetic hysteresis (MH) loop taken at different temperatures is shown in the inset of figure 5.3 (b). At 2 K and 10 K, the saturation magnetic moment (M_S) is ~1.96 μ_B/f.u. On further increase in temperature, the M_S is decreased. The zoomed central portion of the MH hysteresis loop is shown in figure 5.3 (c) which shows the overriding coercivity at 150 K than that at 2 K. The variation of coercivity (H_C) and remanence (M_r) is plotted against temperature as shown in the inset of figure 5.3 (d). The values of both M_r and H_C are zero at 180 K and increases with decreasing temperature. On reaching ~150 K, with further decrease in temperature, the H_C value decreases. Below the T_{C1}, the H_C is again found to be increased with a decrease in temperature. This trend in the variation of H_C with temperature indicates the presence of inhomogeneous magnetic interactions and magnetic anisotropy in the material. The H_C is related to the saturation magnetization (M_s) and the uniaxial magnetic anisotropy of the crystal (K) as $H_C = 2K/M_S$. Usually the H_C decrease on

increasing the temperature since the anisotropy decreases than does the magnetization [38, 39]. A reversal of this tendency is observed in systems with shape anisotropy, magnetoelectric coupling, and the presence of inhomogeneous magnetic interactions like the simultaneous occurrence of spin glass, AFM, PM, and FM correlations, etc. [38-41]. Further studies are necessary to confirm the precise origin of this trend. A considerable H_C and M_r are observed even above the T_C, pointing the presence of FM short-range correlations above T_C.

Table 5.1. The effective moment (in units of μ_B / f.u.) calculated for different combinations of Cr and Mn cations.

Spin Only interaction	**Mn^{3+} (HS)**	**Mn^{3+} (LS)**
Cr^{3+}	6.245	4.796
	Cr^{2+} (HS)	**Cr^{2+} (LS)**
Mn^{4+}	6.245	4.796
Spin-Orbit Coupling	**Mn^{3+} (HS)**	**Mn^{3+} (LS)**
Cr^{3+}	9.433	7.583
	Cr^{2+} (HS)	**Cr^{2+} (LS)**
Mn^{4+}	9.433	7.583

The FC inverse susceptibility as a function of temperature at 100 Oe is shown in figure 5.3 (d). A linear fit to the plot based on the CW law is shown as a solid blue line. The inverse susceptibility vs. T shows a deviation from the CW law as a downturn below the T*=180 K. This sort of deviation is exhibited by materials with a GP [18]. The inverse susceptibility precisely follows the CW above T* where

the material is considered to be completely PM. The CW fit gives Θ=122.6(1) K. The effective PM moment is calculated by the equation $\mu_{eff} = 2.828\sqrt{C_w}$ as 4.916(3) μ_B / f.u. where the Curie constant C_w is obtained from the slope of the straight line. The effective moment is theoretically calculated for various combinations of Cr and Mn cations by the equation $\mu_{eff} = g\sqrt{s(s+1)}\mu_B$ for the spin-only case and by using the equation $\mu_{eff} = g_j\sqrt{j(j+1)}\mu_B$ for the case of spin-orbit interaction and tabulated in Table 5.1. The experimentally obtained effective moment (4.916(3) μ_B / f.u.) omits the possibility of a spin-orbit coupling in the material. The superexchange interaction between Cr^{3+} (t_{2g}^3 e_g^0) and Mn^{3+} (LS) (t_{2g}^4 e_g^0), as well as that between Cr^{2+} (LS) (t_{2g}^4 e_g^0) and Mn^{4+} (t_{2g}^3 e_g^0), is between two empty e_g^0 orbitals, which is strong and AFM according to the Goodenough-Kanamori rule [42]. The observed value of μ_{eff} (4.916(3) μ_B / f.u.) is slightly higher than that for these combinations (4.796 μ_B / f.u). So the presence of exchange interaction between Cr^{3+} (t_{2g}^3 e_g^0) and Mn^{3+} (HS) ($t_{2g}^3e_g^1$) as well as Cr^{2+} (HS) (t_{2g}^3 e_g^1) and Mn^{4+} (t_{2g}^3 e_g^0) are possible which is FM according to the Goodenough-Kanamori rule [42]. In addition to this, FM double exchange interaction is also possible in the system. The saturation magnetic moment (M_S) expected for Cr^{3+} and Mn^{3+} (LS), as well as Cr^{2+} (LS) and Mn^{4+}, is 5 μ_B /f.u., while the observed M_S is ~2 μ_B/f.u. at 2 K and 10 K. Since the system is disordered without a particular cationic ordering, a lower M_S value per f.u. is found experimentally.

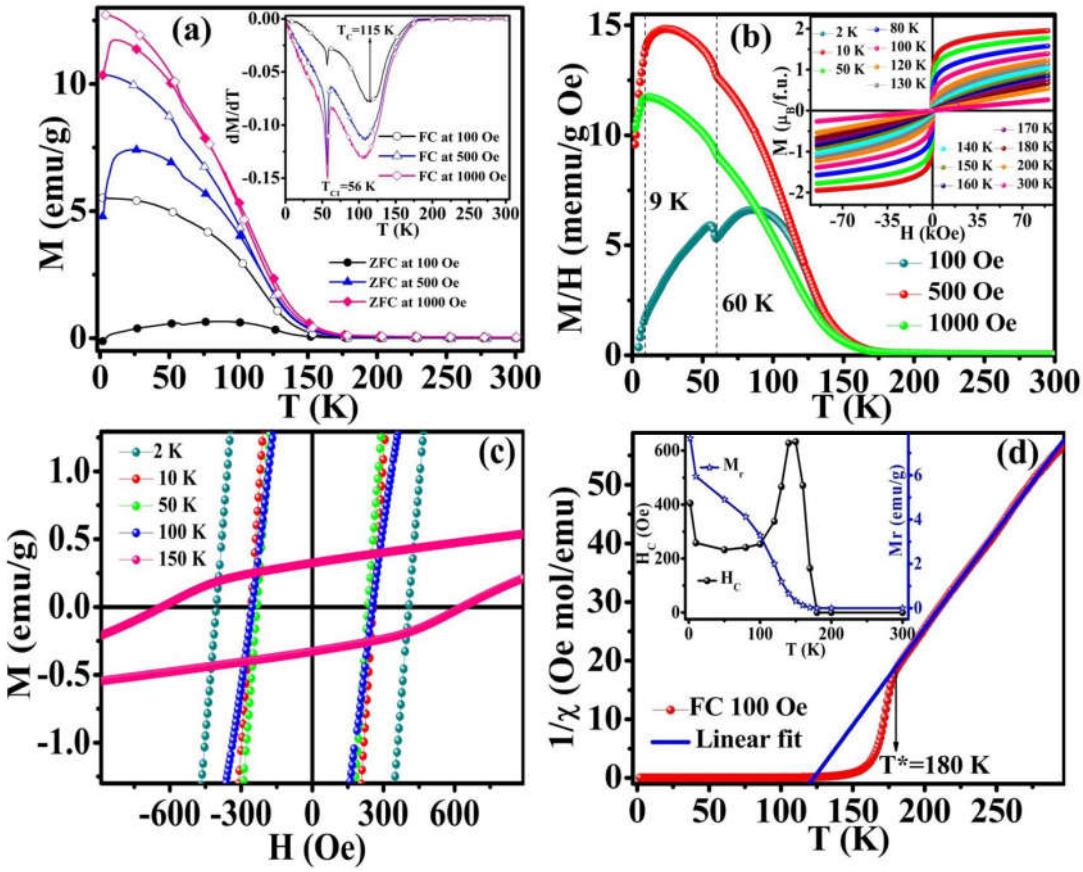

Figure 5.3 (a) ZFC and FC thermomagnetic curves at various fields. Inset is showing the dM/dT vs. T plot. (b) M/H vs. T of the ZFC curves at different fields indicating the dip at 60 K. Inset of (b) showing the isothermal magnetization curves recorded at different temperatures. (c) The zoomed center portion of MH loop at various temperatures. (d) Temperature dependence of inverse dc susceptibility (FC) at 100 Oe along with the CW fit (solid blue line). Inset of (d) depicting the variation of coercivity (H_C) and remanence (M_r) with temperature.

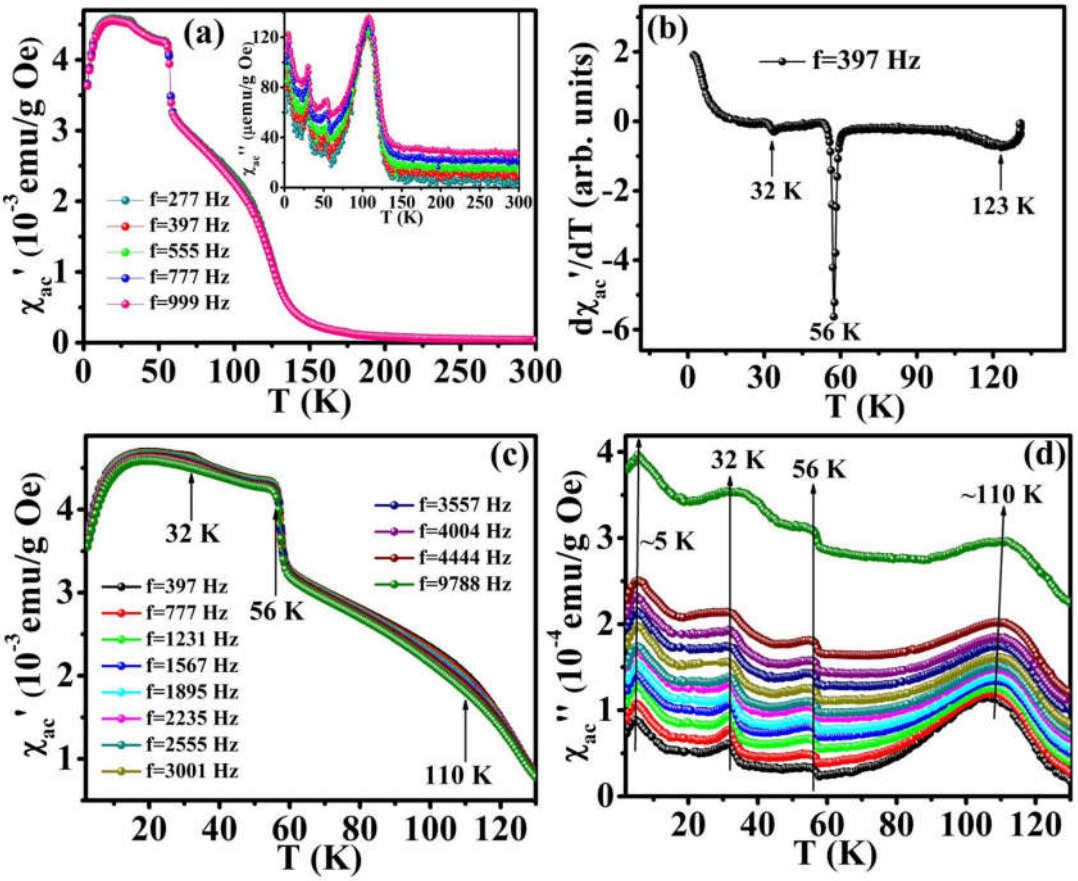

Figure 5.4 (a) Temperature dependence of real part of AC susceptibility (χ_{ac}') and inset showing the temperature dependence of imaginary part of AC susceptibility (χ_{ac}'') at various frequencies for 2-300 K. (b) The $d\chi_{ac}'/dT$ vs. T plot showing the minima at 32 K, 56 K, and 123 K. Temperature dependence of (c) real (χ_{ac}') and (d) imaginary (χ_{ac}'') part of AC susceptibility for 2-130 K at various frequencies.

The variation of real (χ_{ac}') and imaginary (χ_{ac}'') part of AC susceptibility with temperatures 2-300 K is measured at various frequencies (figure 5.4 (a)). χ_{ac}' and χ_{ac}'' show multiple transition points for temperatures ranging from 2-130 K as depicted in figure 5.4 (c) and (d) respectively. The $d\chi_{ac}'/dT$ vs. T plot (figure 5.4 (b)) gives minima at 32 K, 56 K, and 123 K. The minimum observed at 123 K in $d\chi_{ac}'/dT$ (H_{ac}=5 Oe) corresponds to the minima of dM/dT (H_{dc}=100 Oe) observed at 115 K,

dM/dT (H_{dc}=500 Oe) observed at 108 K, and dM/dT (H_{dc}=1000 Oe) observed at 106 K. This difference is attributed to the effect of field strength. χ_{ac}" shows peaks at ~5 K, 32 K, 56 K and ~110 K. The peaks at 32 K and 56 K are not showing any frequency dependent shift to the temperature position while peaks at ~5 K and ~110 K are showing frequency dispersion as marked with arrows in the χ_{ac}" vs. T plot (figure 5.4 (d)). The peaks at 32 K and 56 K (T_{C1}) are a kind of FM transitions and the peaks at ~5 K, and ~110 K are of a spin glass origin.

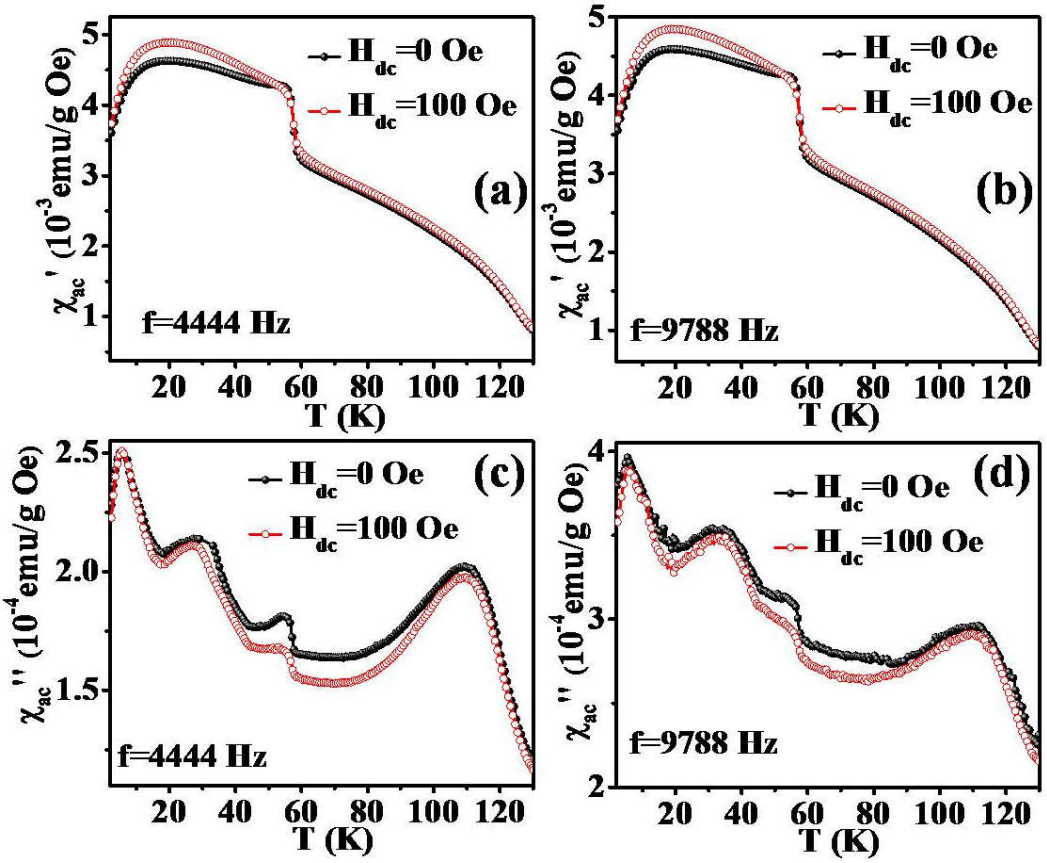

Figure 5.5. Temperature dependence of real (χ_{ac}') part of ac susceptibility at H_{dc}=0 and 100 Oe for (a) f=4444 Hz, (b) f=9788 Hz. Temperature dependence of imaginary (χ_{ac}") part of ac susceptibility at H_{dc}=0 and 100 Oe for (c) f=4444 Hz, (d) f=9788 Hz.

The ac susceptibility in an applied dc magnetic field (H_{dc}) of 100 Oe for 2-130 K with frequencies 4444 Hz and 9788 Hz were carried out (figure 5.5). Since the χ_{ac}' reveals the sensitivity of the material to the external applied field, the value of χ_{ac}' increases with the application of H_{dc}. The significant increase is observed below the FM transition temperature 56 K. The χ_{ac}'' decreases on application of an external field due to a decrease in energy dissipation, distinctly in the FM region [43]. The relative shift in T_m $\left(\delta T_m = \frac{\Delta T_m}{T_m \Delta \log(\omega)} \right)$ can be used to illustrate the magnetic order of the system. δT_m is usually small for spin/cluster-glass systems and ~2 for non-interacting superparamagnetic materials. In the present study, we have observed δT_m=0.03 for the peaks at ~5 K and δT_m=0.007 for the peaks at ~110 K. Both the relaxations are examined by the dynamical scaling analysis by using the critical slowing down relation,[44] $\frac{\tau}{\tau_0} = \left(\frac{T_m - T_{SG}}{T_{SG}} \right)^{-zv}$ where $\tau=(2\pi f)^{-1}$ is the relaxation time related to the frequency (f), τ_0 is the characteristic relaxation time of a single flip, T_{SG} is the critical spin glass ordering temperature when frequency tends to zero and zv is the dynamic critical exponent [44]. The ln τ vs. T_m plot along with the fit to the critical power law for transition near 5 K and near 110 K are shown in figure 5.6 (a) and (b) respectively. The values $\tau_0=2.0(2)\times10^{-6}$ s, T_{SG}=4.744(8) K, and zv=1.31(5) are obtained for the transition near 5 K and the values $\tau_0=5.6(9)\times10^{-7}$ s, T_{SG}=107.77(5) K, and zv=1.0(4) are obtained for the transition near 110 K. Typically, $\tau_0 \sim 10^{-10}$-10^{-13} s and zv ~ 4-12, for a non-interacting spin glass system. The obtained high value of τ_0 and low value of zv indicates a co-operative slow spin flipping due to the presence of randomly oriented FM clusters (clustered spin glass).

The cluster-glass behavior along with the anomalous multiple magnetic transitions are due to the competing magnetic interactions arising from Cr and Mn.

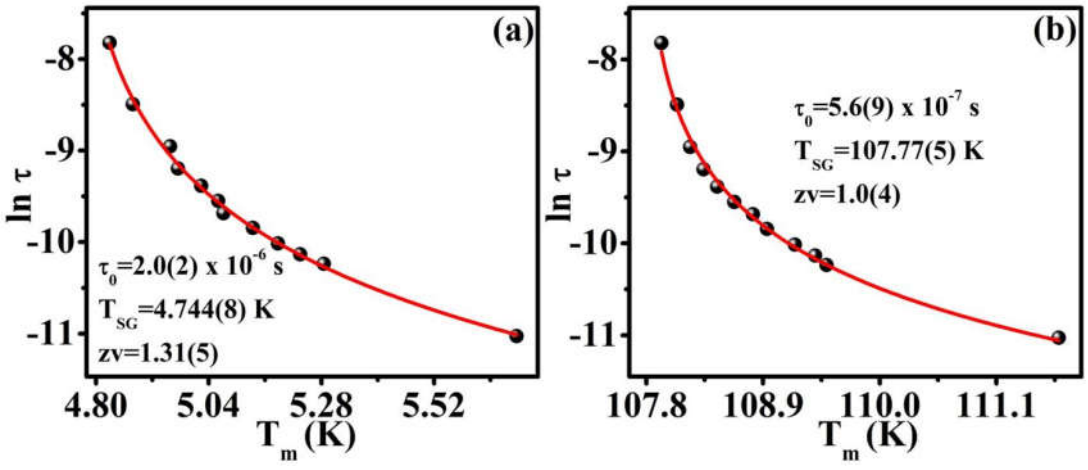

Figure 5.6 ln τ vs. T_m plot along with the fit to the critical power law for (a) transition near 5 K and (b) transition near 110 K

To confirm the spin glass phase, the ZFC memory experiment was performed by following the ZFC protocol. During ZFC cooling from 300 K, the sample was subjected to a wait time of 7200 s at 75 K and cooled further to 2 K. A field of H=100 Oe was applied and the magnetization was measured upon warming. This was incorporated with ZFC M vs. T without a wait time (reference curve), and the difference $\Delta M_{ZFC}=M_{ZFC}-M_{ZFCMem}$ is plotted as shown in figure 5.7 (a). A feeble effect around 78 K was observed in ΔM_{ZFC} as shown. In order to confirm if the effect stems from aging, we further carried out time dependent magnetization measurement with ZFC aging protocol.

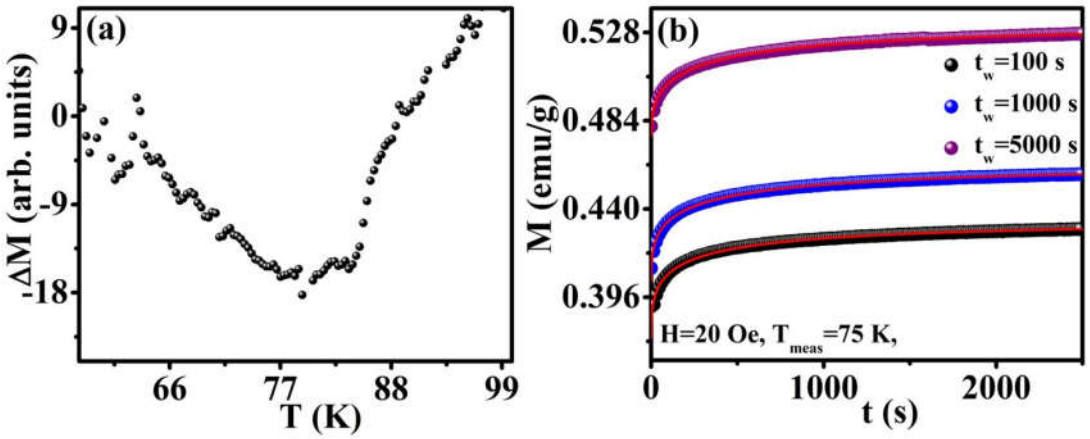

Figure 5.7 (a) The variation of ΔM as a function of temperature. (b) Time evolution of ZFC magnetic moment measured at H=20 Oe, T_{meas}=2 K, and t_w=100 s, 1000 s, and 5000 s. Solid red lines are the best fit to the stretched exponential function.

Table 5.2. The parameters obtained after the mathematical fitting of the time-dependent ZFC magnetization by using the stretched exponential function.

75 K, 20 Oe				
t_w (s)	**M_0 (emu/g)**	**M_{rel} (emu/g)**	**τ_{rel} (s)**	**β**
100	0.43374(3)	0.0579(3)	181.7(16)	0.383(1)
1000	0.46162(3)	0.0573(1)	228.1(10)	0.395(1)
5000	0.53129(5)	0.0546(1)	278.6(12)	0.430(1)

During the aging experiment, the system was initially cooled from 300 K to the measuring temperature T_{meas} = 75 K. After the respective waiting time of t_w (100 s, 1000 s, and 5000 s) at T_{meas}, a dc field of 20 Oe was applied and the time evolution of the magnetic moment was recorded as shown in figure 5.7 (b). A stretched exponential function of the form $M(t) = M_0 - M_{rel} exp\left\{(-t/\tau_{rel})^{\beta}\right\}$ is used to fit the time-dependent magnetization data, where M_0 is the intrinsic FM component, M_{rel} is the glassy component, τ_{rel} is the characteristic relaxation time,

and β is the stretching parameter [45-47]. The various parameters obtained after fitting are tabulated in Table 5.2. M_0 and τ_{rel} are increasing, and M_{rel} is decreasing with t_w. The β shows a small increase with t_w where its value β ≈0.4 lies in the range reported for many spin glass systems [45, 48]. In this case, β is less than 1, which implies that multiple anisotropy barriers are distributed in the system and is a typical characteristic of spin glass state [45, 47, 49].

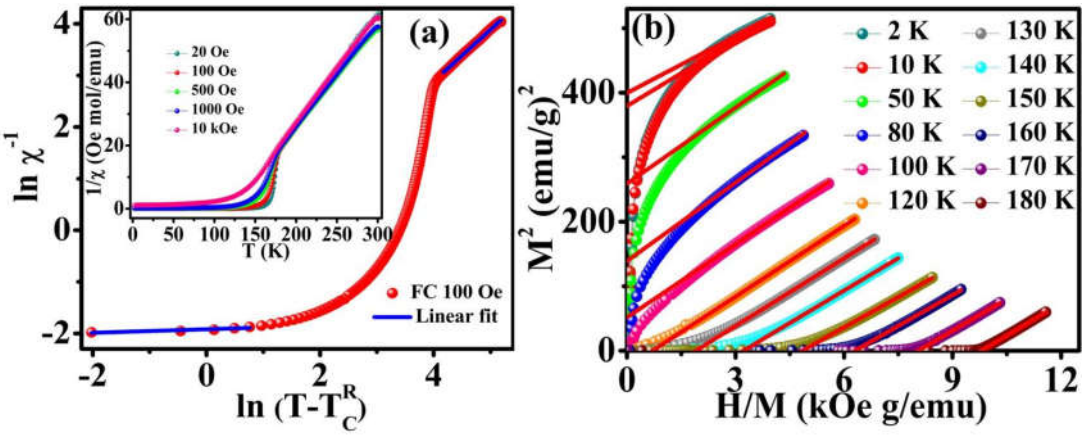

Figure 5.8 (a) ln (χ^{-1}) vs. ln ($T-T_C^R$) at 100 Oe with the linear fit (solid blue line). Inset of (a) showing the CW fit (solid blue line) on 1/χ (T) for FC at 100 Oe. (b) M^2 vs. H/M plot above and below T_C.

The deviation of inverse susceptibility from the CW law as a downturn is gradually decreased by increasing the magnetic field as shown in the inset of figure 5.8 (a). It is a characteristic feature of the GP. The susceptibility of a GP follows the power law in low fields, [9-19] as $\chi^{-1} \propto (T - T_C^R)^{1-\lambda}$, where T_C^R is the random critical temperature and λ is the magnetic susceptibility exponent ($0 \le \lambda \le 1$). For a GP the λ value is close to one, and the λ value is close to zero for a PM. Assuming the T_C^R as equal to 122 K, the value of Θ obtained from CW law; a good estimate for the λ_{PM} is obtained. The GP analysis is shown in figure 5.8 (a) which gives

λ_{PM}=0.0017(9) and λ_{GP} =0.966(1). The M^2 vs. H/M plot for temperatures above and below the observed T_C is shown in figure 5.8 (b). It can be seen that the linear fit to the high field region of the M^2 vs. H/M plot gives negative M^2-axis intercept above T_C. It implies the absence of a spontaneous magnetization even though the material is showing the magnetic hysteresis loop above T_C=115 K, which further confirms the presence of GP [18, 19]. The manganites are likely to show GP since the hybridization between Mn 3d and O 2p orbitals and the J-T distortion associated with the Mn^{3+} cations plays an important role in the occurrence of GP [10-12, 14, 15, 17-19, 50]. The strong magnetic inhomogeneities observed in La_2CrMnO_6 can be attributed to the disorder, arising from strong structural distortion associated with the *Pbnm* crystal structure and the mixed valence cations [51]. The presence of quenched disorder, the J-T distortion and the hopping of carriers during a FM double exchange interaction has crucial role in the occurrence of GP [51]. Mixed valence manganites with quenched disorder are well known to exhibit a GP [12, 14, 17-19, 23, 50-53]. The R-3c structured La_2CrMnO_6 without a J-T distortion has no signal of a GP in the inverse susceptibility plot as reported by Barrozo *et al.* [37] Also, the irregularity observed at 60 K (figure 5.3 (b)) is not visible in their reports [37]. The FC and ZFC bifurcation temperature is 140 K in the reports[37] whereas it is 170 K in the present work. This means that the rhombohedral structure without a J-T distortion has washed-out the low-temperature magnetic inhomogeneities[37] while the disordered *Pbnm* structure and the J-T distortion of the present sample introduced a GP. La_2CrMnO_6 with a *Pbnm* structure as reported by Singh *et al.* demonstrated a deviation near 200 K in the inverse susceptibility vs. T plot [29]. Numerous exchange interactions are possible within the system due to disorder and

presence of four different transition element cations. Though a clear distinction between these interactions is not possible, the present experiments indicate ferromagnetic, spin glass, and Griffiths-like phases within La_2CrMnO_6.

5.3.3 Specific Heat, dc resistivity, and magnetoresistance

The specific heat (C) for temperatures 2-300 K is measured, and the C/T vs. T plot is shown in figure 5.9 (a). The C/T shows a kink around 11 K and deviates the direction of C/T vs. T beyond this point. The C/T grows fast till T_{C1}=56 K, and then it slows down. After reaching the maximum value at 135 K, the C/T value decreases. The low-temperature C can be fitted by using the equation $C=\gamma T+\beta_3 T^3+\beta_5 T^5+\beta_7 T^7$ where γT is the electronic specific heat, and the higher order T terms are contributions arising from lattice/phonons [54]. The fitting of the low-temperature C data by including a magnetic contribution (δT^n term where n=3/2 or 2) produced erroneous results. There are few reports suspicious about the presence of spin waves in manganites and hence eliminated non-zero values of δ for many of such systems [19, 54-57]. The values obtained after fitting the C for 2-78 K (inset of figure 5.9 (a)) are γ=64.8(86) $mJmol^{-1}K^{-2}$ for the linear term, β_3=0.398(10) $mJmol^{-1}K^{-4}$, β_5=-8.15(35)x10^{-5} $mJmol^{-1}K^{-6}$, and β_7=5.91(35)x10^{-9} $mJmol^{-1}K^{-8}$. The high value of γ is an indication of the presence of FM phase with localized charge carriers [57, 58]. The C/T does not show an anomaly at any of the observed magnetic transitions due to the presence of inherent magnetic inhomogeneities and short-range order [57, 59].

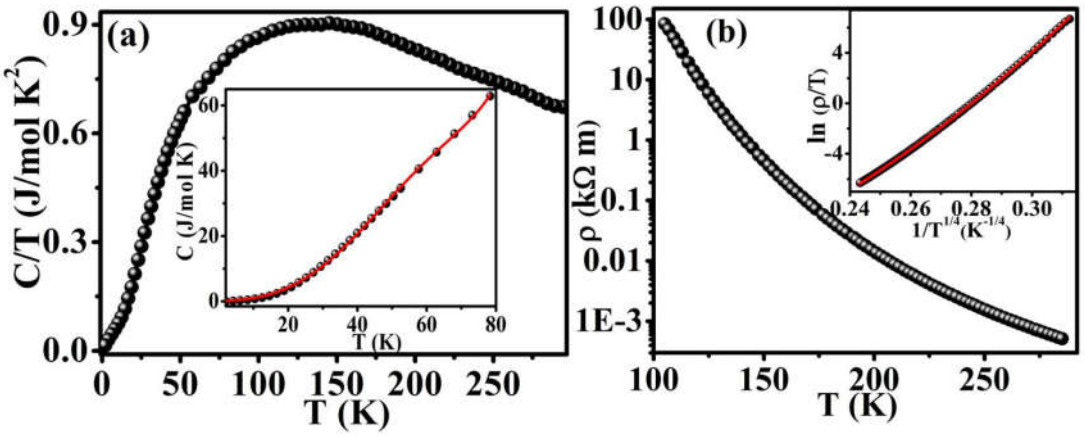

Figure 5.9 (a) Temperature dependence of specific heat (C/T) vs. T plot. The inset is showing the specific heat fit for the low-temperature region (2-78 K). (b) Temperature dependence of resistivity (ρ). Inset is showing the ln (ρ/T) vs. $1/T^{1/4}$ plot with the red solid curve showing the nonlinear fit for SP-VRH model.

The dc resistivity (ρ) as a function of temperature from 103-287 K is plotted in figure 5.9 (b). The ρ has a value of 0.5 Ωm near the room temperature which is increased on cooling and reaches 10^5 Ωm at 103 K. The mechanisms that govern the ρ in insulators and semiconductors are Mott's variable range hopping (VRH) and nearest neighbor hopping of small polarons (NNSPH). In the present study, ρ follows a combination of the two mechanisms as variable range hopping of small polarons (VR-SPH). In this VR-SPH, the small polarons are thermally activated into an intermediate state and hop to proper sites with modest energy differences as per the random potential fluctuation induced by the electric or magnetic disorder [60, 61]. The combined equation for the VR-SPH is $\rho = BT\exp\left(\frac{E_A}{k_B T} + \left(\frac{T_0}{T}\right)^{1/4}\right)$ where B and T_0 are temperature-independent terms; E_A is the activation energy, k_B is the Boltzmann constant [61]. The nonlinear curve fit to the ln (ρ/T) vs. $1/T^{1/4}$ plot by

using the VR-SPH equation is shown in the inset of figure 5.9 (b). The obtained value of E_A after the fitting is 0.1045(6) eV.

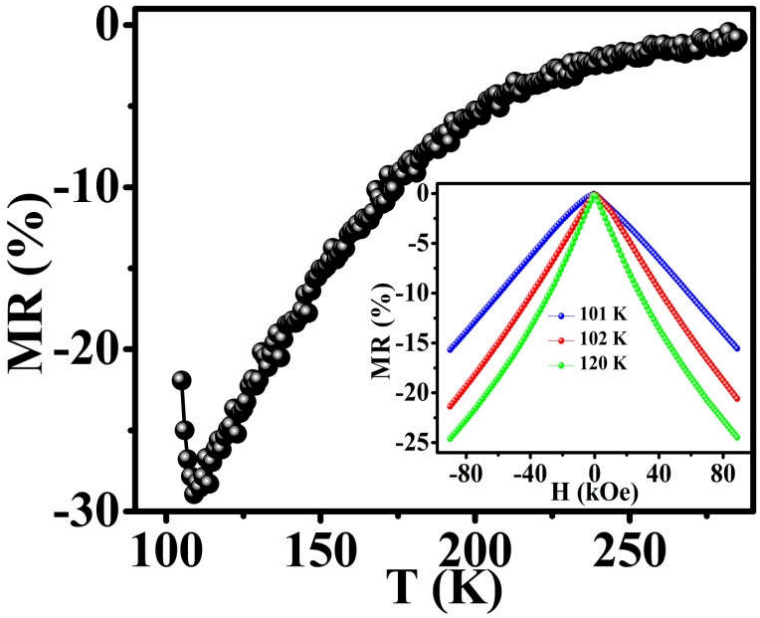

Figure 5.10 Magnetoresistance as a function of (a) temperature at 90 kOe (b) magnetic field at 101 K, 102 K, and 120 K.

The MR is calculated by the equation MR (%)=$(\rho_H-\rho_0)/\rho_0$ x 100, where ρ_H is the value of ρ at the magnetic field (H) and ρ_0 is the value of ρ at zero magnetic fields. The MR is calculated for temperatures 105-285 K with a magnetic field of 90 kOe as shown in figure 5.10. The temperature-dependent MR shows an anomaly in the neighborhood of T_C. It shows a negative MR of 22% at 105 K which slowly increases and reaches the maximum of 29 % at a temperature near 110 K. Above this point, the negative MR show decrease with increasing temperature and gradually becomes negligible. A significant MR is observed below the T*, indicating the strong correlation between the spin and charge degrees of freedom. The field variation of MR at 101 K, 102 K, and 120 K are shown in the inset of figure 5.10. For all the temperatures, the negative MR is linearly increasing with a

magnetic field. Further, the significant negative MR observed below T* is almost linearly increasing till 110 K. These point to a spin-dependent disorder scattering mechanism in La_2CrMnO_6. [3, 62] The observation of MR in a material has different origin; likewise, the GP has also claimed its role in the occurrence of MR in many manganite systems [4, 6, 21-24]. However there is a report claiming that GP is not a prerequisite for the occurrence of colossal MR in manganites [10]. In the present work, we experimentally observed the simultaneous existence of a GP and significant MR below the Griffiths-temperature T*.

5.4 Conclusion

In summary, La_2CrMnO_6 is synthesized with orthorhombic *Pbnm* crystal structure with a distorted perovskite structure and mixed valence cations Cr^{3+}, Cr^{2+}, Mn^{3+}, and Mn^{4+}. Multiple magnetic transitions due to the various competing magnetic interactions are found. Transitions at T_{C1}=56 K and T_C=115 K are observed from the DC magnetic measurements. A GP with FM short range correlations is identified with Griffiths temperature T*=180 K. The effective moment is observed as 4.916(3) μ_B / f.u., that suggest the competing exchange interactions among Cr^{3+} and Mn^{3+} as well as between Cr^{2+} and Mn^{4+}. Multiple transitions with FM ordering at 32 K and 56 K along with spin glass transitions at 4.744(8) K and 107.77(5) K are observed from the AC magnetic measurements. The dc transport mechanism follows the variable range hopping of small polarons. The spin-dependent disorder scattering induces significant MR in La_2CrMnO_6 below T*. A negative MR of 22% at 105 K is identified that increases to 29 % at temperatures near 110 K.

5.5 References

[1] E. Dagotto, Science, 309 (2005) 257-262.

[2] J. Varignon, N.C. Bristowe, E. Bousquet, P. Ghosez, Scientific Reports, 5 (2015) 15364.

[3] C.N.R. Rao, B. Raveau, Colossal Magnetoresistance, Charge Ordering and Related Properties of Manganese Oxides, World Scientific, 1998.

[4] P.K. Siwach, H.K. Singh, O.N. Srivastava, Journal of Physics: Condensed Matter, 20 (2008) 273201.

[5] M. Mayr, A. Moreo, J.A. Vergés, J. Arispe, A. Feiguin, E. Dagotto, Physical Review Letters, 86 (2001) 135-138.

[6] M.B. Salamon, S.H. Chun, Physical Review B, 68 (2003) 014411.

[7] A.K. Kundu, R. Ranjith, V. Pralong, V. Caignaert, B. Raveau, Journal of Materials Chemistry, 18 (2008) 4280-4285.

[8] R.B. Griffiths, Physical Review Letters, 23 (1969) 17-19.

[9] C. Magen, P.A. Algarabel, L. Morellon, J.P. Araújo, C. Ritter, M.R. Ibarra, A.M. Pereira, J.B. Sousa, Physical Review Letters, 96 (2006) 167201.

[10] W. Jiang, X. Zhou, G. Williams, Y. Mukovskii, K. Glazyrin, Physical Review Letters, 99 (2007) 177203.

[11] P. Tong, B. Kim, D. Kwon, T. Qian, S.-I. Lee, S.W. Cheong, B.G. Kim, Physical Review B, 77 (2008) 184432.

[12] W. Jiang, X. Zhou, G. Williams, Y. Mukovskii, K. Glazyrin, Physical Review B, 77 (2008) 064424.

[13] S. Guo, D.P. Young, R.T. Macaluso, D.A. Browne, N.L. Henderson, J.Y. Chan, L.L. Henry, J.F. DiTusa, Physical Review Letters, 100 (2008) 017209.

[14] S. Zhou, Y. Guo, J. Zhao, L. He, L. Shi, The Journal of Physical Chemistry C, 115 (2011) 1535-1540.

[15] A.K. Pramanik, A. Banerjee, Physical Review B, 81 (2010) 024431.

[16] A. Ślebarski, J. Goraus, M. Fijałkowski, Physical Review B, 84 (2011) 075154.

[17] D. Bhoi, N. Khan, A. Midya, M. Nandi, A. Hassen, P. Choudhury, P. Mandal, The Journal of Physical Chemistry C, 117 (2013) 16658-16664.

[18] J. Pezhumkattil Palakkal, P.N. Lekshmi, S. Thomas, K.G. Suresh, M.R. Varma, RSC Advances, 5 (2015) 105531-105536.

[19] H.S. Nair, D. Swain, H. N., S. Adiga, C. Narayana, S. Elzabeth, Journal of Applied Physics, 110 (2011) 123919.

[20] A.H. Castro Neto, G. Castilla, B.A. Jones, Physical Review Letters, 81 (1998) 3531-3534.

[21] M.B. Salamon, P. Lin, S.H. Chun, Physical Review Letters, 88 (2002) 197203.

[22] G.N. Rao, J.W. Chen, S. Neeleshwar, Y.Y. Chen, M.K. Wu, Journal of Physics D: Applied Physics, 42 (2009) 095003.

[23] J. Wanjun, Z. XueZhi, W. Gwyn, Y. Mukovskii, R. Privezentsev, Journal of Physics: Condensed Matter, 21 (2009) 415603.

[24] V.N. Krivoruchko, M.A. Marchenko, Y. Melikhov, Physical Review B, 82 (2010) 064419.

[25] B. Toby, Journal of Applied Crystallography, 34 (2001) 210-213.

[26] P. Ganguly, Bulletin of Materials Science, 3 (1981) 255-260.

[27] M. HROVAT , S. BERNIK, J. HOLC , D. KUSCER , D. KOLAR Journal of Materials Science Letters, 16 (1997) 143-146.

[28] N.X. Dung, Journal of Experimental Nanoscience, 10 (2015) 511-519.

[29] D. Singh, A. Mahajan, Journal of Alloys and Compounds, 644 (2015) 172-179.

[30] S. Estemirova, A. Fetisov, V. Balakirev, S. Titova, Journal of Superconductivity and Novel Magnetism, 20 (2007) 113-116.

[31] V. Cuartero, J. Blasco, J. García, J.A. Rodríguez-Velamazán, C. Ritter, EPJ Web of Conferences, 40 (2013) 15002.

[32] D.G. Franco, R.E. Carbonio, G. Nieva, IEEE Transactions on Magnetics, 49 (2013) 4594-4597.

[33] N. Uekawa, K. Kaneko, The Journal of Physical Chemistry, 100 (1996) 4193-4198.

[34] R. Merryfield, M. McDaniel, G. Parks, Journal of Catalysis, 77 (1982) 348-359.

[35] N.N.A. Ivanov-Emin B.N., Zaitsev B.E., Ivanova T.M., Zh. Neorg. Khimii 27 (1982) 2.

[36] Y. Umezawa, C.N. Reilley, Analytical Chemistry, 50 (1978) 1290-1295.

[37] P. Barrozo, J. Albino Aguiar, Journal of Applied Physics, 113 (2013) 17E309.

[38] T.-J. Park, G.C. Papaefthymiou, A.J. Viescas, Y. Lee, H. Zhou, S.S. Wong, Physical Review B, 82 (2010) 024431.

[39] O. Kubo, T. Ido, H. Yokoyama, IEEE Transactions on Magnetics, 18 (1982) 1122-1124.

[40] B. Ruette, S. Zvyagin, A.P. Pyatakov, A. Bush, J.F. Li, V.I. Belotelov, A.K. Zvezdin, D. Viehland, Physical Review B, 69 (2004) 064114.

[41] A.K. Nayak, R. Sahoo, K.G. Suresh, A.K. Nigam, X. Chen, R.V. Ramanujan, Applied Physics Letters, 98 (2011) 232502.

[42] J. Kanamori, Journal of Physics and Chemistry of Solids, 10 (1959) 87-98.

[43] P.N. Lekshmi, G.R. Raji, M. Vasundhara, M.R. Varma, S.S. Pillai, M. Valant, Journal of Materials Chemistry C, 1 (2013) 6565-6574.

[44] P.C. Hohenberg, B.I. Halperin, Reviews of Modern Physics, 49 (1977) 435-479.

[45] N. Khan, P. Mandal, D. Prabhakaran, Physical Review B, 90 (2014) 024421.

[46] T. Chakrabarty, A.V. Mahajan, S. Kundu, Journal of Physics: Condensed Matter, 26 (2014) 405601.

[47] S. Sarkar, A. Mondal, K. Dey, R. Ray, RSC Advances, 5 (2015) 81260-81265.

[48] D. Chu, G.G. Kenning, R. Orbach, Physical Review Letters, 72 (1994) 3270-3273.

[49] H. Khurshid, P. Lampen-Kelley, Ò. Iglesias, J. Alonso, M.-H. Phan, C.-J. Sun, M.-L. Saboungi, H. Srikanth, 5 (2015) 15054.

[50] Z. Hong-guang, S. Jiang-jian, L. Yong-tao, D. Xue-guang, G. Xiao-peng, L. Hao, H. Qing-teng, L. Qi, T. Yan-kun, Journal of Physics: Condensed Matter, 26 (2014) 145601.

[51] A. Karmakar, S. Majumdar, S. Kundu, T.K. Nath, S. Giri, Journal of Physics: Condensed Matter, 25 (2013) 066006.

[52] V. Markovich, R. Puzniak, I. Fita, A. Wisniewski, D. Mogilyansky, B. Dolgin, G. Gorodetsky, G. Jung, Journal of Applied Physics, 113 (2013) 233911.

[53] S.K. Giri, S.M. Yusuf, M.D. Mukadam, T.K. Nath, Journal of Alloys and Compounds, 591 (2014) 181-187.

[54] M.R. Lees, O.A. Petrenko, G. Balakrishnan, D. McK. Paul, Physical Review B, 59 (1999) 1298-1303.

[55] J.J. Hamilton, E.L. Keatley, H.L. Ju, A.K. Raychaudhuri, V.N. Smolyaninova, R.L. Greene, Physical Review B, 54 (1996) 14926-14929.

[56] T. Kyômen, R. Yamazaki, M. Itoh, Physical Review B, 68 (2003) 104416.

[57] C.L. Lu, K.F. Wang, S. Dong, J.G. Wan, J.-M. Liu, Z.F. Ren, Journal of Applied Physics, 103 (2008) 07F714.

[58] R.K. Zheng, A.N. Tang, Y. Yang, W. Wang, G. Li, X.G. Li, H.C. Ku, Journal of Applied Physics, 94 (2003) 514-518.

[59] L. Jia, G.J. Liu, J.Z. Wang, J.R. Sun, H.W. Zhang, B.G. Shen, Applied Physics Letters, 89 (2006) 122515.

[60] J. Pezhumkattil Palakkal, P.N. Lekshmi, S. Thomas, M. Valant, K.G. Suresh, M.R. Varma, Materials Research Bulletin, 76 (2016) 161-168.

[61] S. Young, X. Xiaojun, Z. Yuheng, Journal of Physics: Condensed Matter, 12 (2000) 10475.

[62] J.K. Murthy, K.D. Chandrasekhar, S. Murugavel, A. Venimadhav, Journal of Materials Chemistry C, 3 (2015) 836-843.

Chapter 6

Conclusion and scope of future works

This chapter concludes the thesis and gives a summary of the results described in the previous chapters. The significant observations of the investigation are highlighted. Also, the scopes of the future investigations are described.

6.1 Conclusion

In summary, the perovskites La_2FeMnO_6, La_2CuMnO_6, and La_2CrMnO_6 were synthesized. The structural, magnetic, transport and magnetotransport properties of the materials were studied in detail. The significant results are as follows.

6.1.1 High-temperature magnetic transition and existence of positive and negative magnetodielectric coupling in La_2FeMnO_6

- La_2FeMnO_6 is synthesized by combustion of citrate-nitrate gel. The material sintered at 900 ºC has an orthorhombic *Pbnm* crystal structure with unit cell parameters a= 5.5141(1) Å, b= 5.5398(4) Å, c= 7.8122(3) Å, and α, β, γ = 90° along with Fe^{3+} and Mn^{3+} cations.
- When sintered at 1000 ºC, La_2FeMnO_6 has an orthorhombic *Pbnm* crystal structure with unit cell parameters *a*=5.5082(2) Å, *b*=5.5413(2) Å, c=7.8092(3) Å, α=β=γ=90º along with Fe^{3+}, Fe^{2+}, Mn^{3+} and Mn^{4+} cations.
- It has a J-T distortion $\Delta d = 8.8 \times 10^{-4}$ and angle distortions $\langle\omega_1\rangle$=18.2, $\langle\omega_2\rangle$=18.0, and in average $\langle\omega\rangle$=18.1
- It shows two magnetic transitions at T_{C1}=60 K and T_C=425 K
- It possesses a Griffiths-like phase with T*=570 K and T_C^R = 18 K
- The material has a spin glass state at lower temperatures
- The resistivity value is 1388 Ω m near room temperature
- It possess a charge localization at temperatures near T_{CL}~133 K

- Below T_{CL}, a combination of variable range hopping and small polaron hopping conduction mechanism exists.
- Above T_{CL}, the small polaron hopping mechanism is the conduction mechanism.
- The low temperature specific heat gives the parameters γ=59.5 $mJmol^{-1}K^{-2}$ for the linear term, β_3=0.694 $mJmol^{-1}K^{-4}$, β_5=-2.54x10^{-4} $mJmol^{-1}K^{-6}$ and β_7=3.69x10^{-8} $mJmol^{-1}K^{-8}$.
- Double dielectric relaxation are present
- The charge localization splits the magnetodielectric coupling as positive and negative
- Large MD coupling values of +4.5% at ~80 K, +45% at ~122 K, -18% at ~147 K, and -6.8% at ~284 K are established through a cooperative effect from charge ordering phenomenon, spin glass property, and dielectric relaxation behavior.

6.1.2 Unusual magnetodielectric effects in frustrated ferromagnetic perovskite La_2CuMnO_6

- La_2CuMnO_6 was synthesized by combustion of citrate/acetate-nitrate gel. It has an orthorhombic *Pbnm* crystal structure with unit cell parameters a=5.5149(3) Å, b=5.4706(3) Å, c=7.7543(4) Å, and $\alpha=\beta=\gamma=90^o$ along with Cu^{2+} and Mn^{4+} cations
- It has a J-T distortion Δd =9.47x10^{-3} and angle distortions $\langle\omega_1\rangle$=23.54º and $\langle\omega_2\rangle$=10.45º with an average $\langle\omega\rangle$=16.99º

- Combined AFM and FM interactions are existing in La_2CuMnO_6 below T_C=72 K and T_N=5 K
- It possesses a Griffiths-like phase with T^*=115 K and T_C^R=27 K
- The low temperature specific heat gives the parameters γ=230 $mJmol^{-1}K^{-2}$ for the linear term, β_3=0.403 $mJmol^{-1}K^{-4}$, β_5=-8.3x10^{-5} $mJmol^{-1}K^{-6}$ and β_7=5.96x10^{-9} $mJmol^{-1}K^{-8}$
- The resistivity has a value of 67x10^{-3} Ω m at room temperature
- The conduction mechanism in the material follows the VRH model.
- The material shows a dynamic Arrhenius to Arrhenius crossover in the relaxation phenomena around the T_C due to the existence of GP and magnetic ordering.
- Just above T_C, the Maxwell-Wagner effect along with a contribution from Debye relaxation occurs while the Maxwell-Wagner relaxation dominates for low frequency below T_C.
- A different trend is observed for the variation of maximum MD coupling with respect to the dynamic crossover around T_C.
- A maximum MD of 55% is observed at 67 K for 4 kHz, and 61% is observed at 105 K for 285.8 kHz.
- A negative MDL is observed corresponding to a positive MD and a positive MDL is observed corresponding to a low value of MD. The origin of MD in La_2CuMnO_6 is correlated to the presence of FM short-range correlations, and the influence of a core grain dominated MR on Maxwell-Wagner interfacial

polarization. The magnetic ordering and the external magnetic field have control over the electric dipole relaxations in the material.

6.1.3 Multiple magnetic transitions, Griffiths-like phase, and Magnetoresistance in La_2CrMnO_6

- La_2CrMnO_6 was synthesized by combustion of citrate-nitrate gel. It has an orthorhombic *Pbnm* crystal structure with unit cell parameters a= 5.5130(3) Å, b= 5.4752(3) Å, c= 7.7601(4) Å, and α=β=γ=90º along with Cr^{3+} , $Cr^{2+,}$ Mn^{3+} and Mn^{4+} cations
- It has a J-T distortion Δd =4.34x10^{-3} and angle distortions $\langle\omega\rangle = 180^{\circ} - \langle\theta\rangle$ as $\langle\omega_1\rangle$=23.5º and $\langle\omega_2\rangle$=14.5º with average $\langle\omega\rangle$=19º
- Transitions at T_{C1}=56 K and T_C=115 K are observed from the DC magnetic measurements.
- It possesses a Griffiths-like phase with T^*=180 K and T_C^R=122 K
- Multiple transitions with FM-like ordering at 32 K and 56 K along with spin glass transitions at 4.74 K and 107.77 K are observed from the AC magnetic measurements.
- The low temperature specific heat gives the parameters γ=64.82 mJmol^{-1}K^{-2} for the linear term, β_3=0.398 mJmol^{-1}K^{-4}, β_5=-8.15x10^{-5} mJmol^{-1}K^{-6}, and β_7=5.91x10^{-9} mJmol^{-1}K^{-8}.
- The resistivity has a value of 0.5 Ωm at room temperature
- The dc transport mechanism follows the variable range hopping of small polarons.

- The spin-dependent disorder scattering induces significant MR in La_2CrMnO_6 below T*. A negative MR of 22% at 105 K is identified that increases to 29 % at temperatures near to 110 K.

Table 6.1. Important results obtained for La_2BMnO_6 (B=Fe, Cu, and Cr)

	La_2FeMnO_6	**La_2CuMnO_6**	**La_2CrMnO_6**
Structure	*Pbnm*	*Pbnm*	*Pbnm*
Cations	Mixed Valance	Single Valance	Mixed Valance
Magnetism	FM (60 K, T_C=425 K)	FM (12 K, T_C=72 K)	FM ~ 32 K, 56 K, T_C = 115 K
Charge Ordering / Localization	133 K	No	No
Resistivity Mechanism	$T<T_{CL}$, VRH+SPH $T>T_{CL}$, SPH	VRH	VR-SPH
Spin Glass	Yes	No	Yes
GP	Yes	Yes	Yes
Dielectric relaxation	Double Arrhenius	Single Different E_A - T_C	--
MD/MR	MD at multiple regions	MD around T_C	MR around T_C

All the three materials synthesized are having *Pbnm* crystal symmetry. They possess a J-T ion and subsequently possess structural distortions and angle distortions. La_2FeMnO_6 and La_2CuMnO_6 are exhibiting magnetodielectric property whereas La_2CrMnO_6 is showing magnetoresistance. All the three materials possess the Griffiths-like phase. The random critical temperatures for La_2FeMnO_6 and La_2CuMnO_6 are below the observed T_C while that of La_2CrMnO_6 is above the T_C. Main results are tabulated in Table 6.1.

6.2 Scope of future works

- Further characterization of these materials by using Neutron diffraction is required to understand the exact magnetic interaction at lower temperatures.
- The nano sized double perovskites can be prepared with different the size and grain distribution. Analyzing the particle size - property relationship of the nano double perovskites will be interesting.
- Fabrication and characterization of double perovskite thin films for the development of devices.
- Novel double perovskite structures can be synthesized with various A and B, B’ atoms and the basic mechanism behind the properties can be analyzed.
- As a preliminary step towards the future studies, some more double perovskites are sythesized with different A, B and B' cations. Three of them are listed in appendices A and B.

Magnetism and transport properties of ordered double perovskite Ba_2FeWO_6

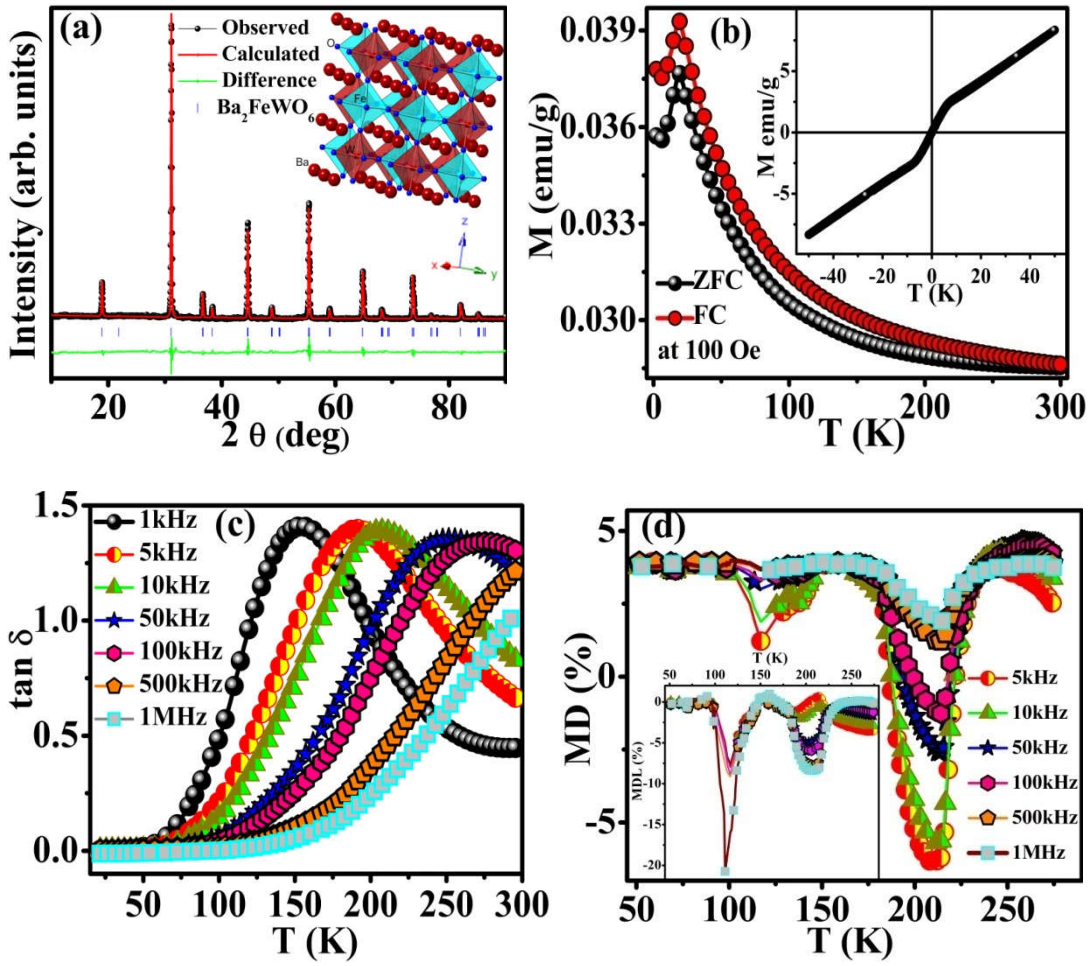

Figure A.1 (a) Observed, calculated and the difference XRD pattern of Ba_2FeWO_6 obtained from Rietveld refinement. The bar marks represent the possible Bragg reflections. Inset: The crystallographic structure framed using CrystalMaker® (b) The ZFC and FC M(T) at 100 Oe. Inset showing the isothermal magnetization at 2 K (c) tan δ vs T at various frequencies (d) Percentage MD vs. T at different frequencies. Inset showing percentage MDL vs. T at different frequencies.

- The ordered double perovskite Ba_2FeWO_6 is synthesized in a highly controlled reducing atmosphere (H_2:Ar gas) with tetragonal *I 4/m* crystal structure

- The material is antiferromagnetic with transition T_N at 19 K
- Dielectric relaxation is observed
- A small intrinsic MD coupling of 4% is observed which changes to -6.3% around 210 K.

Magnetism and magnetoresistance in $La_2B'NiO_6$ (B'=Co, & Al)

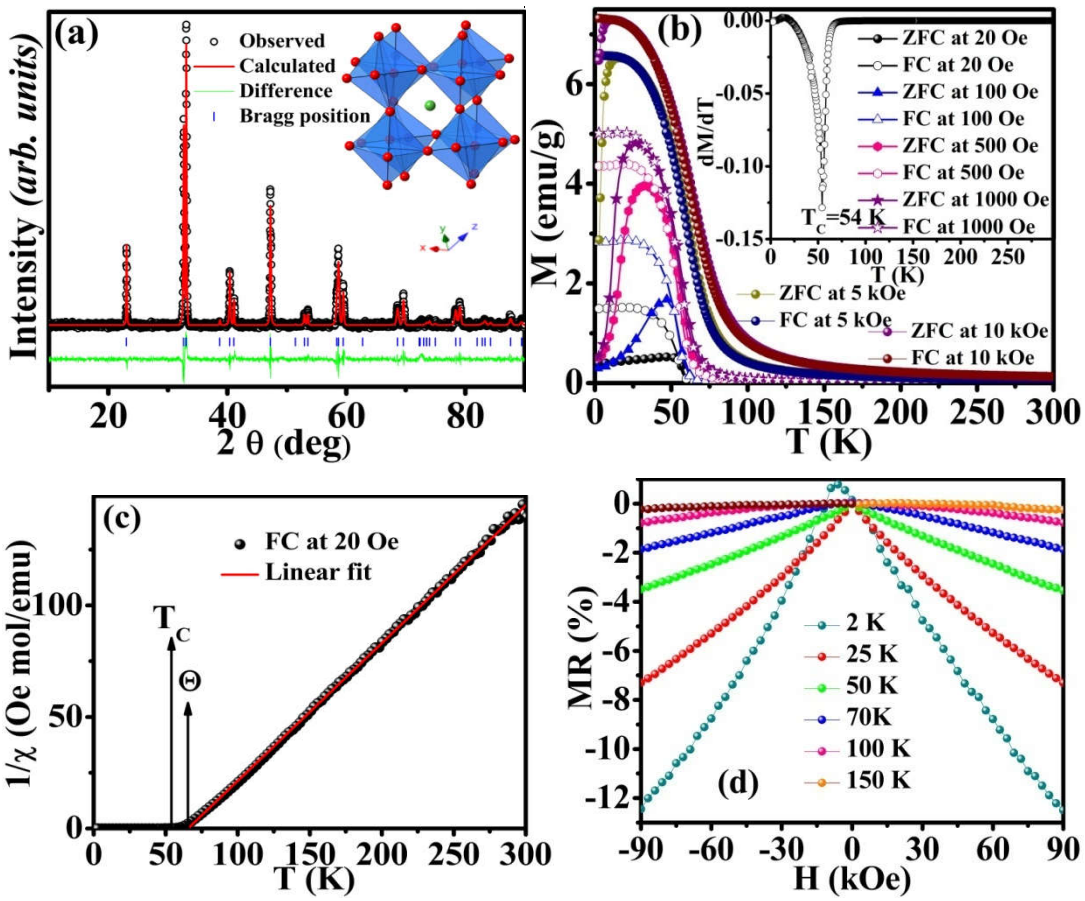

Figure B.1 (a) Observed, calculated and the difference XRD pattern of La_2CoNiO_6 obtained from Rietveld refinement. The bar marks represent the possible Bragg reflections. Inset showing the crystallographic structure framed using CrystalMaker® (b) The ZFC and FC M(T) at various magnetic fields. Inset showing dM/dT vs. T plot (c) inverse susceptibility vs. T along with the C-W linear fit (d) Magnetoresistance as a function of magnetic field at various temperatures.

- The double perovskite La_2CoNiO_6 is synthesized by combustion of nitrate-citrate gel. The crystal structure is trigonal *R-3cH*.
- The material is having a ferromagnetic transition at T_C=54 K

- Unlike the La_2BMnO_6 compounds, La_2CoNiO_6 is not showing any Griffiths-like phase. The values of T_C and Θ are almost same.

- Negative magnetoresistance of 12 % is observed at 2 K for 90 kOe.

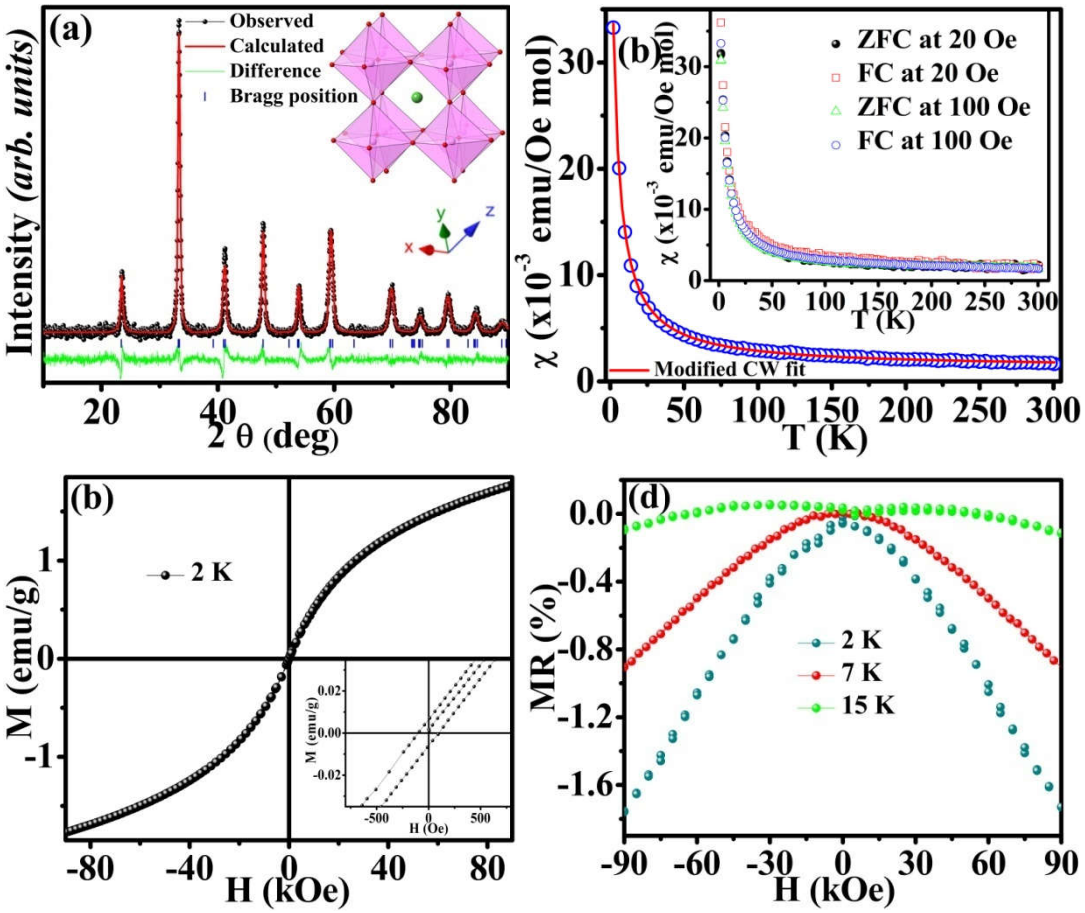

Figure B.2 (a) Observed, calculated and the difference XRD pattern of La_2AlNiO_6 obtained from Rietveld refinement. The bar marks represent the possible Bragg reflections. Inset showing the crystallographic structure framed using CrystalMaker® (b) FC DC susceptibility vs. temperature plot along with the modified CW fit at 100 Oe. Inset showing the ZFC and FC DC susceptibility vs. temperature at 20 Oe and 100 Oe (c) Magnetic hysteresis loop at 2 K. Inset is showing the zoomed center portion (d) Magnetoresistance as a function of magnetic field at various temperatures.

- The double perovskite La_2AlNiO_6 is synthesized by combustion of nitrate-citrate gel. The crystal structure is trigonal *R-3cH*.
- The material is having small magnetic correlations at low temperatures. The susceptibility is fitted by the modified Curie-Weiss law with Θ=-3.2 K.
- The material is having small coercivity H_C=108 Oe at 2 K.
- A small negative magnetoresistance of 1.75 % is observed at 2 K for 90 kOe.

Further studies are necessary to get the exact reason behind the observed magnetoresistance in the $La_2B'NiO_6$ (B'=Co, & Al) perovskites. Also, the absence of a Griffiths-like phase in the La_2CoNiO_6 is observed while La_2BMnO_6 (B=Ni, Co, Fe, Cu, and Cr) exhibit the GP. So, the relationship between the presence of the Mn or a Jahn-Teller ion and the existence of a GP should also be closely analyzed.

List of Publications (Thesis)

1. '*Observation of high-temperature magnetic transition and existence of ferromagnetic short-range correlations above transition in double perovskite* La_2FeMnO_6, **Jasnamol P Palakkal**, P. N. Lekshmi, S. Thomas, K. G. Suresh and M. R. Varma, **RSC Advances** 5 (128), 105531-105536 (2015).

2. *'Polarons induced electronic transport, dielectric relaxation and magnetodielectric coupling in spin frustrated* Ba_2FeWO_6, **Jasnamol P Palakkal**, P. N. Lekshmi, S. Thomas, M. Valant, K. G. Suresh and M. R. Varma, **Materials Research Bulletin** 76, 161-168 (2016).

3. *'Multiple magnetic transitions, Griffiths-like phase, and Magnetoresistance in* La_2CrMnO_6', **J P Palakkal,** C R Sankar and M R Varma, **Journal of Applied Physics**, 122 (7), 073907 (2017).

4. *'Hopping conduction and spin glass behavior of* La_2FeMnO_6', **J P Palakkal**, C R Sankar, A P Paulose, and M R Varma, **(under review).**

5. *'Unusual magnetodielectric effects in* La_2CuMnO_6 *induced by dynamic crossover in dielectric relaxation at* T_C', **J P Palakkal**, C R Sankar, A P Paulose, M Valant, A Badasyan, and M R Varma, **(under review).**

6. *'Large positive and negative magnetodielectric coupling in* $LaFe_{0.5}Mn_{0.5}O_3$', **J P Palakkal,** C R Sankar, P N Lekshmi, M Valant, M V Mihelj and M R Varma, **(communicated).**

7. *'Magnetic, transport and magnetotransport studies of La_2BNiO_6 (B = Fe and Al)'*, **J P Palakkal,** K Aswathi, C R Sankar and M R Varma, **(under preparation).**

List of Publications (Not related to thesis)

1. *'Memory and aging effects of molecular nanomagnet Mn_{12} benzoate'*, J **P Palakkal**, M R Varma, and C R Sankar, **AIP Conference proceedings, (accepted).**
2. *'Structural and Magnetic Properties of Multiferroic Y_2NiMnO_6 Double Perovskite'*, Aswathi K, **J P Palakkal**, A P Paulose, and M R Varma, **Ferroelectrics, (accepted).**
3. *'Griffiths-like phase in High T_C Perovskite La_2FeReO_6 prepared in a controlled reducing atmosphere'*, A Kaipamagalath, **J P Palakkal**, and M R Varma, **AIP Conference proceedings, (accepted).**
4. *'Dipolar interactions between molecular (nano)magnets causing super spin glass state in Mn_{12}-acetate'*, **J P Palakkal**, M Rijila, A P Paulose, and C R Sankar, **(under review).**
5. *'Impact of rare earth ion on the magnetic, magneto-dielectric and spin-phonon interactions in RE_2NiMnO_6 (RE = La, Sm, Tb)'*, P N Lekshmi, **J P Palakkal**, V Sathe, S Pillai, S Thomas, K G Suresh, M Valant, and M R Varma, **(under review).**

List of Conference Presentations

1. '*Structural, magneto-electric and transport properties of $Sr_2Fe_{1-x}Mn_xMoO_6$ (x=0, 0.25, 0.50, 0.75, 1.0)'*, **P. P. Jasnamol**, *et al.*; **poster** presented at 'IUMRS ICA 2013' international conference at IISc Bangalore, India; December 15-20.
2. '*Structural and magnetoelectric studies on $Sr_2Fe_{1-x}Mn_xMoO_6$ (x=0.0,0.25,0.50)*', **P.P. Jasnamol**, *et al.*; **poster** presented at 'ICRAPID 2014' international confernce at Sathyabama University, Chennai, India; January 23,24.
3. '*Structural and transport properties of $Ca_2Fe_{1-x}Mn_xMoO_6$ double perovskites synthesized in controlled reducing atmosphere*', **P. P. Jasnamol**, *et al.*; **poster** presented at 'ICAFM 2014' international conference at NIIST CSIR, Trivandrum, India; February 19-21.
4. 'Magnetic structure and transport properties of Ba_2FeWO_6 synthesized in ambient H_2: Ar gas', **P P Jasnamol** , *et al.*; **poster** presented at 'ICMAGMA 2014' international conference at Department of Physics, Pondicherry University, Pondicherry, India; September 15-17 2014.
5. '*Multiferroic double perovskite La_2FeMnO_6',* **Jasnamol P P**, *et al.;* **poster** presented at 'ICSTAR 2015' international conference, organized by Rare Earth Association of India (REAI) at Thiruvananthapuram, India during April 23rd-25th 2015.
6. *'Origin of Magnetodielectric Coupling in mixed B-site Perovskites: La_2FeMnO_6 and La_2CuMnO_6',* **Jasnamol P Palakkal**, *et al.;* **Oral** presentation at 'ICTAM-AMF10' international conference, organized jointly by University of Delhi and Society for Technologically Advanced Materials of India (STAMI) during November 7-11, 2016 at New Delhi, India.
7. *'Observation of high-temperature magnetic transition and existence of ferromagnetic short-range correlations above transition in La_2FeMnO_6'*, **Jasnamol P Palakkal**, *et al.;* **Oral** presentation at 'Research Scholars Symposium on Materials Science and Engineering' organized by the Indian Institute of Metals Trivandrum Chapter at CSIR NIIST on 20th December, 2016.